COMPUTATION OF SURFACE FIELDS EXCITED ON ARBITRARY SMOOTH CONVEX SURFACES WITH AN IMPEDANCE BOUNDARY CONDITION

A DISSERTATION SUBMITTED TO
THE DEPARTMENT OF ELECTRICAL AND ELECTRONICS
ENGINEERING
AND THE GRADUATE SCHOOL OF ENGINEERING AND SCIENCES
OF BILKENT UNIVERSITY
IN PARTIAL FULFILLMENT OF THE REQUIREMENTS
FOR THE DEGREE OF
DOCTOR OF PHILOSOPHY

By
Burak Alişan
July, 2012

I certify that I have read this thesis and that in my opinion it is fully adequate, in scope and in quality, as a dissertation for the degree of doctor of philosophy.

Assoc. Prof. Dr. Vakur B. Ertürk (Advisor)

I certify that I have read this thesis and that in my opinion it is fully adequate, in scope and in quality, as a dissertation for the degree of doctor of philosophy.

Prof. Dr. Ayhan Altıntaş

I certify that I have read this thesis and that in my opinion it is fully adequate, in scope and in quality, as a dissertation for the degree of doctor of philosophy.

Prof. Dr. Özlem Aydın Çivi

I certify that I have read this thesis and that in my opinion it is fully adequate, in scope and in quality, as a dissertation for the degree of doctor of philosophy.

Prof. Dr. Ergin Atalar

I certify that I have read this thesis and that in my opinion it is fully adequate, in scope and in quality, as a dissertation for the degree of doctor of philosophy.

Assoc. Prof. Dr. M. Özgür Oktel

Approved for the Graduate School of Engineering and Sciences:

Prof. Dr. Levent Onural
Director of Graduate School of Engineering and Sciences

ABSTRACT

COMPUTATION OF SURFACE FIELDS EXCITED ON ARBITRARY SMOOTH CONVEX SURFACES WITH AN IMPEDANCE BOUNDARY CONDITION

Burak Alişan
Ph.D in Electrical and Electronics Engineering
Supervisor: Assoc. Prof. Dr. Vakur B. Ertürk
July, 2012

Due to an increase in the use of conformal antennas in military and commercial applications, the study of surface fields excited by a current distribution on material coated perfect electric conductor (PEC) surfaces is becoming more important. These surface fields are useful in the efficient evaluation of mutual coupling of conformal slot/aperture antennas as well as in the design/analysis of conformal antennas/arrays which can be mounted on aircrafts, missiles, mobile base stations, etc. On the other hand, impedance boundary condition (IBC) is widely used in surface field problems because it can model a thin material coated (or partially coated) PEC geometry and reduces the complexity of the surface field problem by relating the tangential electric fields to the tangential magnetic fields on the surface.

Evaluation of surface fields on the circular cylinder and sphere geometries is a canonical problem and stands as a building block for the general problem of surface fields excited on arbitrary smooth convex surfaces. Therefore, high frequency based asymptotic solutions for the surface fields on a source excited PEC convex surface have been investigated for a long time, and surface fields on such surfaces have been obtained by generalizing the surface field expressions of the PEC cylinder and sphere.

In this dissertation, a uniform geometrical theory of diffraction (UTD)-based high frequency asymptotic formulation for the appropriate Green's function representation pertaining to the surface fields excited by a magnetic current source located on an arbitrary smooth convex surface with an IBC is developed. In the course of obtaining the final UTD-based Green's function representation, surface field expressions of cylinder and sphere geometries are written in normal, binormal, tangent $[(\hat{n}, \hat{b}, \hat{t})]$ coordinates and their important parameters such as the divergence factor, the Fock parameter and Fock type integrals are generalized according to the locality of high frequency wave propagation. The surface field expressions for the arbitrary convex impedance surface are then written by blending the sphere and cylinder solutions through blending functions, which are introduced heuristically.

Numerical results are selected from singly and doubly curved surfaces. Because of the lack of numerical results for the surface fields for impedance surfaces in the literature, obtained results are compared with those of PEC surfaces in the limiting case where the surface impedance,$Z_s \to 0$.

Keywords: Surface fields, Impedance boundary condition, UTD based Green's functions, Arbitrary smooth convex surfaces, Fock type integrals.

ÖZET

EMPEDANS SINIR KOŞULU OLAN RASTGELE DISBUKEY YÜZEYLERDEKI YÜZEY ALANLARININ HESAPLANMASI

Burak Alişan
Elektrik ve Elektronik Mühendisliği, Doktora
Tez Yöneticisi: Vakur B. Ertürk
Temmuz, 2012

Askeri ve ticari uygulamalarda konformal antenlerin kullanımının artmasına bağlı olarak, malzeme ile kaplı mükemmel elektrik iletken (PEC) yüzeyler üzerinde bir akım dağılımı ile oluşturulan yüzey alanları üzerindeki çalışmalar daha önemli hale gelmektedir. Bu yüzey alanları konformal yarık veya açıklık antenlerin karşılıklı kuplajının verimli bir şekilde hesaplanmasında olduğu kadar uçaklar, füzeler, mobil baz istasyonları, v.b. üzerine monte edilebilir konformal antenler veya anten dizilerinin tasarım ve analizinde yararlıdır. Diğer yandan, empedans sınır koşulu (IBC) ince bir malzeme ile kaplı (veya kısmen kaplı) bir PEC geometriyi modelleyebildiği ve yüzeye teğet elektrik alanlar ile yüzeye teğet manyetik alanları ilişkilendirerek yüzey alanı probleminin karmaşıklığını azalttığı için yaygın olarak kullanılır.

Dairesel silindir ve küre geometrileri üzerindeki yüzey alanlarının hesaplanması kanonik bir problemdir ve rastgele düzgün dışbükey yüzeylerde oluşturulan genel yüzey alanları problemi için bir yapı taşıdır. Bu nedenle, PEC dışbükey yüzeyde oluşturulan yüzey alanlarının yüksek frekans bazlı asimptotik çözümleri uzun bir süre için incelenmiş ve bu gibi yüzeyler üzerindeki yüzey alanları PEC silindir ve kürenin yüzey alanı ifadelerinin genelleştirilmesi ile elde edilmiştir.

Bu tezde, tekdüzen kırınımın geometrik teorisi (UTD) tabanlı empedans sınır koşuluna sahip rastgele düzgün dışbükey yüzey üzerindeki bir manyetik akım kaynağı ile oluşturulan yüzey alanlarına ilişkin uygun Green fonksiyonu için yüksek frekans asimptotik formülleştirmesi geliştirilmiştir. UTD tabanlı Green fonksiyonunun son halini elde ederken, silindir ve küre geometrileri yüzey alanı ifadeleri normal, binormal, tanjant $[(\hat{n}, \hat{b}, \hat{t})]$ koordinatlarında yazılmış ve ıraksama faktörü, Fock parametresi ve Fock tipi entegraller gibi önemli parametreler yüksek frekanslı dalga yayılımının yerellik özelliğine dayanarak genelleştirilmiştir. Daha sonra rastgele dışbükey empedans yüzey için yüzey alanı ifadeleri, küre ve silindir çözümlerinin sezgisel olarak tanımlanan harmanlama fonksiyonları ile harmanlanarak yazılmıştır.

Sayısal sonuçlar, tek ve çift eğimli yüzeylerden seçilmiştir. Literatürde empedans yüzeylerdeki yüzey alanları için sayısal sonuçlar olmamasından dolayı, elde edilen sonuçlar yüzey empedansının sıfıra gittiği ($Z_s \rightarrow 0$) limit durumda PEC yüzeylerdeki yüzey alanı sonuçları ile kıyaslanmıştır.

Anahtar sözcükler: Yüzey alanları, Empedans sınır koşulu, UTD'ye dayalı Green fonksiyonu, Rastgele düzgün dışbükey yüzeyler, Fock tipi integraller.

To my wife, Fatma, and my son, Toprak.

Acknowledgement

I would like to express my sincere gratitude to my advisor Prof. Vakur B. Ertürk for the continuous support of my Ph.D study and research, for his patience, motivation, enthusiasm, and knowledge. His guidance helped me in all the time of research and writing of this dissertation. I could not have imagined having a better supervisor for my Ph.D study.

Besides my supervisor, I would like to thank the rest of my Ph.D progress committee: Prof. Ayhan Altıntaş, and Prof. Özlem Aydın Çivi for their instructive comments, support and guidance.

I would like to express my special thanks and gratitude to Prof. Ergin Atalar and Prof. M. Özgür Oktel for showing keen interest to the subject matter and accepting to read and review this dissertation.

Futhermore, I would like to thank Aselsan Inc. for letting me to involve in this thesis study.

Finally, I would like to thank my wife, Fatma, for her understanding, support, encouragement and endless love.

Contents

1 Introduction 1

2 Asymptotic solutions for the surface fields pertaining to the canonical problems 8

2.1 Circular Cylinder 8

2.1.1 PEC Circular Cylinder 10

2.1.2 Impedance Circular Cylinder 10

2.2 Sphere 12

2.2.1 PEC Sphere 13

2.2.2 Impedance sphere 14

2.2.3 Caustic Corrections 15

3 Generalization to arbitrary smooth convex impedance surfaces 17

3.1 PEC Surface 17

3.1.1 Generalization to arbitrary convex surfaces 17

3.2 Impedance Surface 21

3.2.1 Expressions for cannonical problems 22

3.2.2 Generalization to arbitrary convex surfaces 23

4 Numerical Results **30**

4.1 PEC Surfaces 31

4.2 Impedance Surfaces 43

4.2.1 Cannonical surfaces 50

4.2.2 Arbitrary smooth convex surfaces 51

4.3 Results obtained by simulation tools 68

5 Conclusions **72**

Appendix **75**

A Uniform Geometrical Theory of Diffraction (UTD) **75**

B Eigenfunction solution pertaining to the canonical problems **77**

B.1 Impedance Circular Cylinder 77

B.2 Impedance Sphere 81

C Derivation of asymptotic solution pertaining to the circular cylinder **87**

C.1 PEC Circular Cylinder 87

C.2 Impedance Circular Cylinder 91

D Derivation of asymptotic solution pertaining to the sphere 97

D.1 PEC Sphere 97

D.2 Impedance Sphere 101

E Calculation of geometrical and electrical parameters for UTD solution 109

E.1 Circular cone geometry 112

E.2 General parabolic cylinder (GPCYL) geometry 115

E.3 Elliptic cylinder geometry 118

E.4 General paraboloid of revolution (GPOR) geometry 120

List of Figures

1.1 Ray coordinates 5

2.1 Cylinder geometry 9

2.2 Sphere geometry 13

4.1 Rectangular apertures with the dimensions a and b such that only the TE_{10} mode is generated. 32

4.2 Problem geometry for a PEC circular cone that has two circumferential slots on it. 34

4.3 Mutual admittance between two circumferential slots with slot length= 0.5λ and width= 0.2λ at radial positions ($u_1 = u_2 = 8\lambda$) on a cone, which has a 15° half-cone angle, as a function of angular separation, $v_2 - v_1$. 35

4.4 Comparison of the magnitude of S_{21} between two circumferential slots with slot ength= 0.9", width= 0.4" and angular separation ($v_2 - v_1 = 60.8°$) on a cone, which has a 12.2° half-cone angle as function of frequency 35

4.5 Problem geometry for PEC GPCYL 36

4.6 Comparison of the magnitude and phase of E-plane coupling between two slots with slot dimensions $0.27\lambda \times 0.65\lambda$ as a function of distance of the second slot to the vertex on Parab.1 37

4.7 Comparison of the magnitude and phase of E-plane coupling between two slots with slot dimensions $0.27\lambda \times 0.65\lambda$ as a function of distance of the second slot to the vertex on Parab.2 38

4.8 Comparison of the magnitude and phase of E-plane coupling between two slots with slot dimensions $0.27\lambda \times 0.65\lambda$ as a function of distance of the second slot to the vertex on Parab.3 38

4.9 Problem geometry for PEC elliptic cylinder 39

4.10 Comparison of the magnitude and phase of E-plane coupling between two slots with slot dimensions $0.27\lambda \times 0.65\lambda$ as a function of distance of second slot to the vertex on an elliptic cylinder with $a/b = 1$ (corresponds to circular cylinder) 41

4.11 Comparison of the magnitude and phase of E-plane coupling between two slots with slot dimensions $0.27\lambda \times 0.65\lambda$ as a function of distance of second slot to the vertex on an elliptic cylinder with $a/b = 1.2$ 41

4.12 Comparison of the magnitude and phase of E-plane coupling between two slots with slot dimensions $0.27\lambda \times 0.65\lambda$ as a function of distance of second slot to the vertex on an elliptic cylinder with $a/b = 2$ 42

4.13 Comparison of the magnitude and phase of E-plane coupling between two slots with slot dimensions $0.27\lambda \times 0.65\lambda$ as a function of distance of second slot to the vertex on an elliptic cylinder with $a/b = 6$ 42

4.14 Problem geometry for PEC GPOR 43

4.15 Problem geometry for the first configuration 44

4.16 Problem geometry for the second configuration 44

4.17 Comparison of the magnitude and phase of S_{21} ($[R, R]$ polarization) between two circular waveguide fed apertures as a function of u_f with the calculated results and calculation and measurement of [13] for the first configuration 45

4.18 Comparison of the magnitude and phase of S_{21} ($[R, \phi]$ polarization) between two circular waveguide fed apertures as a function of u_f with the calculated results and calculation and measurement of [13] for the first configuration 45

4.19 Comparison of the magnitude and phase of S_{21} ($[\phi, R]$ polarization) between two circular waveguide fed apertures as a function of u_f with the calculated results and calculation and measurement of [13] for the first configuration 46

4.20 Comparison of the magnitude and phase of S_{21} ($[\phi, \phi]$ polarization) between two circular waveguide fed apertures as a function of u_f with the calculated results and calculation and measurement of [13] for the first configuration 46

4.21 Comparison of the magnitude and phase of S_{21} ($[R, R]$ polarization) between two circular waveguide fed apertures as a function of u_f with the calculated results and calculation and measurement of [13] for the second configuration 47

4.22 Comparison of the magnitude and phase of S_{21} ($[R, \phi]$ polarization) between two circular waveguide fed apertures as a function of u_f with the calculated results and calculation and measurement of [13] for the second configuration 47

4.23 Comparison of the magnitude and phase of S_{21} ($[\phi, R]$ polarization) between two circular waveguide fed apertures as a function of u_f with the calculated results and calculation and measurement of [13] for the second configuration 48

4.24 Comparison of the magnitude and phase of S_{21} ($[\phi, \phi]$ polarization) between two circular waveguide fed apertures as a function of u_f with the calculated results and calculation and measurement of [13] for the second configuration 48

4.25 Comparison of the magnitude of $G_{\phi\phi}$ component of the eigenfunction solution and the UTD-based solution for the azimuthal angle, $(\phi_2 - \phi_1)$, varying from 0° to 45° at $f = 7GHz$ for a fixed vertical distance, $z_2 - z_1 = 3\lambda$, on a circular cylinder with $a = 5\lambda$ and $\Lambda = 0.1$ 50

4.26 Comparison of the magnitude of H_ϕ component of the eigenfunction solution and the UTD-based solution for the geodesic path length, s, varying from 0.1λ to 2λ at $f = 10GHz$ for a fixed $\phi = 90°$ on a sphere with $a = 3\lambda$ and $\Lambda = 0.75$ 51

4.27 Problem geometry for impedance GPCYL 52

4.28 Comparison of the magnitudes of the calculated tangential magnetic field components with and without Δ terms for the geodesic path length varying from 1λ to 5λ for a GPCYL with $a = 5$ having a surface impedance of $Z_s = 1\Omega$ with those of PEC GPCYL . . . 53

4.29 Comparison of the phases of the calculated tangential magnetic field components with and without Δ terms for the geodesic path length varying from 1λ to 5λ for a GPCYL with $a = 5$ having a surface impedance of $Z_s = 1\Omega$ with those of PEC GPCYL 54

4.30 Problem geometry for impedance elliptic cylinder 55

4.31 Comparison of the magnitudes of the calculated tangential magnetic field components with and without Δ terms for the geodesic path length varying from 1λ to 5λ for an elliptic cylinder with $a = 5$ and $b = 2$ having a surface impedance of $Z_s = 1\Omega$ with those of PEC elliptic cylinder 56

4.32 Comparison of the phases of the calculated tangential magnetic field components with and without Δ terms for the geodesic path length varying from 1λ to 5λ for an elliptic cylinder with $a = 5$ and $b = 2$ having a surface impedance of $Z_s = 1\Omega$ with those of PEC elliptic cylinder 57

4.33 Problem geometry for impedance GPOR 58

4.34 Comparison of the magnitudes of the calculated tangential magnetic field components with and without Δ terms for u_f varying from 0.5 to 4 for a GPOR with $a = 5$ having a surface impedance of $Z_s = 1\Omega$ with those of PEC GPOR 59

4.35 Comparison of the phases of the calculated tangential magnetic field components with and without Δ terms for u_f varying from 0.5 to 4 for a GPOR with $a = 5$ having a surface impedance of $Z_s = 1\Omega$ with those of PEC GPOR 60

4.36 Angle between the geodesic path and the principal surface direction at the source/observation point 61

4.37 Magnitudes of the calculated tangential magnetic field components without Δ terms for u_f varying from 0.5 to 4 on GPORs with $a = 5$ having different surface impedances in the form of $Z_s = \alpha$. PEC result is given for reference. 62

4.38 Magnitudes of the calculated tangential magnetic field components without Δ terms for u_f varying from 0.5 to 4 on GPORs with $a = 5$ having different surface impedances in the form of $Z_s = \alpha + j\beta$. PEC result is given for reference. 63

4.39 Magnitudes of the calculated tangential magnetic field components without Δ terms for u_f varying from 0.5 to 4 on GPORs with $a = 5$ having different surface impedances in the form of $Z_s = \alpha - j\beta$. PEC result is given for reference. 64

4.40 Magnitudes of the calculated tangential magnetic field components with Δ terms for u_f varying from 0.5 to 4 on GPORs with $a = 5$ having different surface impedances in the form of $Z_s = \alpha$. PEC result is given for reference. 65

4.41 Magnitudes of the calculated tangential magnetic field components with Δ terms for u_f varying from 0.5 to 4 on GPORs with $a = 5$ having different surface impedances in the form of $Z_s = \alpha + j\beta$. PEC result is given for reference. 66

4.42 Magnitudes of the calculated tangential magnetic field components with Δ terms for u_f varying from 0.5 to 4 on GPORs with $a = 5$ having different surface impedances in the form of $Z_s = \alpha - j\beta$. PEC result is given for reference. 67

4.43 Comparison of the magnitude and phase of the mutual admittance between two slots [Source: $(u, v) = (1.115, 0)$, Observation: $(u, v) = (u_f, 0)$] with slot length $= 0.5\lambda$ and width $= 0.2\lambda$ on a GPCYL, which has a shaping parameter $a = 0.5$, computed using both UTD and HFSS as a function of increasing seperation between the two slots along the u axis 69

A.1 Line source excitation near a PEC half plane 76

B.1 Problem geometry for an impedance sphere 82

C.1 Integration paths, C_ψ and C_{SDP} , on the complex ψ plane 89

D.1 Contour of integration in the complex ν plane. $C_\nu = C_\nu^+ + C_\nu^-$ is the original contour and $\tilde{C}_\nu = \tilde{C}_\nu^+ + C_\nu^-$ is the new contour. 99

E.1 Caustic distance associated with the spreading of the surface ray field (used to calculate the divergence factor D) 112

E.2 Circular cone geometry 113

E.3 General parabolic cylinder geometry 116

E.4 Elliptic cylinder geometry 118

E.5 General paraboloid of revolution geometry 121

List of Tables

4.1 Magnitude (dB) of mutual admittance between two slots [Source: $(u, v) = (1, 0)$, Observation: $(u, v) = (1.2751, 0)$] with slot length $= 0.65\lambda$ and width $= 0.27\lambda$ on a GPCYL, which has a shaping parameter $a = 1.5$, computed using both UTD and HFSS 69

4.2 Comparison of magnitude (dB) of mutual admittance between two slots (slot length $= 0.65\lambda$ and width $= 0.27\lambda$) separated by 1λ on different planar surfaces computed by CST 71

Chapter 1

Introduction

Many military and commercial applications have stringent aerodynamic constraints that require the use of antennas that conform to their host platforms. This necessitates the development of efficient and accurate design and analysis tools for this class of antennas. Therefore, the study of surface fields excited on arbitrary smooth convex surfaces is of practical interest. Thus, the electromagnetic compatibility (EMC) and the electromagnetic interference (EMI) between these antennas become important, and their prediction requires an accurate, and if possible efficient, analysis of mutual coupling between the antennas and hence, surface fields excited by these antennas. However, such an analysis becomes a challenging task when the distance between the antennas along the geodesic path is large in terms of the wavelength. A possible remedy for this challenging task is to approximate the boundary conditions on surfaces by an impedance boundary condition (IBC) [1]-[3], and to perform the analysis using a Uniform Geometrical Theory of Diffraction (UTD [4]) based high-frequency asymptotic solution that, in general, contains a Fock type integral representation [5]. Information about UTD can be found in Appendix A.

Thin material coating is usually placed to reduce the isolation between the conformal antennas located on the surface. It decreases the mutual coupling between the antennas by attenuating the surface fields. IBC is a valid approximation for a thin material coated (or partially coated) PEC geometry when

1. $|N| \gg 0$
2. $|Im(N)|\, k_0 a_{min} \gg 0$

where N is the refractive index, k_0 is the wavenumber in the outside medium and a_{min} is the minimum radius of the curvature of the geometry [3]. IBC is a widely used approximation because it reduces the complexity and the reqired computational resource of the surface field problem by relating the tangential electric fields to the tangential magnetic fields on the surface.

The motivation for the development of the present UTD based solution is given below.

- Eigenfunction solutions to surface fields excited by a current distribution on the same surface are available for a limited number of geometries, such as cylinder, sphere, etc.
- Since geometries of interest are electrically large, computation of surface fields through the numerical methods such as Method of Moments (MoM), Finite Element Method (FEM), Finite Difference Time Domain (FDTD) is inefficient in terms of the computational time. Due to their extensive memory usage, it may be impossible solving a problem on a standard personal computer. Professional workstations with huge memory size are required for such kind of simulations.
- Unlike the numerical methods, UTD gives physical insight about the nature of the problem in terms of rays arising from certain points on the geometry.

Problem of surface fields on the circular cylinder and sphere geometries is a cannonical problem and stands as a building block for the general problem of surface fields excited on arbitrary smooth convex surfaces. High frequency based asymptotic solutions for the surface fields on a source excited perfect electric conductor (PEC) convex surface have been investigated for a long time. Expressions were obtained for the surface fields excited on perfectly conducting cylinders, spheres and cones. Approximate expressions were obtained for the magnetic field induced by slots on electrically large conducting circular cylinder [6]. Later, improved Geometrical Theory of Diffraction (GTD) and UTD based representations were presented for the surface fields due to a slot on a PEC cylinder [7]. A simple approximate expression for the surface magnetic field due to a magnetic dipole on a conducting circular cylinder was developed in [8]. The surface field solution obtained in [8] contains an additional term taken from [9] because of the need to obtain an accurate solution in the paraxial (nearly axial) region of the cylinder. Furthermore, an approximate asymptotic solution was presented for the electromagnetic fields which are induced on an electrically large perfectly conducting smooth convex surface by an infinitesimal magnetic or electric current moment on the same surface [10]-[11].

The surface field expressions for arbitrary convex PEC surfaces given in [11], which are developed by generalizing the surface field expressions of the PEC cylinder and sphere, are later used for obtaining mutual coupling between antennas on general parabolic cylinder (GPCYL)[12]-[13], general hyperbolic cylinder (GHCYL)[13], elliptic cylinder[13], general paraboloid of revolution (GPOR)[12]-[15]. [13] and [15] also contain comparison of the computed results with measurement results.

However, the study of surface fields created by a current distribution on the surface of an impedance surface, which can also model a thin material coated PEC case [2], is still a challenging problem. Recently, several high-frequency based asymptotic solutions for the surface fields on a source excited circular cylinder with an IBC have been presented valid away from the paraxial region, and within the paraxial region. A high frequency based solution for a surface field excited by a magnetic line source on an impedance cylinder has been presented in [16]. Later, a high frequency asymptotic solution has been introduced for the vector potentials for a point source on an anisotropic impedance cylinder [17]. In [18], an approximate asymptotic solution based on the UTD has been proposed for the magnetic fields excited at a point by an infinitesimal magnetic current moment located at another point, both on the surface of an electrically large circular cylinder with finite surface impedance. Afterwards, approximate solutions have been developed for the surface magnetic field on a magnetic current excited circular cylinder with an IBC in [19]-[20]. Later, an efficient computation technique is developed for the surface fields excited on an electrically large circular cylinder with an IBC [21]-[22] as part of my MSc and PhD study. Furthermore, an alternative approximate asymptotic closed-form solution has been proposed for the accurate representation of the tangential surface magnetic field within the paraxial region of a tangential magnetic current excited circular cylinder with an IBC in [23].

Several high-frequency based asymptotic solutions for the radio wave propagation around the earth that model the earth by a spherical impedance surface have been presented [5],[24]-[33], and attracted significant attention. Among them, [25] discusses the surface waves excited by a vertical dipole and their propagation on a sphere where the spherical surface exhibits an inductive reactance. In this solution, the electric field is expressed as the radiation field of the dipole if it were placed on the surface of a PEC plane multiplied by an attenuation factor (ground wave attenuation factor) that takes the curvature effects into account and possess a Fock type integral representation. [29] discusses the calculation of this ground wave attenuation factor at low frequencies, by using both residue series and power series based on the distance of the observation point from the source. In [30], analytical and numerical procedures are described for the evaluation of some Fock type integral functions that appear in a method presented by [28] to compute the tangential magnetic field on the surface of a smooth inhomogeneous earth excited by a plane wave. Then, [31] generalizes the computation of the ground wave attenuation function for a spherical earth with an arbitrary surface impedance, where ground waves are excited by a vertical electric dipole located at the surface of the earth. Their attenuation function is represented in terms of a Fock type integral, and is in general computed using a residue series approach. However, when the argument of the attenuation function is small (i.e., small curvature case), the attenuation function is computed preferably using either its power series representation given by [34]-[36], or its small curvature expansion [34]-[35] based on the complementary error function. More references on the subject of ground wave propagation, including the early work, can be found in [37]. However, the aforementioned solutions are in general valid far from the

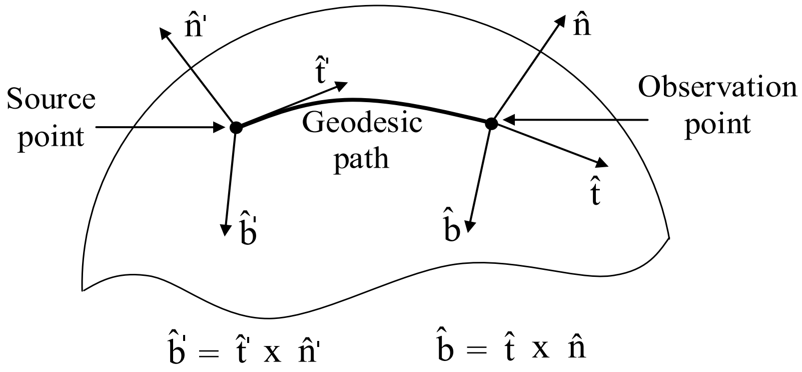

Figure 1.1: Ray coordinates

source location. A different high-frequency based asymptotic analysis from that used traditionally in the ground wave propagation problems is developed in [38] as part of my PhD study. This solution is a UTD-based representation of the surface fields excited by a magnetic current located on the surface of a sphere that has a uniform surface impedance, Z_s, with a positive real part. The radius of the sphere and the length of the geodesic path between the source and observation points, when both are located on the surface of the sphere, are assumed to be large compared to the wavelength. Unlike the UTD-based solution for a PEC sphere developed in [10], some higher-order terms and derivatives of Fock type integrals are included as they may become important for certain impedance values. It is shown that when $Z_s \to 0$, the UTD-based solution recovers to that of the PEC case developed in [10] with higher-order terms and derivatives of the corresponding Fock type integrals. Furthermore, the methodology developed in [10] to correct the surface fields at the caustic of the PEC sphere is extended to the impedance sphere case.

In this dissertation, a UTD-based high frequency asymptotic formulation for the appropriate Green's function representation pertaining to the surface fields excited by a magnetic current source located on an arbitrary smooth convex surface with an IBC is developed for the first time. Present formulation extends the UTD-based high frequency based asymptotic solutions for the surface fields on a source excited PEC convex surface given in [10] and [11]. In the course of obtaining the final UTD-based Green's function representation, surface field expressions of cylinder and sphere geometries are written in normal, binormal, tangent $[\hat{n}, \hat{b}, \hat{t}]$ coordinates, shown in Fig. 1.1. $[\hat{n}, \hat{b}, \hat{t}]$ are ray coordinates and form a right-handed orthonormal basis ($\hat{b} = \hat{t} \times \hat{n}$) and change direction along the ray according to the curvature and torsion of the ray. The important parameters included in the surface field expressions such as the divergence factor, the Fock parameter and Fock type integrals are generalized according to the locality of the high frequency wave propagation. The surface field expressions for the arbitrary convex impedance surface are then written by blending the sphere and cylinder solutions through blending functions, which are introduced heuristically. The final UTD-based Green's function representation for impedance surfaces looks very similar to that of PEC surfaces except the Fock type integrals and extra terms. If the extra terms are discarded, the UTD solution for impedance surfaces reduces to the PEC solution in the limiting case, $Z_s \rightarrow 0$. Numerical results are selected from singly and doubly curved surfaces. Obtained results are compared with those of PEC surfaces in the limiting case where the surface impedance, $Z_s \rightarrow 0$ because

- There are not any numerical results for the surface fields for impedance surfaces in the literature, except cylinder and sphere geometries. Moreover, the results for the impedance sphere in the literature are the outcomes of this PhD study.
- Popular simulation tools such as HFSS, CST and FEKO do not give accurate results for the impedance boundary condition.
- We are trying to collaborate with other groups to obtain numerical results from their in house FEM/FDTD programs. This process could not be completed during my PhD study.

The organization of this dissertation is as follows: In Chapter II, the UTD based asymptotic solutions for the surface fields excited by both a magnetic point source located on the surface of an electrically large PEC/impedance cylinder and sphere are given. The impedance cylinder and sphere expressions, given in Chapter II, are generalized to obtain the surface field expressions for the arbitrary convex impedance surface via the locality of high frequency wave propagation in Chapter III. Several numerical results are presented in Chapter IV. Finally, conclusions are given in Chapter V. There are also 5 Appendices. A brief information about UTD is provided in Appendix A. In Appendix B, derivation of the eigenfunction solution pertaining to the impedance circular cylinder and sphere is given. Asymptotic solutions pertaining to PEC/impedance circular cylinder and PEC/impedance sphere are developed in Appendices C and D, respectively. Calculation of geometrical and electrical parameters of the circular cone, general parabolic cylinder, elliptic cylinder and general paraboloid of revolution required for the UTD solution is provided in Appendix E. An e^{jwt} time dependence is assumed and suppressed throughout this dissertation, where $w = 2\pi f$ and f is the frequency.

Chapter 2

Asymptotic solutions for the surface fields pertaining to the canonical problems

2.1 Circular Cylinder

Consider an electrically large circular cylinder, as shown in Fig. 2.1. The cylinder has a radius a, and is assumed to be infinitely long along its axial direction. The tangential surface field excited by a tangential magnetic source, which is located on the cylinder, is expressed as

$$\vec{H}_t = \vec{P}_m \cdot (\hat{z}'\hat{z}G_{zz} + \hat{\phi}'\hat{z}G_{z\phi} + \hat{z}'\hat{\phi}G_{\phi z} + \hat{\phi}'\hat{\phi}G_{\phi\phi}) \tag{2.1}$$

where $\vec{P}_m$ represents the strength and the orientation of the magnetic current and G_{pq} is a UTD-based Green's function representation for a $\hat{p}$ ($\hat{p} = \hat{z}$ or $\hat{\phi}$) oriented surface magnetic field due to a $\hat{q}$ ($\hat{q} = \hat{z}$ or $\hat{\phi}$) directed magnetic current. In (2.1), G_{pq} represents the summation of all ray encirclements around the cylinder and can be determined as

$$G_{pq} = \sum_{\ell=0}^{\infty}(G_{pq}^{\ell+} + G_{pq}^{\ell-}) \tag{2.2}$$

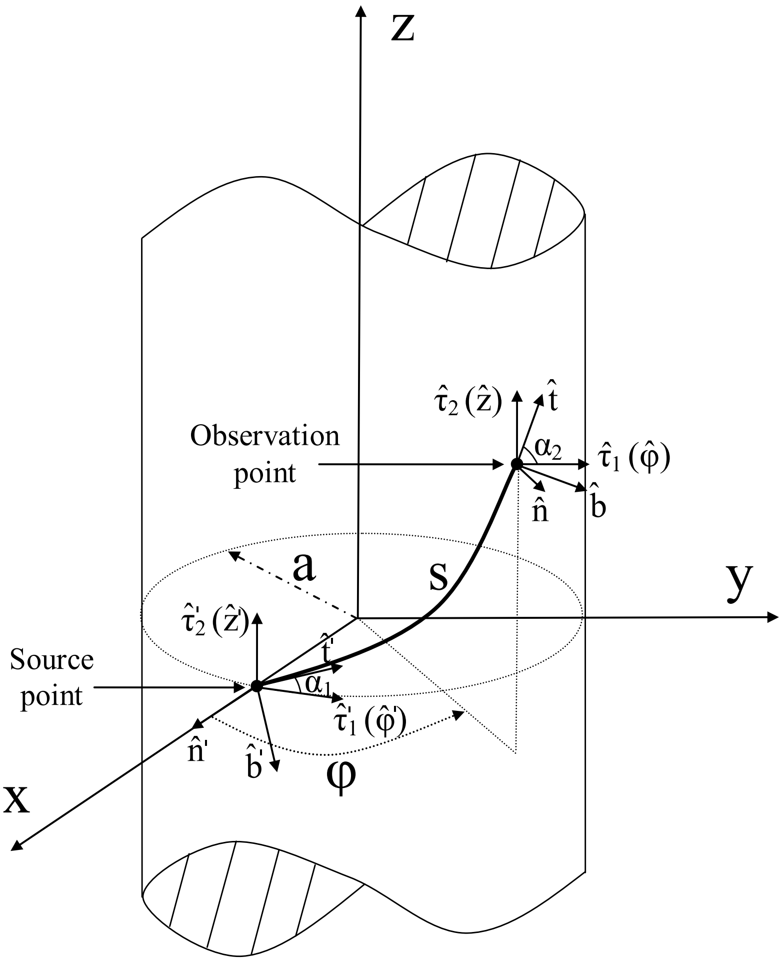

Figure 2.1: Cylinder geometry

where $G_{pq}^{\ell+}$ pertains to the Green's function which is responsible from the surface waves propagating around the cylinder in the positive $\hat{\phi}$ direction, whereas $G_{pq}^{\ell-}$ corresponds to those propagating in the negative $\hat{\phi}$ direction. Provided that the cylinder is electrically large (more than a free-space wavelength in radius), it is enough to retain the $\ell = 0$ term, which corresponds to the primary rays propagating around the cylinder.

2.1.1 PEC Circular Cylinder

The UTD-based asymptotic Green's function representations for a tangential magnetic source on a PEC cylinder are expressed in [10] as [see Appendix C.1, Eqns. (C.24)-(C.27)]

$$G_{zz}^{\ell\pm} \sim G_0\left\{\cos^2\alpha V + \frac{j}{ks}\left(1-\frac{j}{ks}\right)\left(2-3\cos^2\alpha\right)V\right\} \tag{2.3}$$

$$G_{z\phi}^{\ell\pm} \sim \mp G_0\left\{\cos\alpha\sin\alpha\left[1-\frac{j3}{ks}\left(1-\frac{j}{ks}\right)\right]V\right\} \tag{2.4}$$

$$G_{\phi z}^{\ell\pm} \sim \mp G_0\left\{\cos\alpha\sin\alpha\left[1-\frac{j3}{ks}\left(1-\frac{j}{ks}\right)V\right]\right\} \tag{2.5}$$

$$\begin{aligned} G_{\phi\phi}^{\ell\pm} \sim G_0\Bigg\{&\sin^2\alpha V + \frac{j}{ks}\left(1-\frac{j}{ks}\right)\left(2-3\sin^2\alpha\right)V \\ &+\frac{j}{ks}\frac{1}{\cos^2\alpha}\left(U-V\right)\Bigg\} \end{aligned} \tag{2.6}$$

where

$$G_0 = -\frac{jk^2e^{-jks}}{2\pi Z_0 ks} \tag{2.7}$$

k is the free space wave number, Z_0 is the free space impedance, s is the geodesic ray path between the source and observation points, and α is the angle between s and the positive $\hat{\phi}$ direction as shown in Fig. 2.1. The U and V terms in (2.3)-(2.6) are Fock type integrals and can be expressed as

$$U = j\xi\sqrt{\frac{j\xi}{\pi}}\int_{-\infty}^{\infty} d\tau e^{-j\xi\tau}\frac{W_2'(\tau)}{W_2(\tau)} \tag{2.8}$$

$$V = \sqrt{\frac{j\xi}{4\pi}}\int_{-\infty}^{\infty} d\tau e^{-j\xi\tau}\frac{W_2(\tau)}{W_2'(\tau)} \tag{2.9}$$

where $\xi = m\phi$, $m = (ka/2)^{1/3}$, $W_2(\tau)$ is a Fock-type Airy function, and $W_2'(\tau)$ is its derivative with respect to τ. A brief summary of the derivation of this asymptotic solution can be found in Appendix C.1.

2.1.2 Impedance Circular Cylinder

The UTD-based asymptotic Green's function representations for a tangential magnetic source on an impedance cylinder are expressed in [19] as [see Appendix

C.2, Eqns. (C.46)-(C.49)]

$$
\begin{aligned}
G_{zz}^{\ell\pm} &\sim G_0\Bigg\{\cos^2\alpha V_0+\frac{j}{ks}\left(1-\frac{j}{ks}\right)(2-3\cos^2\alpha)V_0\\
&\quad-\frac{j2}{k}\left(1-\frac{j}{ks}\right)\sin\alpha\frac{\partial V_0}{\partial z_d}+\frac{1}{k^2}\frac{\partial^2V_0}{\partial z_d^2}\Bigg\} \qquad (2.10)\\
G_{z\phi}^{\ell\pm} &\sim \mp G_0\Bigg\{\cos\alpha\sin\alpha\left[1-\frac{j3}{ks}\left(1-\frac{j}{ks}\right)\right]Y_0\\
&\quad-\frac{j2}{k}\left(\tan^2\alpha+\frac{j}{ks}\right)\cos\alpha\frac{\partial Y_0}{\partial z_d}+\frac{\tan\alpha}{k^2}\frac{\partial^2Y_0}{\partial z_d^2}\Bigg\} \qquad (2.11)\\
G_{\phi z}^{\ell\pm} &\sim \mp G_0\Bigg\{\cos\alpha\sin\alpha\left[X_0+V_0-\frac{j3}{ks}(1-\frac{j}{ks})V_0\right]\\
&\quad+\frac{j}{k}\left(1-\frac{j}{ks}\right)\left(\cos\alpha\frac{\partial V_0}{\partial z_d}+\sin\alpha\frac{\partial V_0}{\partial y_\ell}\right)-\frac{1}{k^2}\frac{\partial^2V_0}{\partial y_\ell\partial z_d}\Bigg\} \qquad (2.12)\\
G_{\phi\phi}^{\pm} &\sim G_0\Bigg\{\sin^2\alpha Y_0+\frac{j}{ks}\left(1-\frac{j}{ks}\right)(2-3\sin^2\alpha)Y_0+\frac{j}{ks}\frac{1}{\cos^2\alpha}(U_0-Y_0)\\
&\quad+\frac{j}{k}\left(1-\frac{j}{ks}\right)\left(\sin\alpha\frac{\partial Y_0}{\partial z_d}-\cos\alpha\frac{\partial Y_0}{\partial y_\ell}\right)\\
&\quad+\frac{j}{k\cos\alpha}\left(\frac{\partial Y_0}{\partial y_\ell}-\frac{j}{ks}\tan\alpha\frac{\partial Y_0}{\partial z_d}\right)-\frac{\tan\alpha}{k^2}\frac{\partial^2Y_0}{\partial y_\ell\partial z_d}\Bigg\} \qquad (2.13)
\end{aligned}
$$

where G_0 is given in (2.7). The V_0, Y_0, X_0 and U_0 terms in (2.10)-(2.13) are Fock type integrals and can be expressed as

$$
\begin{aligned}
V_0 &= \frac{1}{2}\sqrt{\frac{j\xi}{\pi}}\int_{-\infty}^{\infty}d\tau e^{-j\xi\tau}\frac{1}{D_w}(R_w-q_m) \qquad (2.14)\\
Y_0 &= -\frac{q_m}{2}\sqrt{\frac{j\xi}{\pi}}\int_{-\infty}^{\infty}d\tau e^{-j\xi\tau}\frac{1}{D_w}\left(1+\frac{\tau}{2m_t^2}\right) \qquad (2.15)\\
X_0 &= -\frac{1}{2}\sqrt{\frac{j\xi}{\pi}}\int_{-\infty}^{\infty}d\tau e^{-j\xi\tau}\frac{R_w}{D_w}\left(1+\frac{\tau}{2m_t^2}\right) \qquad (2.16)\\
U_0 &= -j\xi q_m\sqrt{\frac{j\xi}{\pi}}\int_{-\infty}^{\infty}d\tau e^{-j\xi\tau}\frac{R_w}{D_w}(R_w-q_e) \qquad (2.17)
\end{aligned}
$$

where

$$D_w=(R_w-q_e)(R_w-q_m)+q_c^2 \qquad (2.18)$$

in which

$$q_e = -jm_t\Lambda\cos\alpha \tag{2.19}$$

$$q_m = -jm_t\Lambda^{-1}\cos\alpha \tag{2.20}$$

$$q_c = -jm_t\left(1+\frac{\tau}{2m_t^2}\right)\sin\alpha. \tag{2.21}$$

It should be mentioned that the expressions given in (2.10)-(2.13) are valid in the non-paraxial region, and developed mainly for large separations, s, between the source and field points with respect to wavelength λ. However, since some of the second order terms (derivative terms) are included, they may remain accurate even for relatively small separations. The details of the derivation of this asymptotic solution can be found in Appendix C.2.

2.2 Sphere

Consider an electrically large sphere as shown in Fig. 2.2. The sphere has a radius a. A magnetic source is defined as $\vec{P_m} = \hat{x}p_m\delta(\bar{r}-\bar{r}')$ and is located at the point $(r'=a, \theta'=0, \phi'=0)$ on the sphere. The tangential magnetic fields at the field point $(r=a,\theta,\phi)$ on the surface of the sphere are expressed as

$$\vec{H}_t \sim \hat{t}(\hat{t}\cdot\vec{H}) + \hat{b}(\hat{b}\cdot\vec{H}) = \hat{t}H_\theta - \hat{b}H_\phi \tag{2.22}$$

where H_p is a UTD based Green's function representation for a $\hat{p}$ ($\hat{p}=\hat{\theta}$ or $\hat{\phi}$) oriented surface magnetic field due to magnetic current, $\vec{P_m}$. H_p represents the summation of all ray encirclements around the sphere and can be determined as

$$H_p = \sum_{\ell=0}^{\infty}(H_p^{\ell+} + H_p^{\ell-}) \tag{2.23}$$

where $H_p^{\ell+}$ pertains to the Green's function which is responsible from the surface waves propagating around the cylinder in the positive $\hat{\theta}$ direction, whereas $H_p^{\ell-}$ corresponds to those propagating in the negative $\hat{\theta}$ direction. Provided that the sphere is electrically large (more than a free-space wavelength in radius), it is enough to retain the $\ell = 0$ term, which corresponds to the primary rays propagating around the sphere.

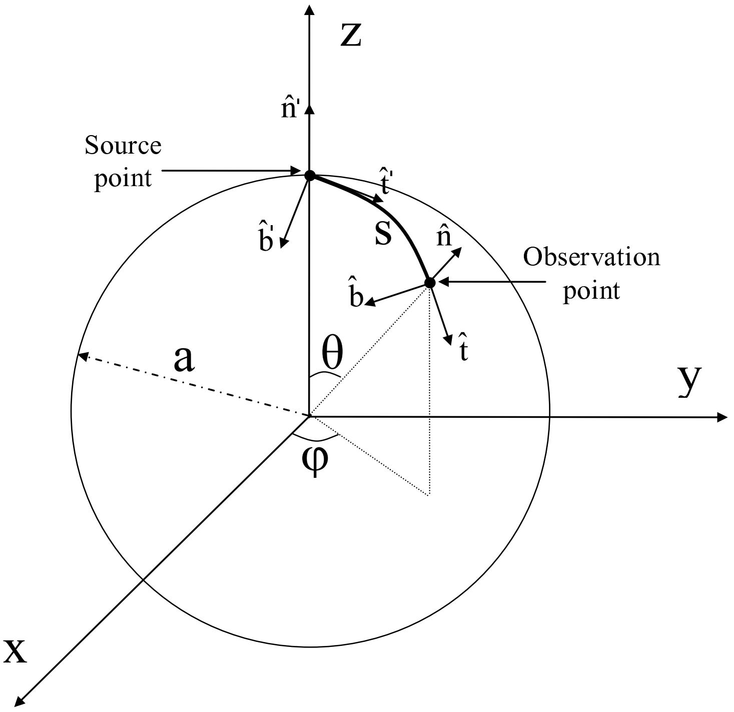

Figure 2.2: Sphere geometry

2.2.1 PEC Sphere

The UTD-based asymptotic Green's function representations for a tangential magnetic source on a PEC sphere are expressed in [10] as [see Appendix D.1, Eqns. (D.24)-(D.25)]

$$H_\theta^\pm = \pm p_m \cos\phi \left[\frac{j}{ks}(1-\frac{2j}{ks})U + D^2 \frac{j}{ks} V \right] DG_0 \tag{2.24}$$

$$H_\phi^\pm = \mp p_m \sin\phi \left[(1-\frac{j}{ks})V - D^2 \frac{U}{(ks)^2} \right] DG_0 \tag{2.25}$$

where

$$D = \sqrt{\frac{\theta}{\sin\theta}} \tag{2.26}$$

is the divergence factor and G_0, U, and V are given in Eqs.(2.7)-(2.9). The details of the asymptotic solution can be found in Appendix D.1.

2.2.2 Impedance sphere

The UTD-based asymptotic Green's function representations for a tangential magnetic source on an impedance sphere are expressed as [see Appendix D.2, Eqns. (D.51)-(D.52)]

$$
\begin{aligned}
H_\theta^\pm &= \pm p_m \cos\phi \Bigg\{ \left[\frac{j}{ks}\left(1 - \frac{2j}{ks}\right) U_z(\xi) + D^2 \frac{j}{ks} V_z(\xi) \right] D G_0 \\
&\quad - G_0 \frac{1}{4m^5 \xi} \frac{\partial}{\partial\theta} [D U_z(\xi)] \Bigg\} \qquad (2.27) \\
H_\phi^\pm &= \mp p_m \sin\phi \Bigg\{ \left[\left(1 - \frac{j}{ks}\right) V_z(\xi) + j^2 D^2 \frac{U_z(\xi)}{(ks)^2} \right] D G_0 \\
&\quad + G_0 \frac{j}{2m^3} \frac{\partial}{\partial\theta} [D V_z(\xi)] \Bigg\}. \qquad (2.28)
\end{aligned}
$$

In (2.27)-(2.28), V_z and U_z are the Fock type integrals given by

$$
\begin{aligned}
V_z &= \sqrt{\frac{j\xi}{4\pi}} \int_{-\infty}^{\infty} \frac{1}{R_w - q_e} e^{-j\xi\tau} d\tau \qquad (2.29) \\
U_z &= e^{j3\pi/4} \xi^{3/2} \frac{1}{\sqrt{\pi}} \int_{-\infty}^{\infty} d\tau e^{-j\xi\tau} \frac{-R_w q_m}{(R_w - q_m)}, \qquad (2.30)
\end{aligned}
$$

where $q_m = -jm\Lambda^{-1}$, $q_e = -jm\Lambda$, and $\Lambda = Z_s/Z_0$ is the normalized surface impedance. The details of the asymptotic solution can be found in Appendix D.2.

Reduction of UTD Based Solution to the Limiting Case of a PEC Sphere

When surface impedance goes to zero ($Z_s \to 0$),

$$
\begin{aligned}
\lim_{Z_s \to 0} \frac{1}{(R_w - q_e)} &= \lim_{Z_s \to 0} \frac{1}{\frac{W_2'(\tau)}{W_2(\tau)} + jm\frac{Z_s}{Z_0}} \\
&= \frac{W_2(\tau)}{W_2'(\tau)} \qquad (2.31)
\end{aligned}
$$

$$\begin{aligned}\lim_{Z_s\to 0}\frac{-R_w q_m}{(R_w-q_m)} &= \lim_{Z_s\to 0}\frac{\frac{W_2'(\tau)}{W_2(\tau)}jm\frac{Z_0}{Z_s}}{\frac{W_2'(\tau)}{W_2(\tau)}+jm\frac{Z_0}{Z_s}} \\ &= \frac{W_2'(\tau)}{W_2(\tau)}. \end{aligned} \tag{2.32}$$

Therefore, the Fock type integrals given by (2.29)-(2.30) reduce to

$$\lim_{Z_s\to 0} V_z = V = \sqrt{\frac{j\xi}{4\pi}}\int_{-\infty}^{\infty} d\tau e^{-j\xi\tau}\frac{W_2(\tau)}{W_2'(\tau)} \tag{2.33}$$

$$\lim_{Z_s\to 0} U_z = U = e^{j3\pi/4}\xi^{3/2}\frac{1}{\sqrt{\pi}}\int_{-\infty}^{\infty} d\tau e^{-j\xi\tau}\frac{W_2'(\tau)}{W_2(\tau)}. \tag{2.34}$$

which are the Fock type functions given by [10] for the PEC sphere problem. Thus, the final expressions of H_θ and H_ϕ given by (2.27)-(2.28) can be obtained in the limit as $Z_s \to 0$ as

$$\begin{aligned} H_\theta^{\pm} &= \pm p_m\cos\phi\Bigg\{\left[\frac{j}{ks}(1-\frac{2j}{ks})U(\xi)+D^2\frac{j}{ks}V(\xi)\right]DG_0 \\ &\quad -G_0\frac{1}{4m^5\xi}\frac{\partial}{\partial\theta}[DU(\xi)]\Bigg\} \end{aligned} \tag{2.35}$$

$$\begin{aligned} H_\phi^{\pm} &= \mp p_m\sin\phi\Bigg\{\left[(1-\frac{j}{ks})V(\xi)+j^2D^2\frac{U(\xi)}{(ks)^2}\right]DG_0 \\ &\quad +G_0\frac{j}{2m^3}\frac{\partial}{\partial\theta}[DV(\xi)]\Bigg\}. \end{aligned} \tag{2.36}$$

When (2.35) and (2.36) are compared with the UTD based solution for a PEC sphere developed in [10], the third terms in both (2.35) and (2.36) (i.e., the terms that contain the derivative with respect to θ) are extra, and include some higher order terms and derivatives of the Fock type integrals, U and V. These extra terms were neglected in [10].

2.2.3 Caustic Corrections

When the field point on the spherical surface is at $\theta=\pi$, it forms a caustic for the surface fields and the tangential magnetic field expressions given by (2.27) and (2.28) are not valid due to the D expression (when $\theta\to\pi$, $D\to\infty$). Therefore, the caustic correction methodology followed in this dissertation is similar to that performed for PEC sphere problem in [10]. Briefly, in (2.27)-(2.28) the expressions have either DG_0 or D^3G_0 type combinations, and are replaced by the following approximate expressions provided by [10]:

$$D^+G_0 + D^-G_0 \approx \frac{k^2Y_0}{2\pi j}\left[\pi m^{3/2} e^{-j2\pi m^3} J_0(2m^3(\pi-\theta))\right]\frac{2e^{j\pi/4}}{ks^+} \tag{2.37}$$

$$[D^+]^3G_0 + [D^-]^3G_0 \approx \frac{k^2Y_0}{2\pi j}\left[2\pi^2 m^{9/2} e^{-j2\pi m^3} \frac{J_1(2m^3(\pi-\theta))}{2m^3(\pi-\theta)}\right]\frac{2e^{j3\pi/4}}{ks^+} \tag{2.38}$$

where J_0 and J_1 are the cylindrical Bessel functions.

Chapter 3

Generalization to arbitrary smooth convex impedance surfaces

3.1 PEC Surface

The UTD-based asymptotic surface field expresssions for PEC cannonical geometries (circular cylinder and sphere) are given in Chapter 2. Surface fields on arbitrary convex PEC surfaces are obtained by generalizing the surface field expressions of the PEC cylinder and sphere [10, 11]. A brief summary of this work is given in the following subsection (3.1.1).

3.1.1 Generalization to arbitrary convex surfaces

A step-by-step procedure is followed for obtaining the surface field expressions on arbitrary convex PEC surfaces. The steps are:

1. Transformation of surface field expressions to $(\hat{n}, \hat{b}, \hat{t})$ coordinates

2. Arrangement of the cylinder solution
3. Generalization of necessary parameters
4. Blending the sphere and cylinder solutions

Step 1: Transformation of surface field expressions to $(\hat{n}, \hat{b}, \hat{t})$ coordinates

To generalize these surface magnetic field expressions, it is better to write the expressions in normal, binormal, tangent $[(\hat{n}, \hat{b}, \hat{t})]$ coordinates. $(\hat{n}, \hat{b}, \hat{t})$ form a right-handed orthonormal basis ($\hat{b} = \hat{t} \times \hat{n}$) and change direction along the ray according to the curvature and torsion of the ray.

Since sphere solution is written in $(\hat{n}, \hat{b}, \hat{t})$ coordiantes, there is no need for the transformation. The surface field expressions on a cylinder can be written in $(\hat{n}, \hat{b}, \hat{t})$ coordinates as follows:

$$\vec{H}_c = \vec{P}_m \cdot (\hat{t}'\hat{t}H^c_{tt} + \hat{b}'\hat{t}H^c_{tb} + \hat{t}'\hat{b}H^c_{bt} + \hat{b}'\hat{b}H^c_{bb}). \tag{3.1}$$

Using the following identitites

$$\begin{aligned} \hat{t}' \cdot \hat{z}' &= \hat{t} \cdot \hat{z} = \sin\alpha, \;\; \hat{t}' \cdot \hat{\phi}' = \hat{t} \cdot \hat{\phi} = \cos\alpha \\ \hat{b}' \cdot \hat{z}' &= \hat{b} \cdot \hat{z} = -\cos\alpha, \;\; \hat{b}' \cdot \hat{\phi}' = \hat{b} \cdot \hat{\phi} = \sin\alpha \end{aligned} \tag{3.2}$$

H^c_{tt}, H^c_{tb}, H^c_{bt} and H^c_{bb} terms in (3.1) can be written explicitly as

$$\begin{aligned} H^c_{tt} &= \hat{t}\hat{t}' \cdot \left(\hat{z}'\hat{z}G_{zz} + \hat{z}'\hat{\phi}G_{\phi z} + \hat{\phi}'\hat{z}G_{z\phi} + \hat{\phi}'\hat{\phi}G_{\phi\phi}\right) \\ &= \sin^2\alpha G_{zz} + \sin\alpha\cos\alpha G_{\phi z} + \cos\alpha\sin\alpha G_{z\phi} + \cos^2\alpha G_{\phi\phi} && (3.3) \\ H^c_{tb} &= \hat{t}\hat{b}' \cdot \left(\hat{z}'\hat{z}G_{zz} + \hat{z}'\hat{\phi}G_{\phi z} + \hat{\phi}'\hat{z}G_{z\phi} + \hat{\phi}'\hat{\phi}G_{\phi\phi}\right) \\ &= -\cos\alpha\sin\alpha G_{zz} - \cos^2\alpha G_{\phi z} + \sin^2\alpha G_{z\phi} + \sin\alpha\cos\alpha G_{\phi\phi} && (3.4) \\ H^c_{bt} &= \hat{b}\hat{t}' \cdot \left(\hat{z}'\hat{z}G_{zz} + \hat{z}'\hat{\phi}G_{\phi z} + \hat{\phi}'\hat{z}G_{z\phi} + \hat{\phi}'\hat{\phi}G_{\phi\phi}\right) \\ &= -\sin\alpha\cos\alpha G_{zz} + \sin^2\alpha G_{\phi z} - \cos^2\alpha G_{z\phi} + \cos\alpha\sin\alpha G_{\phi\phi} && (3.5) \\ H^c_{bb} &= \hat{b}\hat{b}' \cdot \left(\hat{z}'\hat{z}G_{zz} + \hat{z}'\hat{\phi}G_{\phi z} + \hat{\phi}'\hat{z}G_{z\phi} + \hat{\phi}'\hat{\phi}G_{\phi\phi}\right) \\ &= \cos^2\alpha G_{zz} - \cos\alpha\sin\alpha G_{\phi z} - \sin\alpha\cos\alpha G_{z\phi} + \sin^2\alpha G_{\phi\phi}. && (3.6) \end{aligned}$$

Inserting (2.3)-(2.6) into (3.1), surface field expression on a PEC cylinder is obtained as follows:

$$
\begin{aligned}
\vec{H}_c &= \vec{P}_m \cdot \left[\hat{b}'\hat{b} \left\{ \left(1 - \frac{j}{ks}\right) V + \left(\frac{j}{ks}\right)^2 V + \tan^2\alpha \frac{j}{ks}[U - V] \right\} \right. \\
&\quad + \hat{t}'\hat{t} \left\{ \frac{j}{ks} V + \frac{j}{ks} U - 2 \left(\frac{j}{ks}\right)^2 V \right\} \\
&\quad \left. + \left[\hat{t}'\hat{b} + \hat{b}'\hat{t}\right] \left\{ \tan\alpha \frac{j}{ks}[U - V] \right\} \right] G_0. \qquad (3.7)
\end{aligned}
$$

Step 2: Arrangement of the cylinder solution

Before the generalization process, two different arrangements are made in the cylinder solution. The first one is the insertion of the divergence factor, D. Since $D = 1$, it does not appear in the cylinder solution. D is heuristically added by inspecting the sphere solution. The second one is the replacement of $\tan\alpha$ with the torsion factor, T_0. T_0 is a purely geometric factor associated with the geodesic surface ray path. It is heuristically defined as the multiplication of the torsion (T) and the radius of curvature (ρ_g), $T_0 = T\rho_g$. For the cylinder geometry, $T_0 = \tan\alpha$.

After these arrangements, cylinder solution can be written as

$$
\begin{aligned}
\vec{H}_c &= \vec{P}_m \cdot \left[\hat{b}'\hat{b} \left\{ \left(1 - \frac{j}{ks}\right) V + D^2 \left(\frac{j}{ks}\right)^2 V + T_0^2 \frac{j}{ks}[U - V] \right\} \right. \\
&\quad + \hat{t}'\hat{t} \left\{ D^2 \frac{j}{ks} V + \frac{j}{ks} U - 2 \left(\frac{j}{ks}\right)^2 V \right\} \\
&\quad \left. + [\hat{t}'\hat{b} + \hat{b}'\hat{t}] \left\{ T_0 \frac{j}{ks}[U - V] \right\} \right] D G_0. \qquad (3.8)
\end{aligned}
$$

Step 3: Generalization of necessary parameters

The parameters such as torsion factor (T_0), Fock parameter (ξ), large parameter (m) do not change along the geodesic path for cylinder and sphere geometries.

However, on an arbitrary surface these parameters can be different on the different points of the geodesic path. For this reason, some of the parameters are integrated over the geodesic path and the others are splitted symmetrically between the source and the observation points to preserve reciprocity.

The torsion factor T_0 is splitted symmetrically between the source and the observation points to preserve reciprocity. Then, a new parameter $\tilde{T_0}$, which denotes the torsion factor of an arbitrary convex surface, is defined as

$$\tilde{T_0}^2 = T_0(Q')T_0(Q) \tag{3.9}$$

where Q' and Q represent the source and the observation points, respectively. Then, the Fock parameter, ξ, and the Fock integrals U and V are generalized. The generalized Fock parameter is given as,

$$\xi = \int_{Q'}^{Q} ds' \frac{m(s')}{\rho_g(s')} \tag{3.10}$$

where

$$m(s') = \left[\frac{k\rho_g(s')}{2}\right]^{1/3} \tag{3.11}$$

in which s' corresponds to any point along the geodesic ray path. The generalized Fock integrals for an arbitrary convex surface are the scaled versions of the ones in the cylinder and sphere expressions. The scale factor is given as follows:

$$\tau = \left[\frac{ks}{2m(Q')m(Q)\xi}\right]^{1/2} . \tag{3.12}$$

Fock type integrals with $\xi^{3/2}$ factor are scaled by τ^3, and the ones with $\xi^{1/2}$ factor are scaled by τ such that

$$\begin{aligned} \tilde{U} &= \tau^3 U && (3.13) \\ \tilde{V} &= \tau V. && (3.14) \end{aligned}$$

Step 4: Blending the sphere and cylinder solutions

In obtaning the surface fields on an arbirary convex surface, the cylinder solution is broken into two parts as follows:

$$H_c = H_c^T + H_c^N \tag{3.15}$$

where H_c^T and H_c^N are the terms with and without the torsion factor, respectively. The terms without the torsion factor and the sphere solution are blended through blending functions Λ_s and Λ_c, and the terms with the torsion factor are taken directly from the cylinder solution such as

$$H = H_c^T + \Lambda_c \cdot H_c^N + \Lambda_s \cdot H_s. \tag{3.16}$$

Finally, the tangential surface magnetic field expression due to a magnetic source, $\vec{P_m}$, on an arbitrary convex PEC surface can be written as

$$\begin{aligned} \vec{H} \;=\; \vec{P_m} \cdot \Bigg\{ & \hat{b}'\hat{b}\left[\left(1-\frac{j}{ks}\right)\tilde{V}(\xi) + D^2\left(\frac{j}{ks}\right)^2 (\Lambda_s\tilde{U}(\xi)+\Lambda_c\tilde{V}(\xi)) \right. \\ & \left. +\tilde{T_0}^2\frac{j}{ks}(\tilde{U}(\xi)-\tilde{V}(\xi))\right] \\ & +\hat{t}'\hat{t}\left[D^2\frac{j}{ks}\tilde{V}(\xi)+\frac{j}{ks}\tilde{U}(\xi)-2\left(\frac{j}{ks}\right)^2(\Lambda_s\tilde{U}(\xi)+\Lambda_c\tilde{V}(\xi))\right] \\ & +(\hat{t}'\hat{b}+\hat{b}'\hat{t})\left[\frac{j}{ks}\tilde{T_0}(\tilde{U}(\xi)-\tilde{V}(\xi))\right]\Bigg\} DG_0. \end{aligned} \tag{3.17}$$

The blending functions, Λ_s and Λ_c, are introduced heuristically and have the following properties

$$\Lambda_s + \Lambda_c = 1, \qquad \Lambda_s = \begin{cases} 1, & \text{sphere} \\ 0, & \text{cylinder} \end{cases}, \qquad \Lambda_c = \begin{cases} 0, & \text{sphere} \\ 1, & \text{cylinder} \end{cases}.$$

Λ_s is chosen to be

$$\Lambda_s = \left| \sqrt{\frac{R_2(Q')}{R_1(Q')} . \frac{R_2(Q)}{R_1(Q)}} \right| \tag{3.18}$$

where R_1 and R_2 are the principal radii of curvature in the principal surface directions $\tilde{\tau}_1$ and $\tilde{\tau}_2$.

3.2 Impedance Surface

The UTD-based asymptotic surface field expresssions for cannonical geometries (circular cylinder and sphere) with impedance surfaces are given in Chapter 2.

These expresssions contain the derivatives of Fock type integrals. Working with these terms (i.e., the terms that involve the derivatives of Fock type integrals) is intractable in the generalization process. Therefore, in the course of obtaining surface field expressions for arbitrary convex impedance surfaces, these derivative terms that appear in the cannonical geometries with impedance surfaces (i.e., impedance circular cylinder and impedance sphere) are not included.

3.2.1 Expressions for cannonical problems

The UTD-based asymptotic Green's function representations for a tangential magnetic source on an impedance cylinder/sphere that are used in the course of obtaining surface field expressions for arbitrary convex impedance surfaces are simplified as follows without the derivative terms:

Impedance cylinder

Starting with (2.10)-(2.13) and discarding all the derivative terms, the UTD-based asymptotic representations for the components of the Green's function for a tangential magnetic source on an impedance cylinder are simplified as

$$G_{zz} \sim G_0\left\{\cos^2\alpha V_0 + \frac{j}{ks}\left(1-\frac{j}{ks}\right)\left(2-3\cos^2\alpha\right)V_0\right\} \tag{3.19}$$

$$G_{z\phi} \sim -G_0\left\{\cos\alpha\sin\alpha\left[1-\frac{j3}{ks}\left(1-\frac{j}{ks}\right)\right]Y_0\right\} \tag{3.20}$$

$$G_{\phi z} \sim -G_0\left\{\cos\alpha\sin\alpha\left[X_0+V_0-\frac{j3}{ks}\left(1-\frac{j}{ks}\right)V_0\right]\right\} \tag{3.21}$$

$$\begin{aligned} G_{\phi\phi} \sim\ & G_0\left\{\sin^2\alpha Y_0 + \frac{j}{ks}\left(1-\frac{j}{ks}\right)\left(2-3\sin^2\alpha\right)Y_0\right. \\ & \left. +\frac{j}{ks}\frac{1}{\cos^2\alpha}\left(U_0-Y_0\right)\right\}. \end{aligned} \tag{3.22}$$

The V_0, Y_0, X_0, and U_0 terms in the above equations are given in (2.14)-(2.17).

Impedance sphere

Starting with (2.27) and (2.28) and discarding all the derivative terms, the UTD-based asymptotic representations for the components of the Green's function for a tangential magnetic source on an impedance sphere are simplified as

$$H^s_{tt} = \left[\frac{j}{ks}(1-\frac{2j}{ks})U_z + D^2\frac{j}{ks}V_z\right]DG_0 \tag{3.23}$$

$$H^s_{bb} = \left[(1-\frac{j}{ks})V_z + j^2D^2\frac{U_z}{(ks)^2}\right]DG_0 \tag{3.24}$$

where V_z and U_z are given in (2.29)-(2.30). The $p_m \cos\alpha$ and $-p_m \sin\alpha$ terms in tangential magnetic field components [(2.27)-(2.28)] are not included in (3.23) and (3.24) because they are the consequences of $\vec{P_m} \cdot \hat{t}$ and $\vec{P_m} \cdot \hat{b}$, respectively ($\vec{P_m}$ is in the $\hat{x}$ direction). Since $\alpha = 0$ (the angle between s and principal surface direction, $\hat{\theta}$) for sphere, U_z, and V_z terms in the above equations can be expressed as

$$V_z = V_0\Big|_{\alpha=0} . \tag{3.25}$$

$$U_z = U_0\Big|_{\alpha=0} \tag{3.26}$$

Since Fock type integrals for sphere are in the same form with the ones in cylinder expressions, impedance sphere solution can be cast into the following form:

$$H^s_{tt} = \left[\frac{j}{ks}(1-\frac{2j}{ks})U_0 + D^2\frac{j}{ks}V_0\right]DG_0 \tag{3.27}$$

$$H^s_{bb} = \left[(1-\frac{j}{ks})V_0 + j^2D^2\frac{U_0}{(ks)^2}\right]DG_0 \tag{3.28}$$

3.2.2 Generalization to arbitrary convex surfaces

The procedure followed for obtaining the surface field expressions on an arbitrary convex impedance surface is similar to that of the PEC case. The steps are summarized as follows:

Step 1: Transformation of surface field expressions to $(\hat{n},\hat{b},\hat{t})$ coordinates

Since sphere solution is written in $(\hat{n},\hat{b},\hat{t})$ coordiantes, there is no need for the transformation. The surface field expressions on a cylinder can be written in $(\hat{n},\hat{b},\hat{t})$ coordinates as follows:

$$\vec{H}_c = \vec{P}_m \cdot (\hat{t}'\hat{t}H^c_{tt} + \hat{b}'\hat{t}H^c_{tb} + \hat{t}'\hat{b}H^c_{bt} + \hat{b}'\hat{b}H^c_{bb}). \tag{3.29}$$

Prior to the transformation of cylinder expressions to $(\hat{n},\hat{b},\hat{t})$ coordinates, a new Fock type integral, R_0, is defined as follows:

$$R_0 = Y_0 - V_0. \tag{3.30}$$

Then, similar to the PEC case inserting (3.19)-(3.22) together with (3.30) into (3.3)-(3.6), tangential magnetic field on an impedance cylinder can be written as

$$\begin{aligned}
\vec{H}_c \;=\; \vec{P}_m \cdot \Bigg[& \hat{t}'\hat{t}\Bigg\{ \frac{j}{ks}V_0 + \frac{j}{ks}U_0 - 2\left(\frac{j}{ks}\right)^2 V_0 - \frac{j}{ks}R_0 \\
& +2\cos^2\alpha\frac{j}{ks}\left(1-\frac{j}{ks}\right)R_0 - \sin^2\alpha\cos^2\alpha X_0 \Bigg\} \\
& +\hat{b}'\hat{t}\Bigg\{ \tan\alpha\frac{j}{ks}[U_0 - V_0] - \tan\alpha\frac{j}{ks}R_0 \\
& +2\sin\alpha\cos\alpha\frac{j}{ks}\left(1-\frac{j}{ks}\right)R_0 + \cos^3\alpha\sin\alpha X_0 \Bigg\} \\
& +\hat{t}'\hat{b}\Bigg\{ \tan\alpha\frac{j}{ks}[U_0 - V_0] - \tan\alpha\frac{j}{ks}R_0 \\
& +\sin\alpha\cos\alpha\left[1-\frac{j}{ks}\left(1-\frac{j}{ks}\right)\right]R_0 - \sin^3\alpha\cos\alpha X_0 \Bigg\} \\
& +\hat{b}'\hat{b}\Bigg\{ \left(1-\frac{j}{ks}\right)V_0 + \left(\frac{j}{ks}\right)^2 V_0 + \tan^2\alpha\frac{j}{ks}[U_0 - V_0] - \tan^2\alpha\frac{j}{ks}R_0 \\
& +\sin^2\alpha\left[1-\frac{j}{ks}\left(1-\frac{j}{ks}\right)\right]R_0 + \sin^2\alpha\cos^2\alpha X_0 \Bigg\}\Bigg] G_0.
\end{aligned} \tag{3.31}$$

Step 2: Arrangement of the cylinder solution

Before the generalization process, two different arrangements are made in the cylinder solution. These are the insertion of the divergence factor and the torsion factor to the cylinder solution. After these arrangements, cylinder solution can be written as

$$
\begin{aligned}
\vec{H}_c \;=\; \vec{P}_m \cdot \Bigg[& \hat{t}'\hat{t}\Bigg\{ D^2 \frac{j}{ks} V_0 + \frac{j}{ks} U_0 - 2\left(\frac{j}{ks}\right)^2 V_0 - \frac{j}{ks} R_0 \\
& + 2\cos^2\alpha \frac{j}{ks}\left(1 - \frac{j}{ks}\right) R_0 - \sin^2\alpha\cos^2\alpha X_0 \Bigg\} \\
& + \hat{b}'\hat{t}\Bigg\{ T_0 \frac{j}{ks}[U_0 - V_0] - T_0 \frac{j}{ks} R_0 \\
& + 2\sin\alpha\cos\alpha \frac{j}{ks}\left(1 - \frac{j}{ks}\right) R_0 + \cos^3\alpha\sin\alpha X_0 \Bigg\} \\
& + \hat{t}'\hat{b}\Bigg\{ T_0 \frac{j}{ks}[U_0 - V_0] - T_0 \frac{j}{ks} R_0 \\
& + \sin\alpha\cos\alpha \left[1 - \frac{j}{ks}\left(1 - \frac{j}{ks}\right)\right] R_0 - \sin^3\alpha\cos\alpha X_0 \Bigg\} \\
& + \hat{b}'\hat{b}\Bigg\{ \left(1 - \frac{j}{ks}\right) V_0 + D^2 \left(\frac{j}{ks}\right)^2 V_0 + T_0^2 \frac{j}{ks}[U_0 - V_0] - T_0^2 \frac{j}{ks} R_0 \\
& + \sin^2\alpha \left[1 - \frac{j}{ks}\left(1 - \frac{j}{ks}\right)\right] R_0 + \sin^2\alpha\cos^2\alpha X_0 \Bigg\}\Bigg] D G_0. \qquad (3.32)
\end{aligned}
$$

Step 3: Generalization of parameters

In the PEC case, $\sin\alpha$ and $\cos\alpha$ expressions dissappear after the transformation to $(\hat{n}, \hat{b}, \hat{t})$ coordinates. However, this does not happen in the impedance cylinder case. $\sin\alpha$ and $\cos\alpha$ expressions are present. It has to be revealed whether α is the angle between the geodesic path and the principal surface direction at the source point or at the observation point. Therefore, we define α_1 and α_2 as the angles between the geodesic ray path and the principal surface direction at the source and the observation point, respectively. Then, inspecting

$$\begin{aligned}
H^c_{tt} &= \hat{t}\hat{t}' \cdot \left(\hat{z}'\hat{z}G_{zz} + \hat{z}'\hat{\phi}G_{\phi z} + \hat{\phi}'\hat{z}G_{z\phi} + \hat{\phi}'\hat{\phi}G_{\phi\phi}\right) \\
&= \sin\alpha_1 \sin\alpha_2 G_{zz} + \sin\alpha_1 \cos\alpha_2 G_{\phi z} + \cos\alpha_1 \sin\alpha_2 G_{z\phi} \\
&\quad + \cos\alpha_1 \cos\alpha_2 G_{\phi\phi} \qquad (3.33) \\
H^c_{tb} &= \hat{t}\hat{b}' \cdot \left(\hat{z}'\hat{z}G_{zz} + \hat{z}'\hat{\phi}G_{\phi z} + \hat{\phi}'\hat{z}G_{z\phi} + \hat{\phi}'\hat{\phi}G_{\phi\phi}\right) \\
&= -\cos\alpha_1 \sin\alpha_2 G_{zz} - \cos\alpha_1 \cos\alpha_2 G_{\phi z} + \sin\alpha_1 \sin\alpha_2 G_{z\phi} \\
&\quad + \sin\alpha_1 \cos\alpha_2 G_{\phi\phi} \qquad (3.34) \\
H^c_{bt} &= \hat{b}\hat{t}' \cdot \left(\hat{z}'\hat{z}G_{zz} + \hat{z}'\hat{\phi}G_{\phi z} + \hat{\phi}'\hat{z}G_{z\phi} + \hat{\phi}'\hat{\phi}G_{\phi\phi}\right) \\
&= -\sin\alpha_1 \cos\alpha_2 G_{zz} + \sin\alpha_1 \sin\alpha_2 G_{\phi z} - \cos\alpha_1 \cos\alpha_2 G_{z\phi} \\
&\quad + \cos\alpha_1 \sin\alpha_2 G_{\phi\phi} \qquad (3.35) \\
H^c_{bb} &= \hat{b}\hat{b}' \cdot \left(\hat{z}'\hat{z}G_{zz} + \hat{z}'\hat{\phi}G_{\phi z} + \hat{\phi}'\hat{z}G_{z\phi} + \hat{\phi}'\hat{\phi}G_{\phi\phi}\right) \\
&= \cos\alpha_1 \cos\alpha_2 G_{zz} - \cos\alpha_1 \sin\alpha_2 G_{\phi z} - \sin\alpha_1 \cos\alpha_2 G_{z\phi} \\
&\quad + \sin\alpha_1 \sin\alpha_2 G_{\phi\phi}. \qquad (3.36)
\end{aligned}$$

together with the following identitites

$$\begin{aligned}
\hat{t}' \cdot \hat{z}' &= \sin\alpha_1, \quad \hat{t}' \cdot \hat{\phi}' = \cos\alpha_1, \quad \hat{b}' \cdot \hat{z}' = -\cos\alpha_1, \quad \hat{b}' \cdot \hat{\phi}' = \sin\alpha_1 \\
\hat{t} \cdot \hat{z} &= \sin\alpha_2, \quad \hat{t} \cdot \hat{\phi} = \cos\alpha_2, \quad \hat{b} \cdot \hat{z} = -\cos\alpha_2, \quad \hat{b} \cdot \hat{\phi} = \sin\alpha_2 \qquad (3.37)
\end{aligned}$$

tangential magnetic field on an impedance cylinder can be obtained as

$$\begin{aligned}
\vec{H}_c \;=\; & \vec{P}_m \cdot \Bigg[\hat{t}'\hat{t} \Bigg\{ D^2 \frac{j}{ks} V_0 + \frac{j}{ks} U_0 - 2\left(\frac{j}{ks}\right)^2 V_0 - \frac{j}{ks} R_0 \\
& +2\cos\alpha_1\cos\alpha_2 \frac{j}{ks}\left(1-\frac{j}{ks}\right) R_0 - \sin\alpha_1\sin\alpha_2\cos\alpha_1\cos\alpha_2 X_0 \Bigg\} \\
& +\hat{b}'\hat{t} \Bigg\{ T_0 \frac{j}{ks}[U_0 - V_0] - T_0 \frac{j}{ks} R_0 \\
& +2\sin\alpha_1\cos\alpha_2 \frac{j}{ks}\left(1-\frac{j}{ks}\right) R_0 + \cos^2\alpha_1\cos\alpha_2\sin\alpha_2 X_0 \Bigg\} \\
& +\hat{t}'\hat{b} \Bigg\{ T_0 \frac{j}{ks}[U_0 - V_0] - T_0 \frac{j}{ks} R_0 \\
& + \sin\alpha_2\cos\alpha_1 \left[1 - \frac{j}{ks}\left(1-\frac{j}{ks}\right)\right] R_0 - \sin^2\alpha_2\sin\alpha_1\cos\alpha_1 X_0 \Bigg\} \\
& +\hat{b}'\hat{b} \Bigg\{ \left(1-\frac{j}{ks}\right) V_0 + D^2 \left(\frac{j}{ks}\right)^2 V_0 + T_0^2 \frac{j}{ks}[U_0 - V_0] \\
& -T_0^2 \frac{j}{ks} R_0 + \sin\alpha_1\sin\alpha_2 \left[1 - \frac{j}{ks}\left(1-\frac{j}{ks}\right)\right] R_0 \\
& + \sin\alpha_1\sin\alpha_2\cos\alpha_1\cos\alpha_2 X_0 \Bigg\} \Bigg] DG_0. \qquad (3.38)
\end{aligned}$$

Moreover, Fock type integrals present in the cylinder and sphere solutions also have $\sin\alpha$ and $\cos\alpha$ terms. For a cylinder, the angle between the geodesic path and principal surface direction, α, does not change along the geodesic path because it has only one curvature in principal directions (singly curved surface). For a sphere, $\alpha = 0$ because torsion is zero. However, α changes along the geodesic path since an arbitrary surface has curvature in the both of the pricipal directions and has nonzero torsion. For this reason, $\cos^2\alpha$ and $\sin^2\alpha$ terms are splitted symmetrically between the source and observation points to preserve the reciprocity. Thus, V_0, Y_0, X_0, and U_0 (Fock type integrals) are generalized to V_0^g, Y_0^g, X_0^g, U_0^g, and R_0^g by generalizing q_e, q_m and q_c^2, which include $\cos^2\alpha$ and $\sin^2\alpha$, as follows:

$$q_e^g = -jm\Lambda\cos\alpha_1\cos\alpha_2 \qquad (3.39)$$

$$q_m^g = -jm\Lambda^{-1}\cos\alpha_1\cos\alpha_2 \tag{3.40}$$

$$q_c^g = -jm\left[\left(1+\frac{\tau}{2m^2\cos\alpha_1\cos\alpha_2}\right)\cos\alpha_1\cos\alpha_2\sin\alpha_1\sin\alpha_2\right]^{1/2}. \tag{3.41}$$

The generalization of the parameters such as torsion factor (T_0), Fock parameter (ξ), large parameter (m) is same as that of the PEC case. For the generalization of the Fock integrals, similar to the PEC case, the Fock integrals with $\xi^{3/2}$ factor are scaled by τ^3, and the ones with $\xi^{1/2}$ factor are scaled by τ such that

$$\tilde{U_0^g} = \tau^3 U_0^g \tag{3.42}$$

$$\tilde{V_0^g} = \tau V_0^g \tag{3.43}$$

$$\tilde{X_0^g} = \tau X_0^g \tag{3.44}$$

$$\tilde{Y_0^g} = \tau Y_0^g \tag{3.45}$$

$$\tilde{R_0^g} = \tau R_0^g. \tag{3.46}$$

Step 4: Blending the sphere and cylinder solutions

Similar to the PEC case, in obtaning the surface fields on an arbirary convex surface, the cylinder solution is broken into two parts as follows:

$$H_c = H_c^T + H_c^N \tag{3.47}$$

where H_c^T and H_c^N are the terms with and without the torsion factor, respectively. The terms without the torsion factor and the sphere solution are blended through blending functions Λ_s and Λ_c, and the terms with the torsion factor are taken directly from the cylinder solution such as

$$H = H_c^T + \Lambda_c \cdot H_c^N + \Lambda_s \cdot H_s. \tag{3.48}$$

Finally, the tangential surface magnetic field expression due to a magnetic source, $\vec{P_m}$, on an arbitrary convex impedance surface can be written as

$$
\begin{aligned}
\vec{H} \;=\; & \vec{P_m}\cdot\Bigg\{\hat{t}'\hat{t}\Bigg[D^2\frac{j}{ks}\tilde{V}_0^g+\frac{j}{ks}\tilde{U}_0^g-2\left(\frac{j}{ks}\right)^2(\Lambda_s\tilde{U}_0^g+\Lambda_c\tilde{V}_0^g+\Delta_{tt}\Bigg] \\
& +\hat{b}'\hat{t}\left[\frac{j}{ks}\tilde{T}_0(\tilde{U}_0^g-\tilde{V}_0^g)+\Delta_{tb}\right]+\hat{t}'\hat{b}\left[\frac{j}{ks}\tilde{T}_0(\tilde{U}_0^g-\tilde{V}_0^g)+\Delta_{bt}\right] \\
& +\hat{b}'\hat{b}\Bigg[\left(1-\frac{j}{ks}\right)\tilde{V}_0^g+D^2\left(\frac{j}{ks}\right)^2(\Lambda_s\tilde{U}_0^g+\Lambda_c\tilde{V}_0^g) \\
& +\tilde{T}_0^{\,2}\frac{j}{ks}(\tilde{U}_0^g-\tilde{V}_0^g)+\Delta_{bb}\Bigg]\Bigg\}DG_0 \qquad (3.49)
\end{aligned}
$$

where

$$
\begin{aligned}
\Delta_{tt} \;=\; & \Lambda_c\Bigg[-\frac{j}{ks}\tilde{R}_0^g+2\cos\alpha_1\cos\alpha_2\frac{j}{ks}\left(1-\frac{j}{ks}\right)\tilde{R}_0^g \\
& -\sin\alpha_1\sin\alpha_2\cos\alpha_1\cos\alpha_2\tilde{X}_0^g\Bigg] \qquad (3.50)
\end{aligned}
$$

$$
\begin{aligned}
\Delta_{tb} \;=\; & -\tilde{T}_0\frac{j}{ks}\tilde{R}_0^g+\Lambda_c\Bigg[2\sin\alpha_1\cos\alpha_2\frac{j}{ks}\left(1-\frac{j}{ks}\right)\tilde{R}_0^g \\
& +\cos^2\alpha_1\cos\alpha_2\sin\alpha_2\tilde{X}_0^g\Bigg] \qquad (3.51)
\end{aligned}
$$

$$
\begin{aligned}
\Delta_{bt} \;=\; & -\tilde{T}_0\frac{j}{ks}\tilde{R}_0^g+\Lambda_c\Bigg[\sin\alpha_2\cos\alpha_1\left[1-\frac{j}{ks}\left(1-\frac{j}{ks}\right)\right]\tilde{R}_0^g \\
& -\sin^2\alpha_2\sin\alpha_1\cos\alpha_1\tilde{X}_0^g\Bigg] \qquad (3.52)
\end{aligned}
$$

$$
\begin{aligned}
\Delta_{bb} \;=\; & -\tilde{T}_0^{\,2}\frac{j}{ks}\tilde{R}_0^g+\Lambda_c\Bigg[\sin\alpha_1\sin\alpha_2\left[1-\frac{j}{ks}\left(1-\frac{j}{ks}\right)\right]\tilde{R}_0^g \\
& +\sin\alpha_1\sin\alpha_2\cos\alpha_1\cos\alpha_2\tilde{X}_0^g\Bigg]. \qquad (3.53)
\end{aligned}
$$

Chapter 4

Numerical Results

In this chapter, several numerical results for the surface magnetic field on smooth convex surfaces with an impedance boundary condition are given to illustrate the validity and the accuracy of our proposed UTD solution. Firstly, the validity of the solution is verified by comparing the results obtained by impedance surface solution with those of PEC surfaces in the limiting case where $Z_s \to 0$. For this reason, numerical results related to surface fields on smooth convex PEC surfaces in the literature are duplicated. Later, simulation tools such as HFSS, FEKO and CST are used to verify the smooth convex PEC and impedance surface results. Reasonable agreemnet in PEC surface results are achieved with these simulation tools. However, no reasonable result was attained for the impedance surfaces. Morever, we are working with other groups in order to get numerical results for impedance surfaces from their in house FEM/FDTD programs. However, an outcome have not obtained from this collaboration yet.

The organization of this chapter is as follows: In Section 4.1, surface field results on smooth convex PEC surfaces given in the literature are compared with our calculated PEC surface results. Comparisons of surface field excited on various geometries such as general parabolic cylinder, elliptic cylinder, general paraboloid of revolution, etc. in the limiting case with those of PEC surfaces are given in Section 4.2. Finally, results obtained with the simulation tools are given and possible sources of errors are investigated to figure out the inconsistency in the results in Section 4.3.

4.1 PEC Surfaces

In this section, the arbitrary smooth convex surface solution is specialized to the various geometries and the mutual admidtance between two slots on different geometries is calculated. Since arbitary convex PEC surface solution is used for the verification of the surface fields for impedance surfaces for the limiting case, $Z_s \rightarrow 0$, the arbitrary convex PEC surface solution is specialized to different geometries and the results in the literaure are regenerated.

Firstly, the geometric parameters (i.e.,radii of curvature, torsion, Fock parameter, etc.) of the geometry, which are necesssary for the UTD solution, are calculated. The details of the calculation of these parameters are given in Appendix E. By the help of these parameters pertaining to the geometry, tangential magnetic field expressions are obtained. Finally, the mutual admidtance between the slots/apertures are calculated by substituting these tangential magnetic field components into

$$Y_{12} = -\frac{1}{V_1 V_2} \int_{S_2} \int_{S_1} \bar{M}_2 \cdot \left(\bar{M}_1 \cdot \bar{H} \right) dS_1 dS_2 \tag{4.1}$$

where $\bar{M}_1$ is the magnetic current at source point, $\bar{M}_2$ is the magnetic current at the observation point, $\bar{H}$ is the magnetic field at the observation point due to a point magnetic source at the source point, S_1 and S_2 denote the aperture area of $\bar{M}_1$ and $\bar{M}_2$, respectively. S_{21} is calculated using

$$\overline{S} = \left(\overline{I} - \overline{Y} \right) \left(\overline{I} + \overline{Y} \right)^{-1}. \tag{4.2}$$

In (4.2), $\overline{S}$, $\overline{Y}$ and $\overline{I}$ are the 2×2 scattering, admittance and identity matrices, respectively. Since the source and the observation apertures are identical for the mutual coupling problems studied in this dissertation, $Y_{12} = Y_{21}$ and $Y_{11} = Y_{22}$. $Y_{12} = Y_{21}$ is calculated using (4.1). For the rectangular apertures, a planar

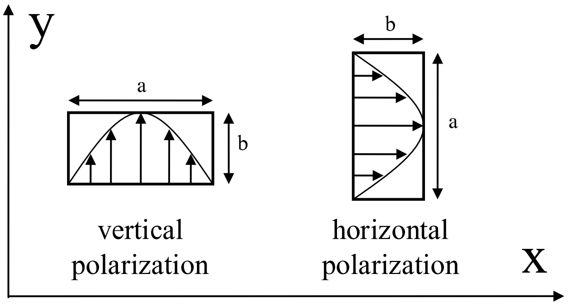

Figure 4.1: Rectangular apertures with the dimensions a and b such that only the TE_{10} mode is generated.

approximation is used for calculating Y_{11} [39] such that

$$\Re Y_{11} = \frac{a}{15\pi^4 k}\int_0^k d\alpha C(\alpha)\beta\left\{\int_0^{\beta b} J_0(t)dt - J_1(\beta b)\right\} \tag{4.3}$$

$$\Im Y_{11} = \frac{-a}{15\pi^4 k}\left\{\int_0^k d\alpha C(\alpha)\beta\left(\int_0^{\beta b} Y_0(t)dt - Y_1(\beta b) - \frac{2}{\pi\beta b}\right) + \frac{2}{\pi}\int_k^\infty d\alpha C(\alpha)\gamma\left(\int_0^{\gamma b} K_0(t)dt + K_1(\gamma b) - \frac{1}{\gamma b}\right)\right\} \tag{4.4}$$

where $\Re Y_{11}$ and $\Im Y_{11}$ denote the real and imaginary parts of Y_{11}, respectively. In (4.3) and (4.4), J_0, J_1, Y_0 and Y_1 are cylindrical Bessel functions whereas K_0 and K_1 are modified cylindrical Bessel functions. Finally in (4.3) and (4.4)

$$\beta = (k^2 - \alpha^2)^{1/2}\ , \quad \gamma = (\alpha^2 - k^2)^{1/2}\ , \quad C(\alpha) = \frac{\cos^2(\alpha a/2)}{1-(\alpha a/\pi)^2} \tag{4.5}$$

with a and b being the dimensions of the rectangular aperture as shown in Fig. 4.1, and k is the wavenumber. For the circular aperture, the meaurement result, which is obtained from the authors of [13], is used.

In the course of obtaining the mutual coupling results, the aperture dimensions are adjusted so that the fields at the apertures can be approximated by the dominant modes (TE_{10} for rectangular apertures and TE_{11} for circular apertures). The field distribution for the vertical polarization for TE_{10} mode, as shown in Fig. 4.1, is given by

$$\bar{E} = \hat{y}\cos\left(\frac{\pi}{a}x\right) \tag{4.6}$$

where a is the length of the aperture. Therefore, the magnetic current is related to this electric field by

$$\bar{M} = \bar{E} \times \hat{z} = \hat{x} \cos\left(\frac{\pi}{a} x\right). \tag{4.7}$$

Similarly, the field distribution for the horizontal polarization for TE_{10} mode is given by

$$\bar{E} = \hat{x} \cos\left(\frac{\pi}{a} y\right), \tag{4.8}$$

and the magnetic current for the horizontal polarization can be written as

$$\bar{M} = -\hat{y} \cos\left(\frac{\pi}{a} y\right). \tag{4.9}$$

Finally, for a circular aperture, the field distribution of [R-polarization] for the TE_{11} mode is given by

$$\bar{E} = \hat{\rho} E_\rho + \hat{\phi} E_\phi = \hat{\rho} \frac{1}{\rho} J_1\left(1.841 \frac{\rho}{a}\right) \sin\phi + \hat{\phi} J_1'\left(1.841 \frac{\rho}{a}\right) \cos\phi \tag{4.10}$$

where a is the radius of the aperture, and 1.841 is the first zero of the derivative of $J_1(x)$ ($J_1'(1.841) = 0$). Therefore, the magnetic current is related to this electric field by

$$\begin{aligned}
\bar{M} &= \bar{E} \times \hat{z} = \hat{\rho} M_\rho + \hat{\phi} M_\phi \\
&= \hat{\rho} J_1'\left(1.841 \frac{\rho}{a}\right) \cos\phi - \hat{\phi} \frac{1}{\rho} J_1\left(1.841 \frac{\rho}{a}\right) \sin\phi \\
&= \hat{\rho} \left[\frac{1.841}{a} J_0\left(1.841 \frac{\rho}{a}\right) - J_1\left(1.841 \frac{\rho}{a}\right)\right] \cos\phi \\
&\quad - \hat{\phi} \frac{1}{\rho} J_1\left(1.841 \frac{\rho}{a}\right) \sin\phi.
\end{aligned} \tag{4.11}$$

Similarly, the magnetic current for [ϕ-polarization] of the TE_{11} mode can be written as

$$\begin{aligned}
\bar{M} &= \hat{\rho} \left[\frac{1.841}{a} J_0\left(1.841 \frac{\rho}{a}\right) - \frac{1}{\rho} J_1\left(1.841 \frac{\rho}{a}\right)\right] \cos(\phi - \pi/2) \\
&\quad - \hat{\phi} \frac{1}{\rho} J_1\left(1.841 \frac{\rho}{a}\right) \sin(\phi - \pi/2).
\end{aligned} \tag{4.12}$$

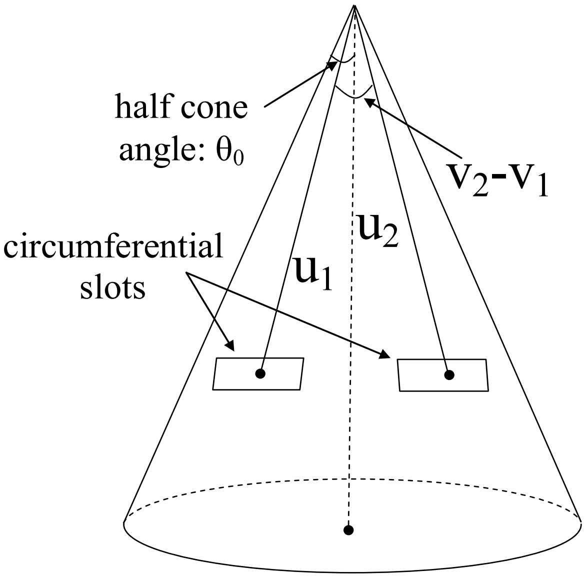

Figure 4.2: Problem geometry for a PEC circular cone that has two circumferential slots on it.

Circular cone geometry

In this section, the arbitrary convex PEC surface solution has been specialized to the cone geometry. Mutual admittances between two circumferential slots on a PEC cone for various configurations are calculated and compared with the results given in [40]. Problem geometry for this configuration is given in Fig. 4.2. The details of all geometrical calculations are given in Appendix E.1.

Using the formulation in (3.17), the mutual admittance between two circumferential slots with slot length= 0.5λ and width= 0.2λ on a cone, which has a 15° half-cone angle, is calculated and plotted as function of angular separation $(v_2 - v_1)$ in Fig. 4.3. The slots are at the same radial poisitions $(u_1 = u_2 = 8\lambda)$. It is seen from the figure that a good agreement with the results given in [40] is achieved for the magnitude and phase of the mutual admidtance.

Another example is the mutual coupling between two circumferential slots with slot length= 0.9", width= 0.4" and angular separation $(v_2 - v_1 = 60.8°)$ on a cone, which has a 12.2° half-cone angle. Comparison of the magnitude of S_{21} between these slots is plotted as function of frequency in Fig. 4.4. The slots

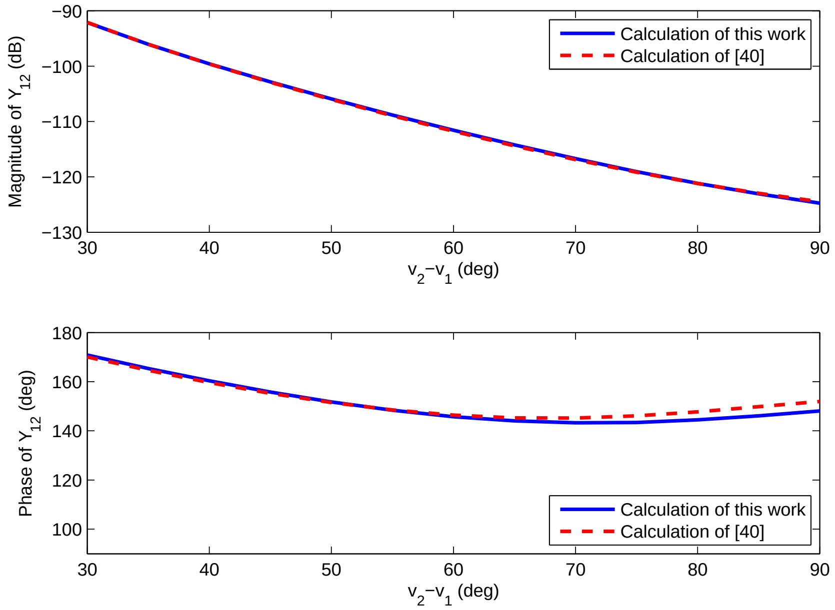

Figure 4.3: Mutual admittance between two circumferential slots with slot length= 0.5λ and width= 0.2λ at radial positions ($u_1 = u_2 = 8\lambda$) on a cone, which has a 15° half-cone angle, as a function of angular separation, $v_2 - v_1$.

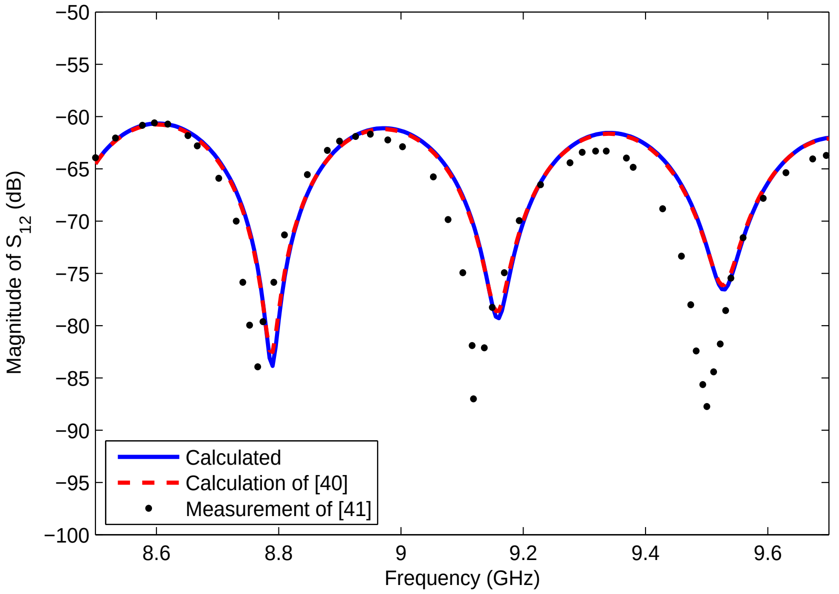

Figure 4.4: Comparison of the magnitude of S_{21} between two circumferential slots with slot ength= 0.9”, width= 0.4” and angular separation ($v_2 - v_1 = 60.8°$) on a cone, which has a 12.2° half-cone angle as function of frequency

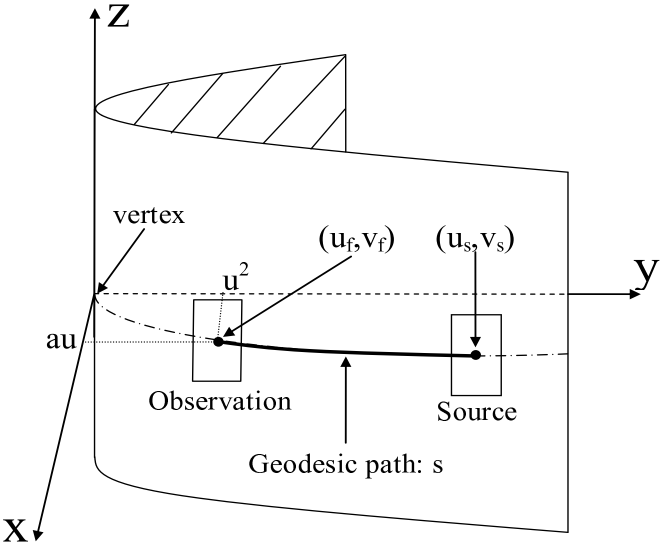

Figure 4.5: Problem geometry for PEC GPCYL

are at the same radial poisitions ($u_1 = u_2 = 45.53cm$). It is seen from the figure that a good agreement with the calculated results given in [40] and measurement data given in [41] is obtained. It should be noted that in order to obtain the interference pattern shown in Fig. 4.4, the diffraction by the cone tip must be included. The tip diffraction formula given in [40] is used for the calculations in this dissertation.

General parabolic cylinder (GPCYL) geometry

In this section, the arbitrary convex PEC surface solution has been specialized to the GPCYL geometry and the mutual coupling between two rectangular apertures with dimensions $0.27\lambda \times 0.65\lambda$ on various GPCYLs is calculated and compared with the results given in [13]. The center of the first aperture (source) is located 5λ away from the vertex of the GPCYL and the center of the second aperture (observation) moves from the first aperture to 5λ away from the vertex of the other side of the GPCYL. The apertures are at the same vertical poisition. Three different geometries are studied for E-plane coupling.

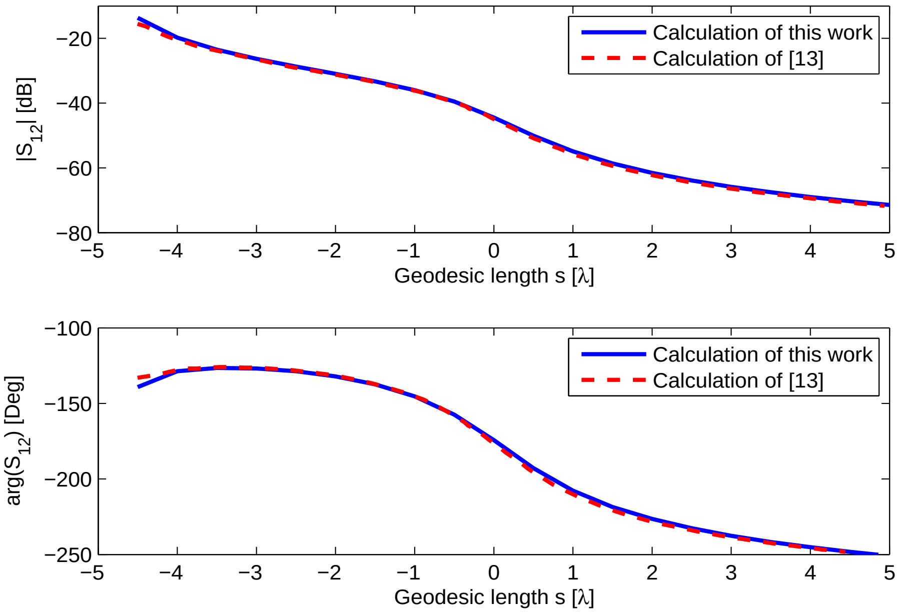

Figure 4.6: Comparison of the magnitude and phase of E-plane coupling between two slots with slot dimensions $0.27\lambda \times 0.65\lambda$ as a function of distance of the second slot to the vertex on Parab.1

- Parab.1: a=1.5, geodesic coordinate for the first slot [(u,v)]: (-1.95,0)
- Parab.2: a=2.3, geodesic coordinate for the first slot [(u,v)]: (-1.687,0)
- Parab.3: a=3.93, geodesic coordinate for the first slot [(u,v)]: (-1.2,0)

Problem geometry is given in Fig. 4.5. The details of all geometrical calculations are given in Appendix E.2.

Comparison of the magnitude and phase of S_{21} between these slots (as a function of the distance of the second slot to the vertex for the geometries given above) with that of given in [13] is plotted in Figs. 4.6-4.8. As it is seen from the figures a good agreement is achieved.

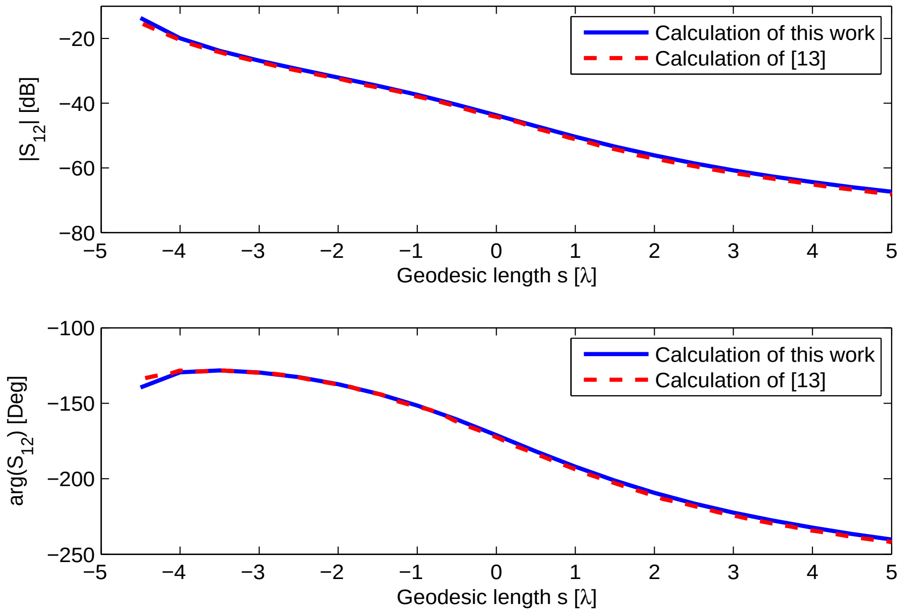

Figure 4.7: Comparison of the magnitude and phase of E-plane coupling between two slots with slot dimensions $0.27\lambda \times 0.65\lambda$ as a function of distance of the second slot to the vertex on Parab.2

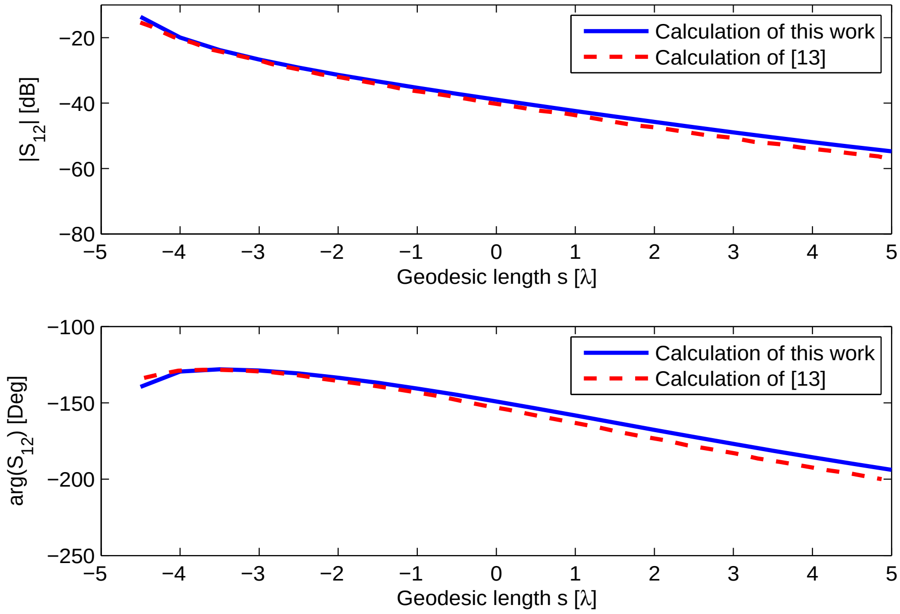

Figure 4.8: Comparison of the magnitude and phase of E-plane coupling between two slots with slot dimensions $0.27\lambda \times 0.65\lambda$ as a function of distance of the second slot to the vertex on Parab.3

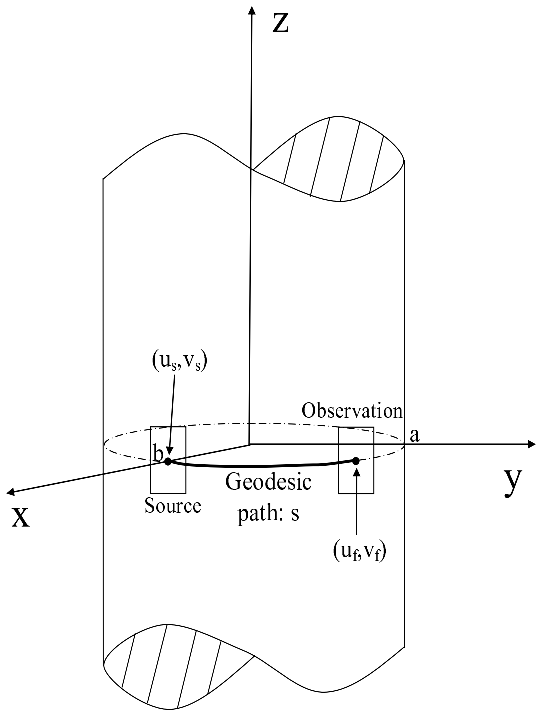

Figure 4.9: Problem geometry for PEC elliptic cylinder

Elliptic cylinder geometry

In this section, the arbitrary convex PEC surface solution has been specialized to the elliptic cylinder geometry and the mutual coupling between two rectangular apertures with dimensions $0.27\lambda \times 0.65\lambda$ on various elliptic cylinders is calculated and compared with the results given in [13]. The center of the first aperture (source) is located at the point $(u, v) = (0, 0)$ and the center of the second aperture (observation) is located at the point $(u, v) = (u_f, 0)$ where u_f changes from 0 to $\pi/2$. Parametric equation for an elliptic cylinder is $(b \cos u, a \sin u, v)$. a is the major axis and b is the minor axis. a/b denotes the ellipticity. Four different geometries are studied for E-plane coupling.

- a/b=1 (corresponds to circular cylinder)
- a/b=1.2
- a/b=2

- a/b=6

The major axis is chosen to be 5λ for all geometries. Problem geometry is given in Fig. 4.9. The details of all geometrical calculations are given in Appendix E.3.

Comparison of the magnitude and phase of S_{21} between these slots as a function of geodesic length for the geometries given above with the results given in [13] is plotted in Figs. 4.10-4.13. As it is seen from the figures a good agreement is achieved. Note that the ripples at far-away separations are caused by the interference of the primary ray and the secondary ray (travelling opposite direction to the primary ray).

General paraboloid of revolution (GPOR) geometry

In this section, the arbitrary convex PEC surface solution has been specialized to the GPOR geometry. Mutual coupling between two circular waveguide fed apertures on PEC GPOR for two different configurations is calculated and compared with the results given in [13]. For both configurations, four different combinations of polarization are examined. They are $[R, R]$, $[R, \phi]$, $[\phi, R]$ and $[\phi, \phi]$. The first entry in the brackets corresponds to the polarization of the source aperture and the second entry corresponds to the polarization of the observation aperture.

As seen in Fig. 4.14, the diameter of the GPOR used in the calculation is approximately $600mm$ with a depth of approximately $175mm$. Therefore, GPOR has a shaping parameter of 3.9225 at $8.975GHz$. The circular waveguide-fed apertures have a diameter of $14.40mm$ (0.2154λ at $8.975GHz$). Self admittance (Y_{11}) is required for the mutual coupling calculations. It ($Y_{11} = 0.001134618472498 - 0.000834412736580j$) is obtained from the authors of [13]. The details of all geometrical calculations are given in Appendix E.4.

For the first configuration, the center of first aperture (source) is located at the point $(u, v) = (0.1998, 50°)$ and the center of second aperture (observation) is located at the point $(u, v) = (u_f, 90°)$ where u_f changes from 0 to 0.4, as shown in Fig. 4.15. Comparison of the magnitude and phase of S_{21} between these slots as

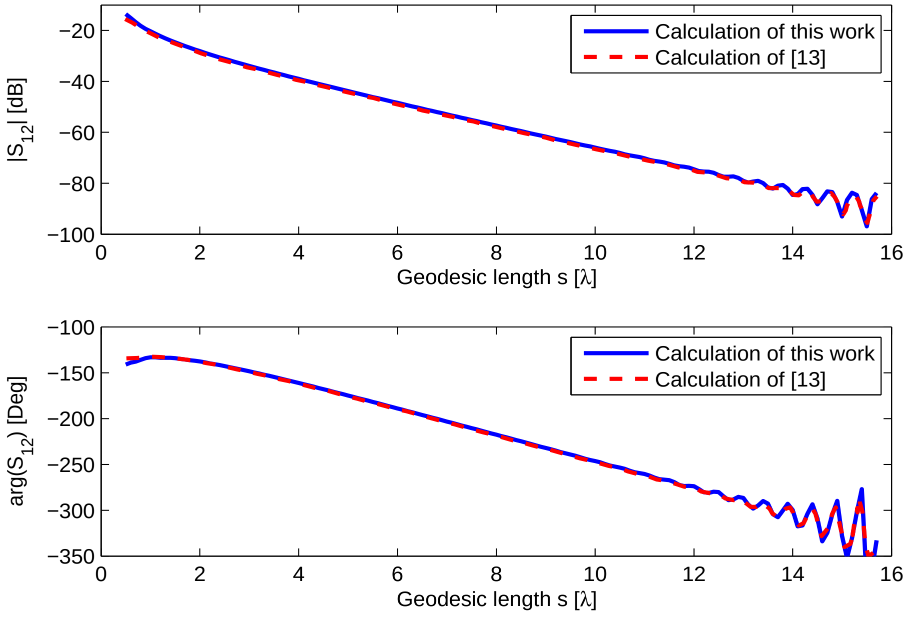

Figure 4.10: Comparison of the magnitude and phase of E-plane coupling between two slots with slot dimensions $0.27\lambda \times 0.65\lambda$ as a function of distance of second slot to the vertex on an elliptic cylinder with $a/b = 1$ (corresponds to circular cylinder)

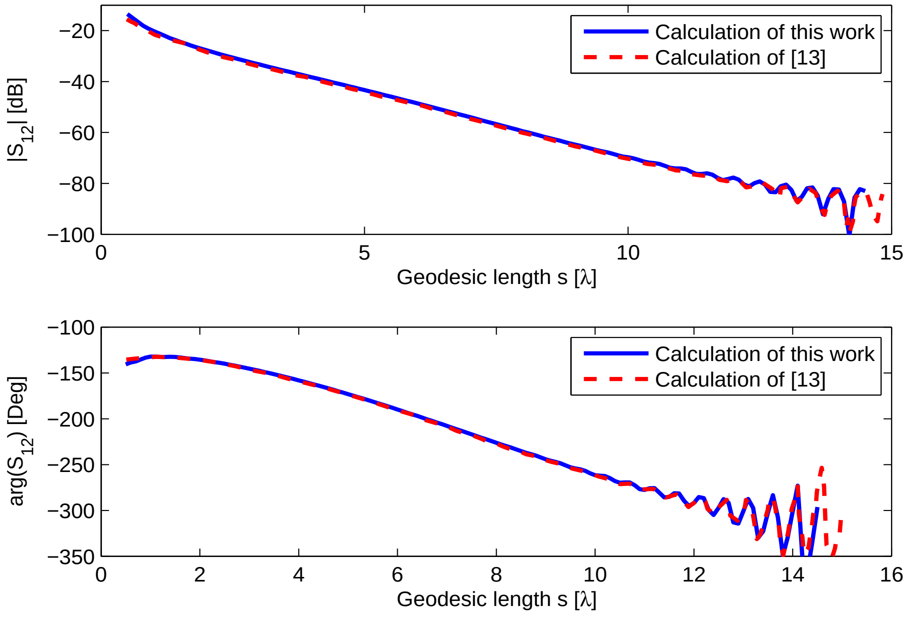

Figure 4.11: Comparison of the magnitude and phase of E-plane coupling between two slots with slot dimensions $0.27\lambda \times 0.65\lambda$ as a function of distance of second slot to the vertex on an elliptic cylinder with $a/b = 1.2$

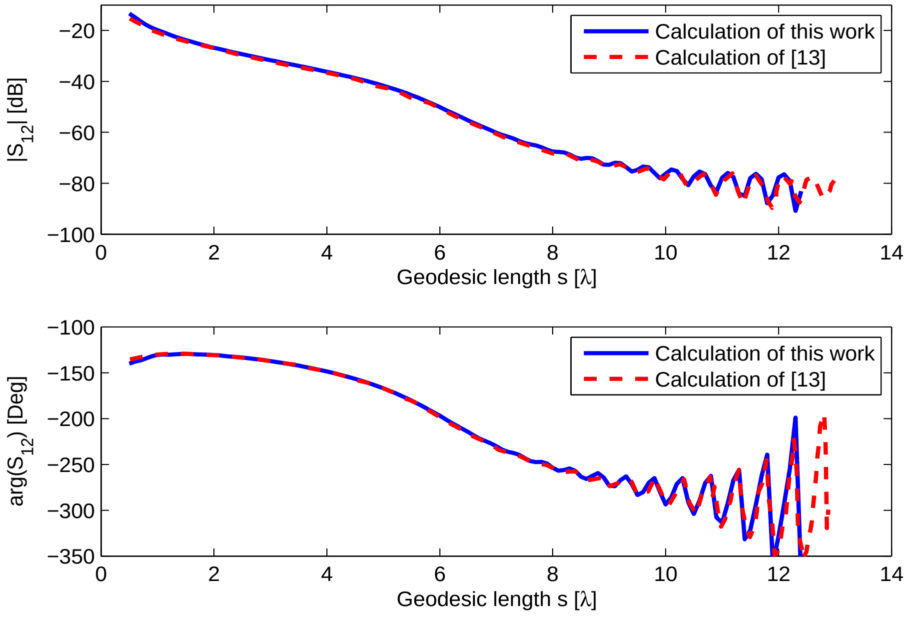

Figure 4.12: Comparison of the magnitude and phase of E-plane coupling between two slots with slot dimensions $0.27\lambda \times 0.65\lambda$ as a function of distance of second slot to the vertex on an elliptic cylinder with $a/b = 2$

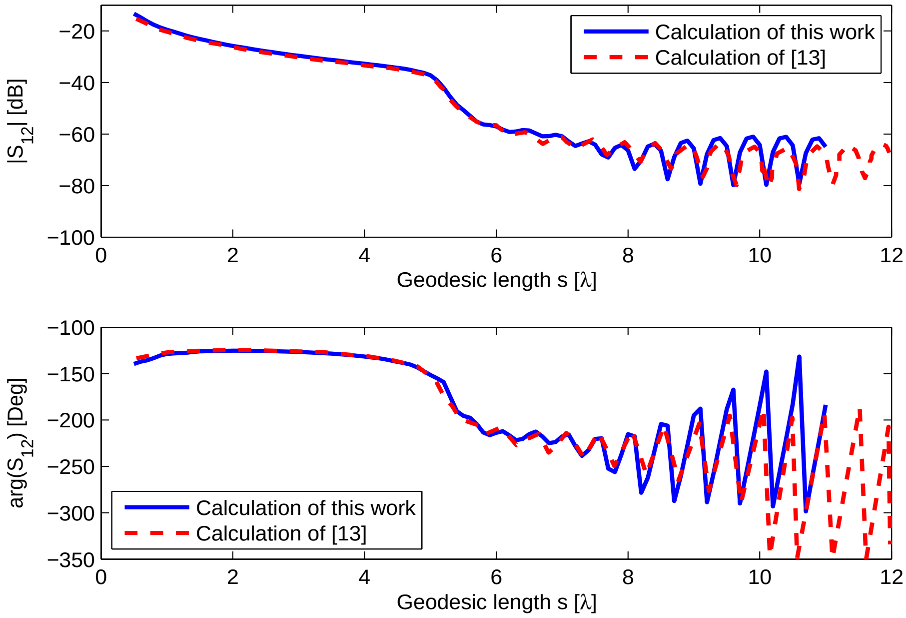

Figure 4.13: Comparison of the magnitude and phase of E-plane coupling between two slots with slot dimensions $0.27\lambda \times 0.65\lambda$ as a function of distance of second slot to the vertex on an elliptic cylinder with $a/b = 6$

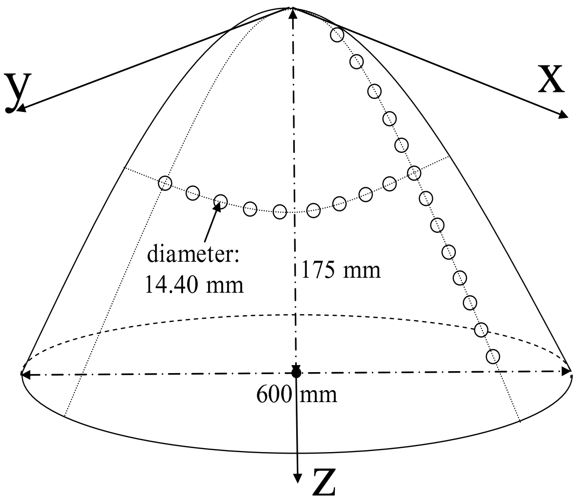

Figure 4.14: Problem geometry for PEC GPOR

a function of u_f with the calculated results and calculation and measurement of [13] is plotted in Figs. 4.17-4.20. As it is seen from the figures a good agreement is achieved.

For the second configuration, the center of first aperture (source) is located at the point $(u, v) = (0.1998, 0°)$ and the center of second aperture (observation) is located at the point $(u, v) = (0.1998, v_f)$ where v_f changes from 10° to 90°, as shown in Fig. 4.16. Comparison of the magnitude and phase of S_{21} between these slots as a function of u_f with the calculated results and measurement data given in [13] is plotted in Figs. 4.21-4.24. As it is seen from these figures a good agreement is achieved.

4.2 Impedance Surfaces

UTD-based asymptotic surface field expression for the arbitrary convex impedance surface is specialized to singly and doubly curved surfaces and numerical results for the surface fields are obtained. Since there is no result for the surface fields for impedance surfaces except cylinder and sphere, in the literature, results for the surface fields for impedance surfaces for the limiting case, $Z_s \to 0$,

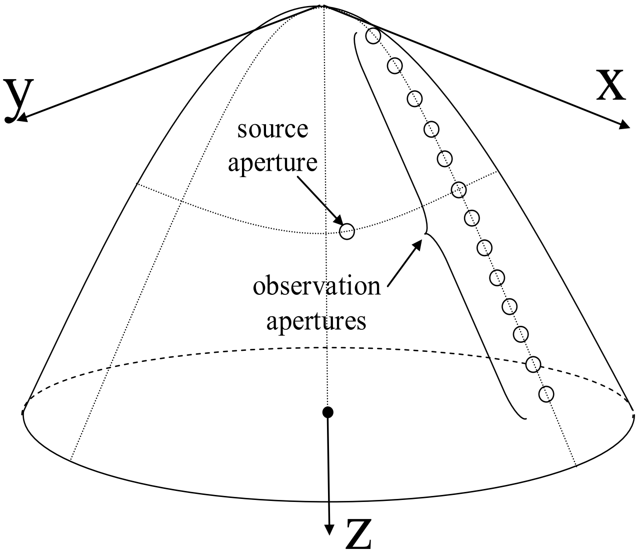

Figure 4.15: Problem geometry for the first configuration

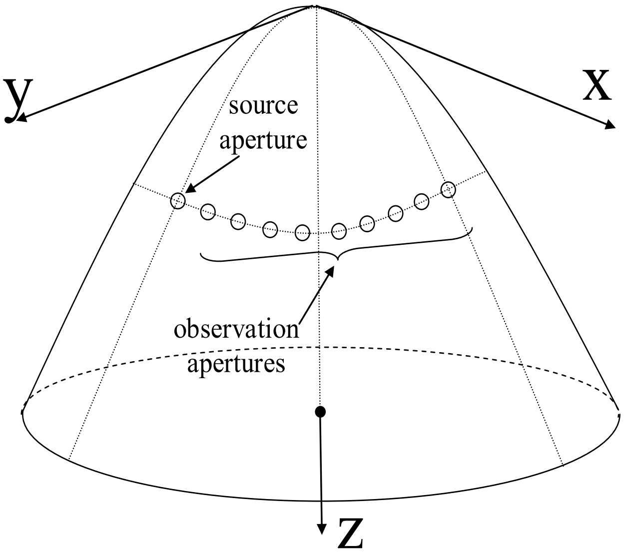

Figure 4.16: Problem geometry for the second configuration

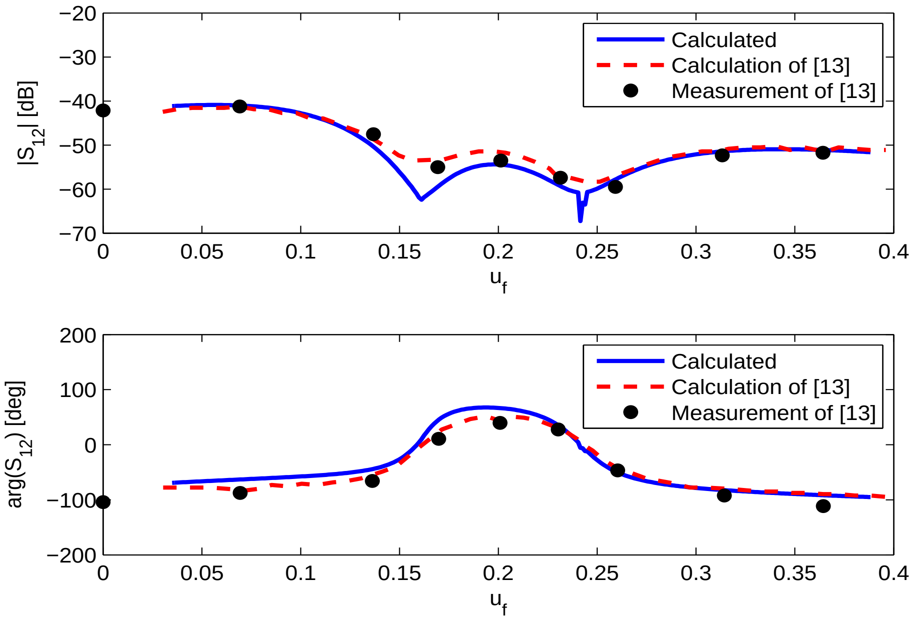

Figure 4.17: Comparison of the magnitude and phase of S_{21} ($[R, R]$ polarization) between two circular waveguide fed apertures as a function of u_f with the calculated results and calculation and measurement of [13] for the first configuration

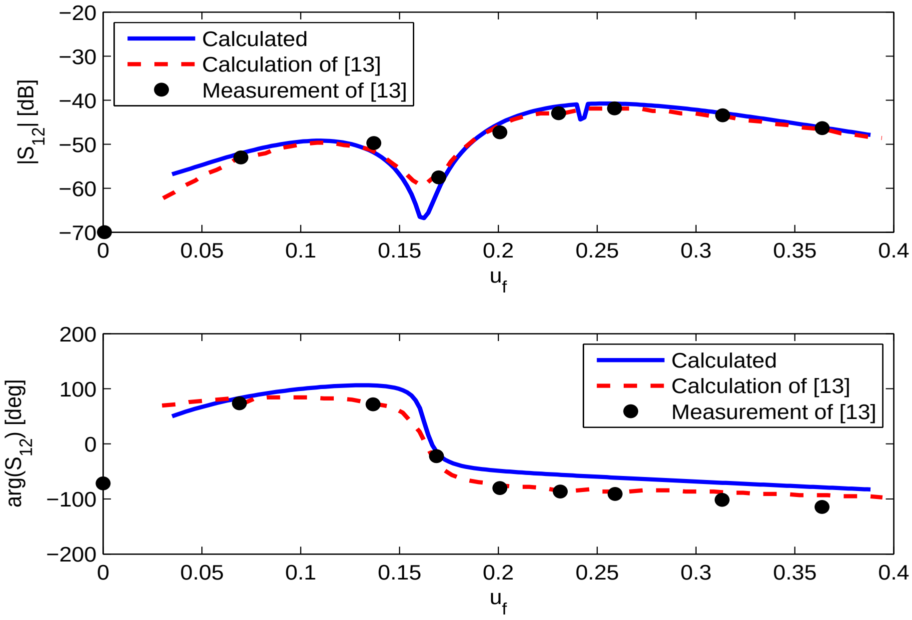

Figure 4.18: Comparison of the magnitude and phase of S_{21} ($[R, \phi]$ polarization) between two circular waveguide fed apertures as a function of u_f with the calculated results and calculation and measurement of [13] for the first configuration

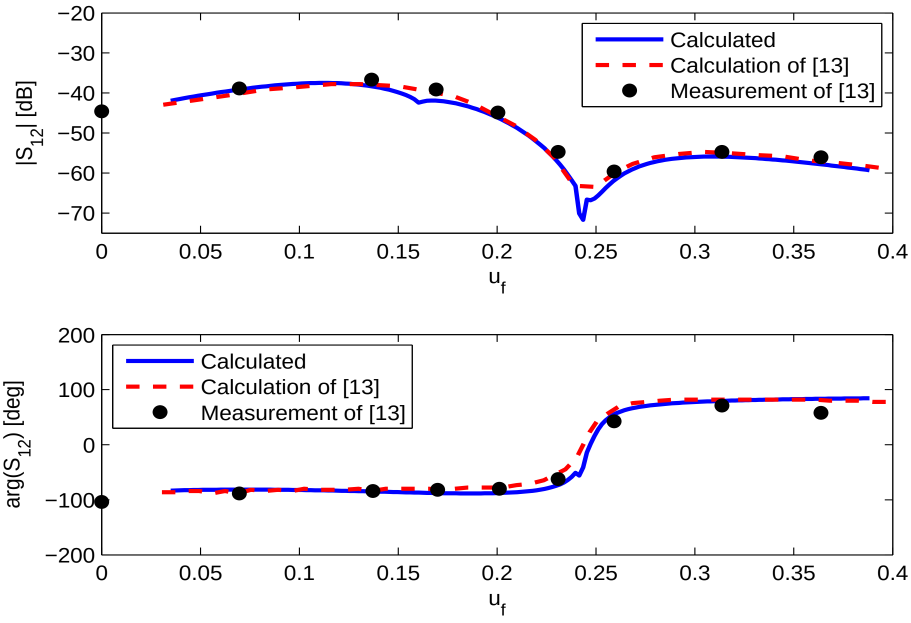

Figure 4.19: Comparison of the magnitude and phase of S_{21} ($[\phi, R]$ polarization) between two circular waveguide fed apertures as a function of u_f with the calculated results and calculation and measurement of [13] for the first configuration

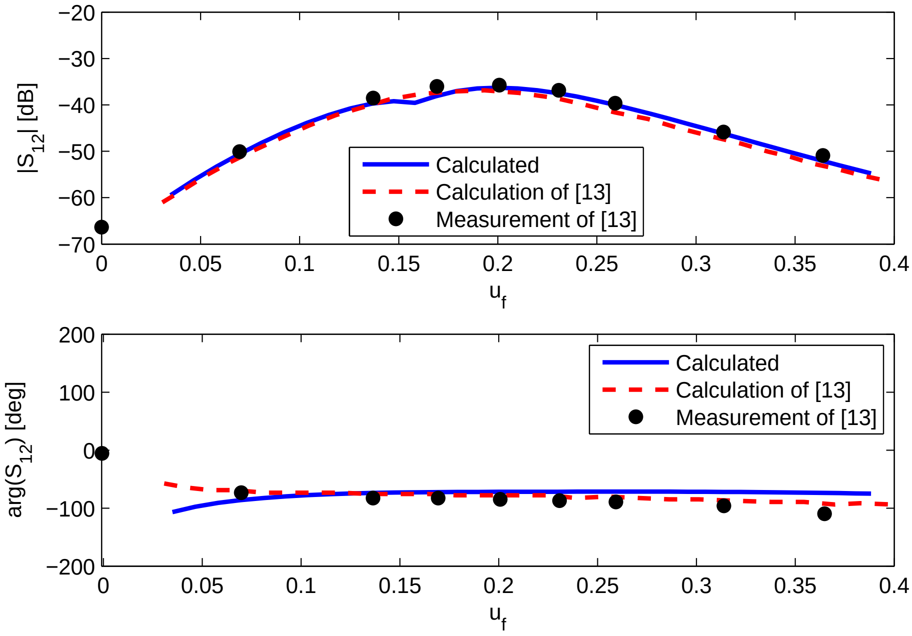

Figure 4.20: Comparison of the magnitude and phase of S_{21} ($[\phi, \phi]$ polarization) between two circular waveguide fed apertures as a function of u_f with the calculated results and calculation and measurement of [13] for the first configuration

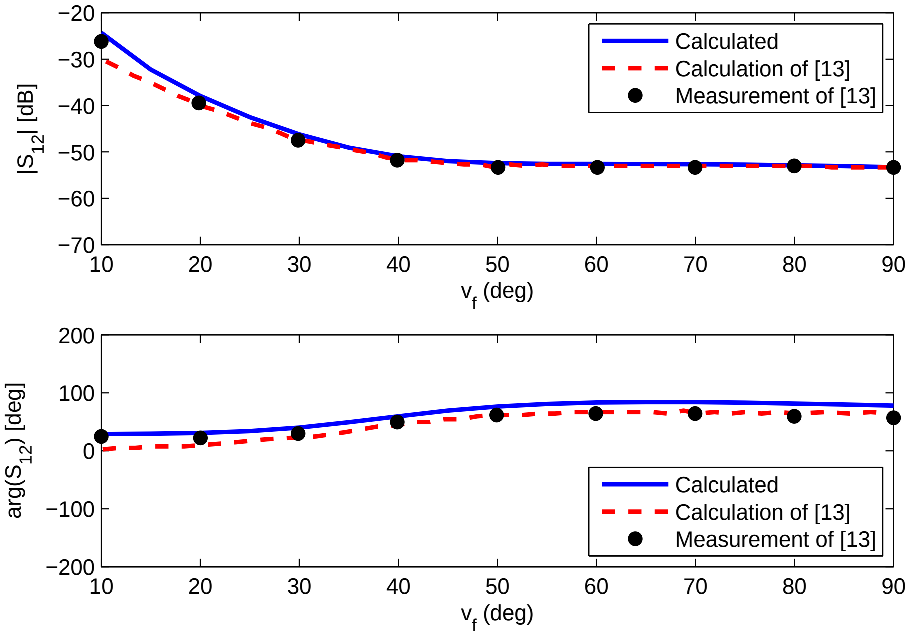

Figure 4.21: Comparison of the magnitude and phase of S_{21} ($[R, R]$ polarization) between two circular waveguide fed apertures as a function of u_f with the calculated results and calculation and measurement of [13] for the second configuration

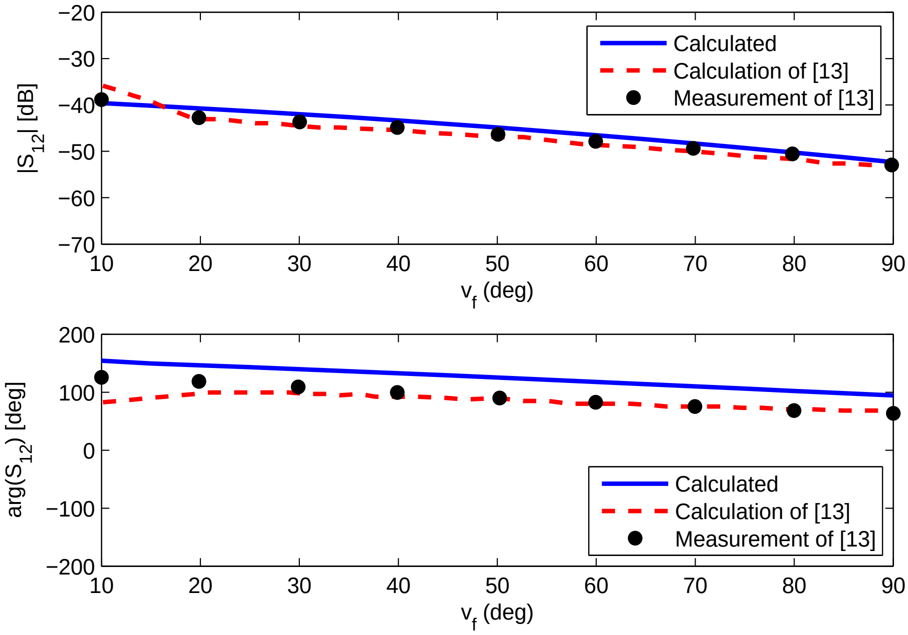

Figure 4.22: Comparison of the magnitude and phase of S_{21} ($[R, \phi]$ polarization) between two circular waveguide fed apertures as a function of u_f with the calculated results and calculation and measurement of [13] for the second configuration

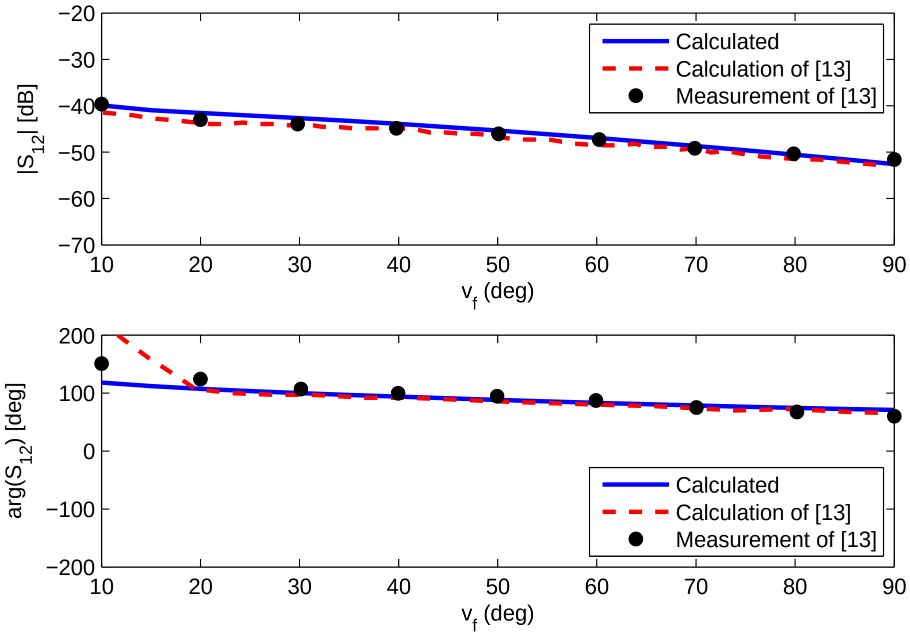

Figure 4.23: Comparison of the magnitude and phase of S_{21} ($[\phi, R]$ polarization) between two circular waveguide fed apertures as a function of u_f with the calculated results and calculation and measurement of [13] for the second configuration

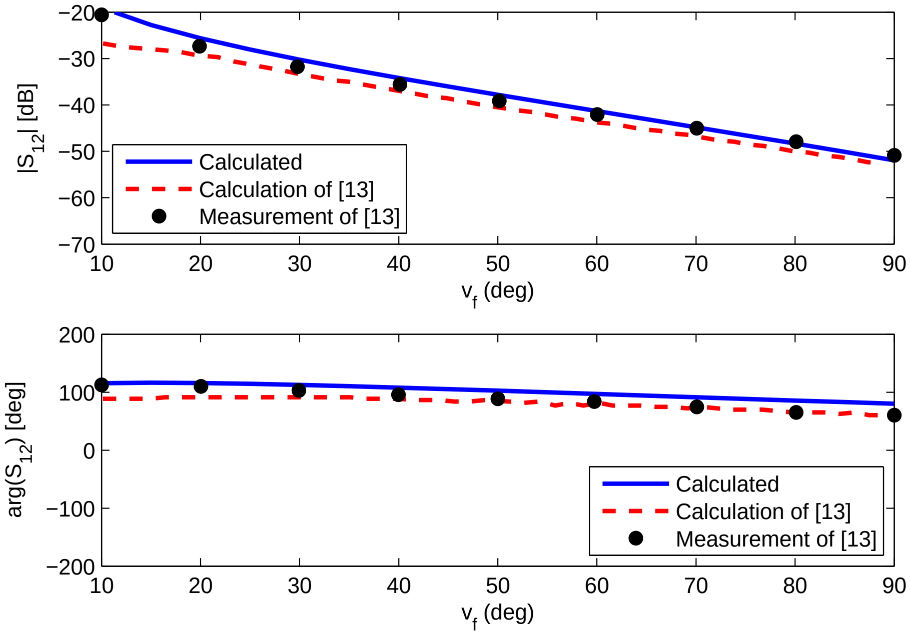

Figure 4.24: Comparison of the magnitude and phase of S_{21} ($[\phi, \phi]$ polarization) between two circular waveguide fed apertures as a function of u_f with the calculated results and calculation and measurement of [13] for the second configuration

are compared with the surface fields for PEC surfaces. Several numerical examples for the surface fields due to magnetic current sources for various geometries such as parabolic, hyperbolic cylinder and paraboloid of revolution with an IBC are presented.

The major difficulty in the evaluation of surface field formulation is the numerical evaluation of the Fock-type integrals. Since the accuracy and efficiency of the surface fields strongly depend on these integrals, special care is required for their numerical evaluation. Computation of the Fock type integrals are performed in two ways. The first approach is to invoke Cauchy's residue theorem. Briefly, the pole singularities of the integrands are found, and the values of the integrals are obtained by summing the residues corresponding to these poles. Details of this approach are explained in [19]. The second approach is to perform a numerical integration, and is based on deforming the integration contour on which the integrands of Fock type integrals are non-oscillatory and fast decaying. Briefly, these integrals are split into three integrals ranging from $(-\infty,0)$, $(0,\tau_{big})$ and (τ_{big},∞), where τ_{big} is chosen approximately $2m^3$ (or $3m^3$) to ensure all pole singularities including a low attenuation Elliott mode [31, 42, 43] are captured. Then, the integration variable τ is changed to $\tau e^{j2\pi/3}$ for the first integral and to $(\tau - \tau_{big})e^{j\pi/3}$ for the third integral, causing the Airy function and its derivative to be non-oscillatory and fast decaying (an exponential decay is achieved). Only the second integral remains oscillatory but its integration interval is relatively short. Thus, its numerical computation does not impose a difficulty though most of the CPU time is consumed during its computation. Finally, a simple Gaussian quadrature algorithm is used for the integration along this deformed contour. Since locating the poles requires a difficult and a complex procedure and one can easily miss a pole, and/or pole search algorithms may need to be modified for some geometries and physical parameters, second approach is preferred in this dissertation.

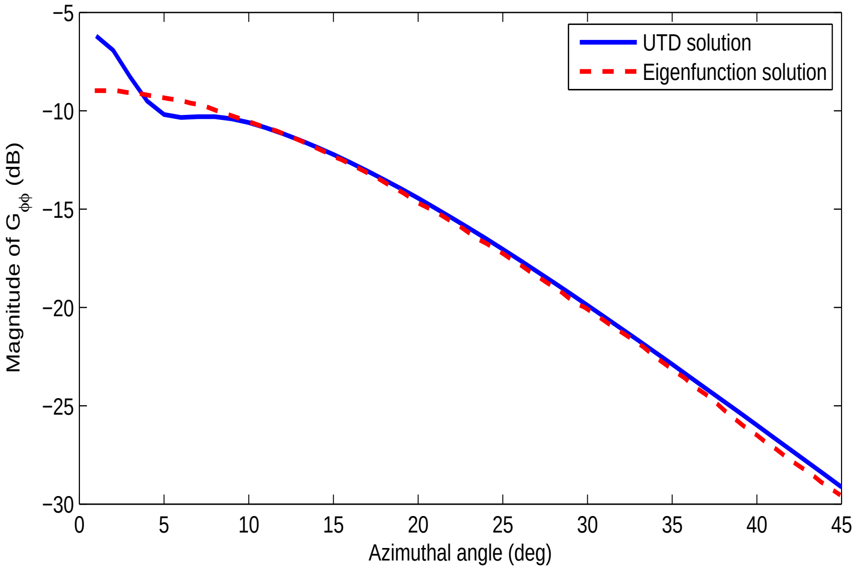

Figure 4.25: Comparison of the magnitude of $G_{\phi\phi}$ component of the eigenfunction solution and the UTD-based solution for the azimuthal angle, $(\phi_2 - \phi_1)$, varying from 0° to 45° at $f = 7GHz$ for a fixed vertical distance, $z_2 - z_1 = 3\lambda$, on a circular cylinder with $a = 5\lambda$ and $\Lambda = 0.1$

4.2.1 Cannonical surfaces

In this section, examples of tangential magnetic field components on an impedance cylinder and sphere are presented. Tangential magnetic field components are calculated using the expressions given in Chapter 2 and compared with the eigenfunction solutions given in Appendix B.

Circular cylinder geometry

The magnitude of $G_{\phi\phi}$ component of the eigenfunction solution and the UTD-based solution for the azimuthal angle, $(\phi_2 - \phi_1)$, varying from 0° to 45° at $f = 7GHz$ for a fixed vertical distance, $z_2 - z_1 = 3\lambda$, on a circular cylinder (see Fig. 2.1) with $a = 5\lambda$ and $\Lambda = 0.1$ are calculated and plotted in Fig. 4.25. As it is seen from the figure a good agreement is achieved except very small azimuthal angles which correspond to the paraxial region. In this region the UTD solution fails.

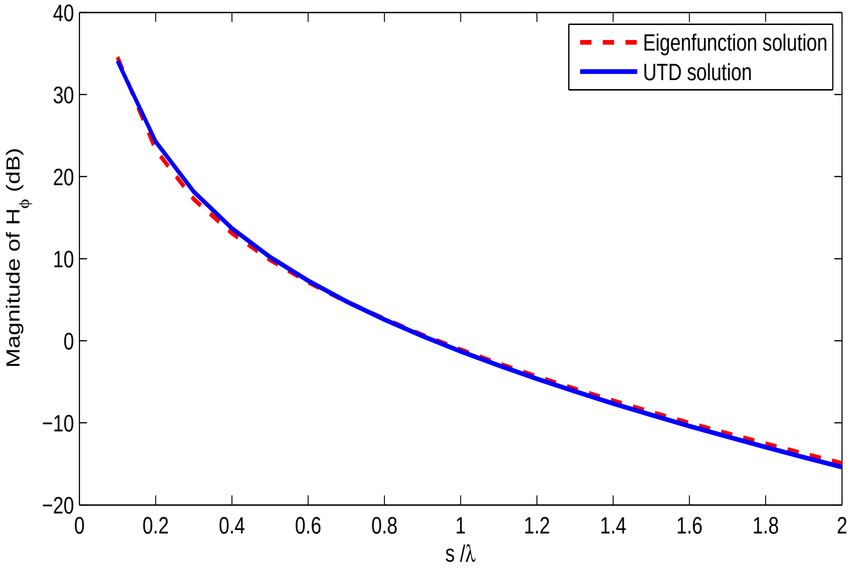

Figure 4.26: Comparison of the magnitude of H_ϕ component of the eigenfunction solution and the UTD-based solution for the geodesic path length, s, varying from 0.1λ to 2λ at $f = 10GHz$ for a fixed $\phi = 90°$ on a sphere with $a = 3\lambda$ and $\Lambda = 0.75$

Sphere geometry

The magnitude of H_ϕ component of the eigenfunction solution and the UTD-based solution for the geodesic path length, s, varying from 0.1λ to 2λ at $f = 10GHz$ for a fixed $\phi = 90°$ on a sphere (see Fig. 2.2) with $a = 3\lambda$ and $\Lambda = 0.75$ are calculated and plotted in Fig. 4.26. As it is seen from the figure a good agreement is achieved.

4.2.2 Arbitrary smooth convex surfaces

The arbitrary convex impedance surface solution is specialized to different geometries in this section. Firstly, the geometric parameters necesssary for the UTD solution are calculated. The details of the calculation of these parameters are given in Appendix E. By the help of these parameters pertaining to the geometry, tangential magnetic field expressions are calculated.

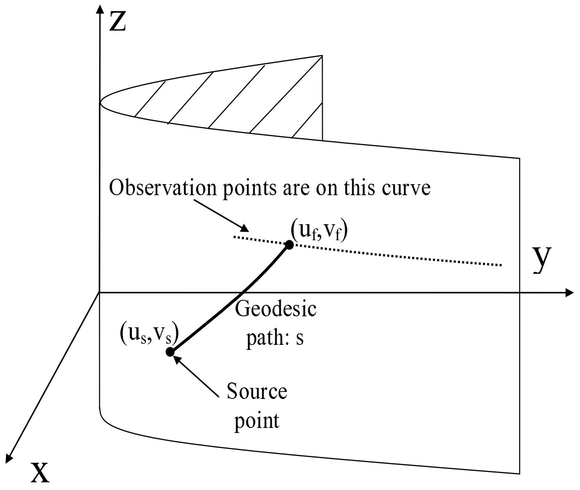

Figure 4.27: Problem geometry for impedance GPCYL

General parabolic cylinder geometry

Tangential magnetic field components with and without Δ terms [presented in (3.50)-(3.53)] are both computed using (3.49) for the geodesic path length varying from 1λ to 5λ for a GPCYL with $a = 5$ having a surface impedance of $Z_s = 1\Omega$. The source is located at $(u, v) = (2, 0)$, and the observation point is $(u, v) = (u_f, 0.5)$ where u_f changes along the geodesic path, as shown in Fig. 4.27. Comparison of the magnitude and phase of the calculated tangential magnetic field components of impedance GPCYL as a function of u_f with those of PEC GPCYL is in Figs. 4.28 and 4.29, respectively.

Elliptic cylinder geometry

Similar to the GPCYL case, tangential magnetic field components with and without Δ terms [presented in (3.50)-(3.53)] are both computed using (3.49) for the geodesic path length varying from 1λ to 5λ for an elliptic cylinder with $a = 5$ and $b = 2$ having a surface impedance of $Z_s = 1\Omega$. The source is located at $(u, v) = (0, 0)$, and the observation point is $(u, v) = (u_f, 0.5)$ where u_f changes along the geodesic path, as shown in Fig. 4.30. Comparison of the magnitude

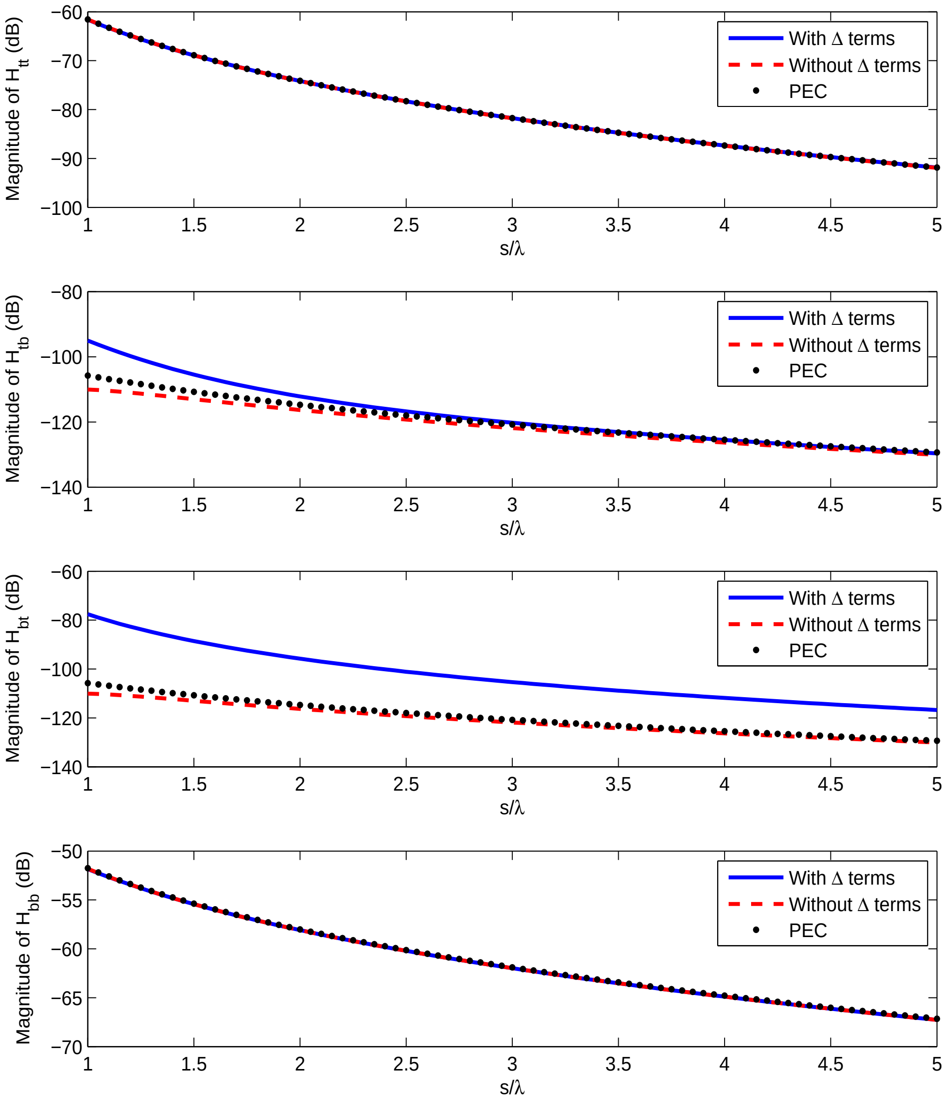

Figure 4.28: Comparison of the magnitudes of the calculated tangential magnetic field components with and without Δ terms for the geodesic path length varying from 1λ to 5λ for a GPCYL with $a = 5$ having a surface impedance of $Z_s = 1\Omega$ with those of PEC GPCYL

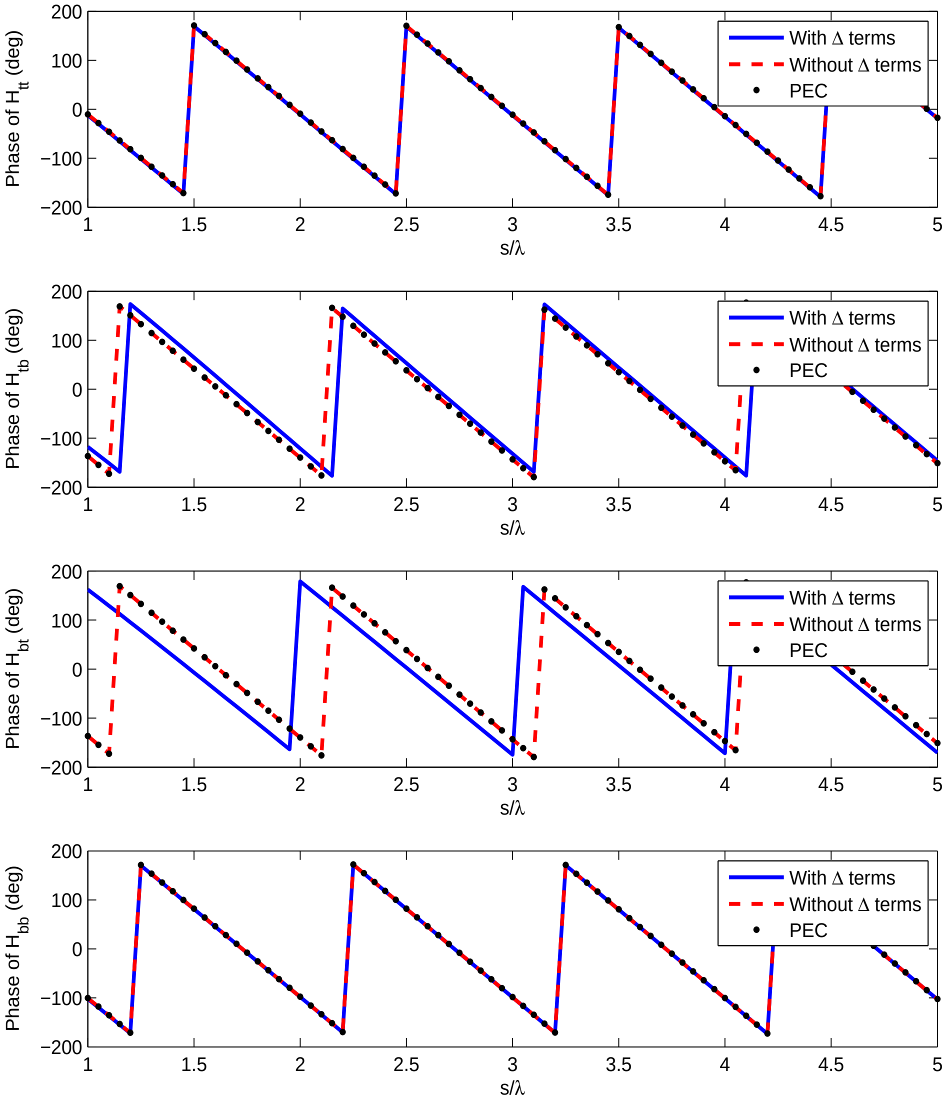

Figure 4.29: Comparison of the phases of the calculated tangential magnetic field components with and without Δ terms for the geodesic path length varying from 1λ to 5λ for a GPCYL with $a = 5$ having a surface impedance of $Z_s = 1\Omega$ with those of PEC GPCYL

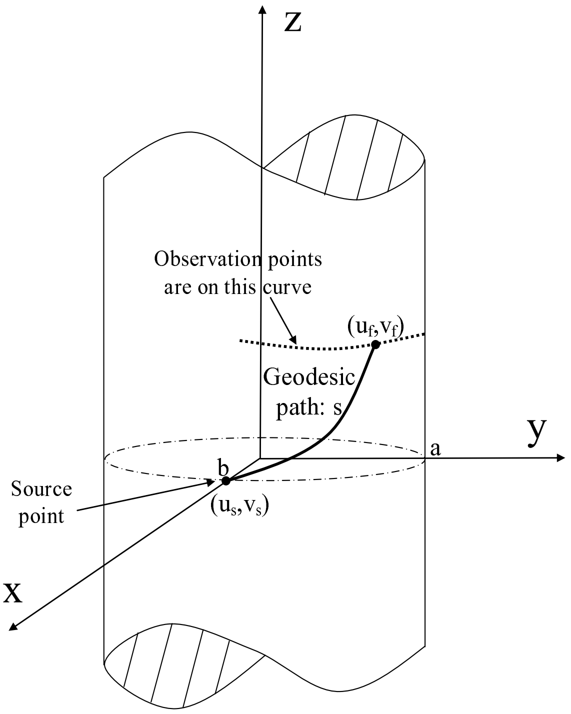

Figure 4.30: Problem geometry for impedance elliptic cylinder

and phase of the calculated tangential magnetic field components of impedance elliptic cylinder as a function of u_f with those of PEC elliptic cylinder is in Figs. 4.31 and 4.32, respectively.

General paraboloid of revolution geometry

Tangential magnetic field components with and without Δ terms [presented in (3.50)-(3.53)] are both computed using (3.49) for u_f varying from 0.5 to 4 for a GPOR with $a = 5$ having a surface impedance of $Z_s = 1\Omega$. The source is located at $(u, v) = (2, 0)$, and the observation point is $(u, v) = (u_f, \pi/4)$, as shown in Fig. 4.33. Comparison of the magnitude and phase of the calculated tangential magnetic field components of impedance GPOR as a function of u_f with those of PEC GPOR is in Figs. (4.34) and (4.35), respectively.

The following conclusions are drawn after the comparison of the magnitude

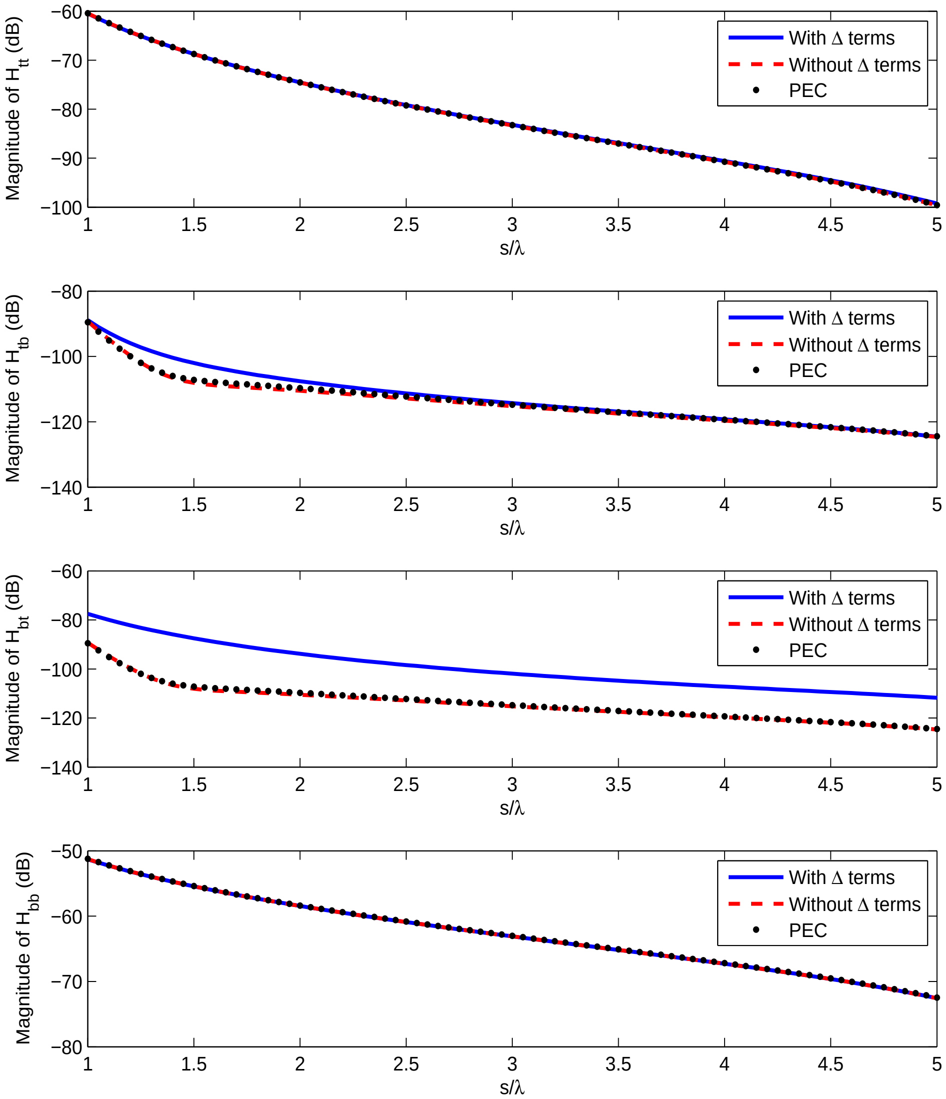

Figure 4.31: Comparison of the magnitudes of the calculated tangential magnetic field components with and without Δ terms for the geodesic path length varying from 1λ to 5λ for an elliptic cylinder with $a = 5$ and $b = 2$ having a surface impedance of $Z_s = 1\Omega$ with those of PEC elliptic cylinder

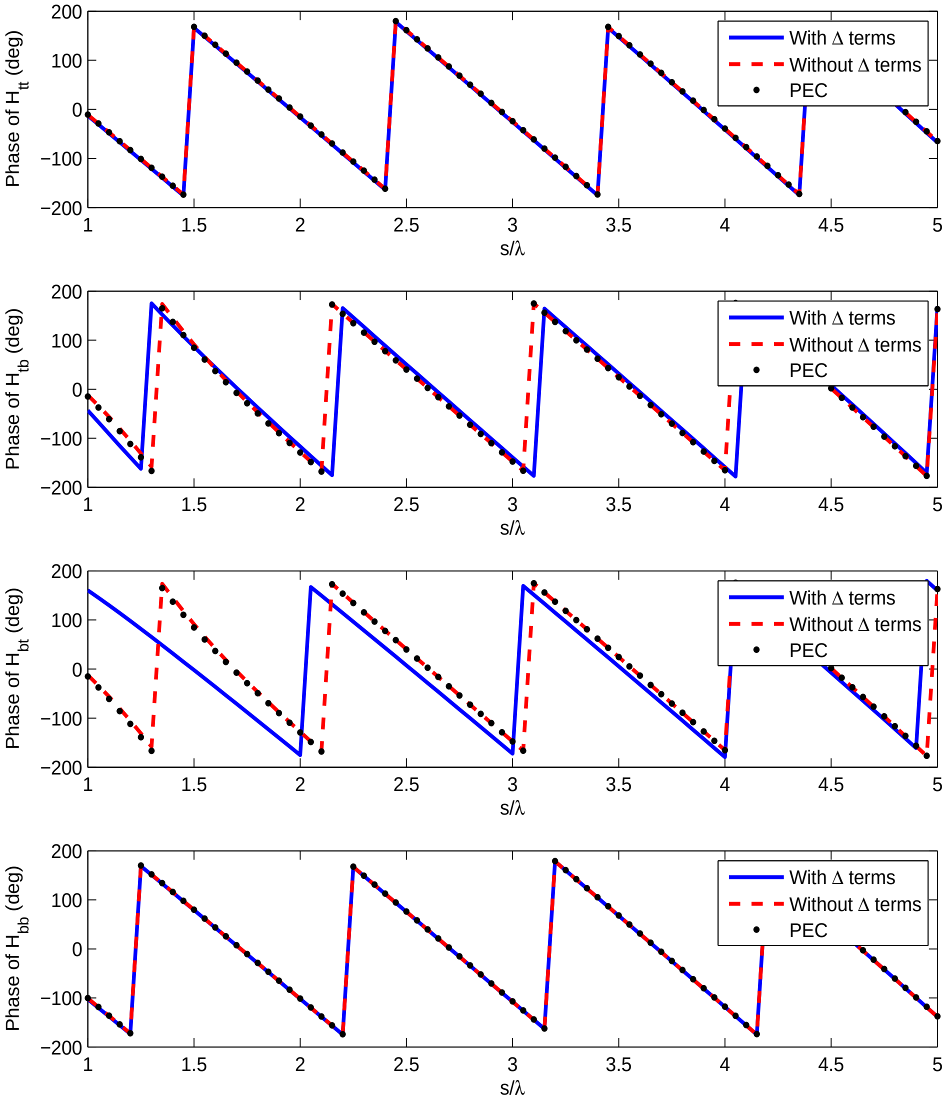

Figure 4.32: Comparison of the phases of the calculated tangential magnetic field components with and without Δ terms for the geodesic path length varying from 1λ to 5λ for an elliptic cylinder with $a = 5$ and $b = 2$ having a surface impedance of $Z_s = 1\Omega$ with those of PEC elliptic cylinder

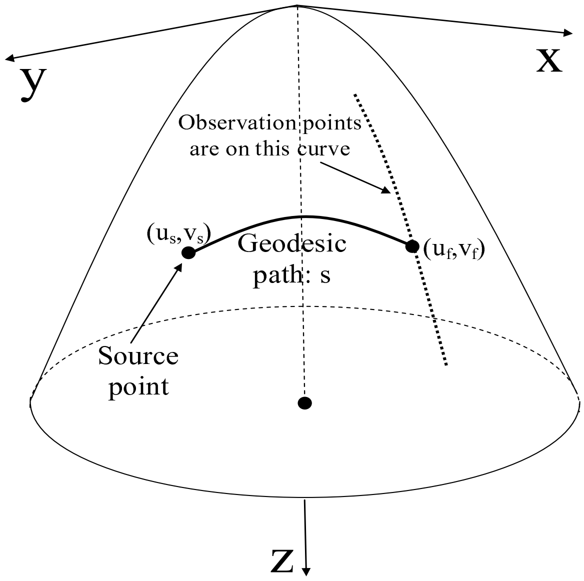

Figure 4.33: Problem geometry for impedance GPOR

and phase of the calculated tangential magnetic field components of impedance surfaces with those of PEC surfaces.

- In general, a good agreement is achieved without Δ terms.
- H_{bt} component with Δ terms is not accurate. H_{tb} component can be used instead of H_{bt} due to reciprocity.
- Δ terms improve the accuracy of the solution for about of $1dB$ at small separations between the source and the observation points as it seen from the H_{tt} and H_{bb} components of Figs. 4.28 and 4.31. However, Δ terms decrease the accuracy of the solution for about of $10dB$ as it seen from the H_{tb} components of Figs. 4.28 and 4.31.
- Δ terms give erroneous results when the angle between the geodesic path and the principal surface direction at the source/observation point goes to $\pi/2$. If Figs. 4.34 and 4.35 are examined, this occurs around $u_f = 1.6$, and $u_f = 2.4$. It can easily be seen from Fig. 4.36 that $u_f = 1.6$, and $u_f = 2.4$ correspond to the areas where angle between the geodesic path and the principal surface direction at the source/observation point goes to

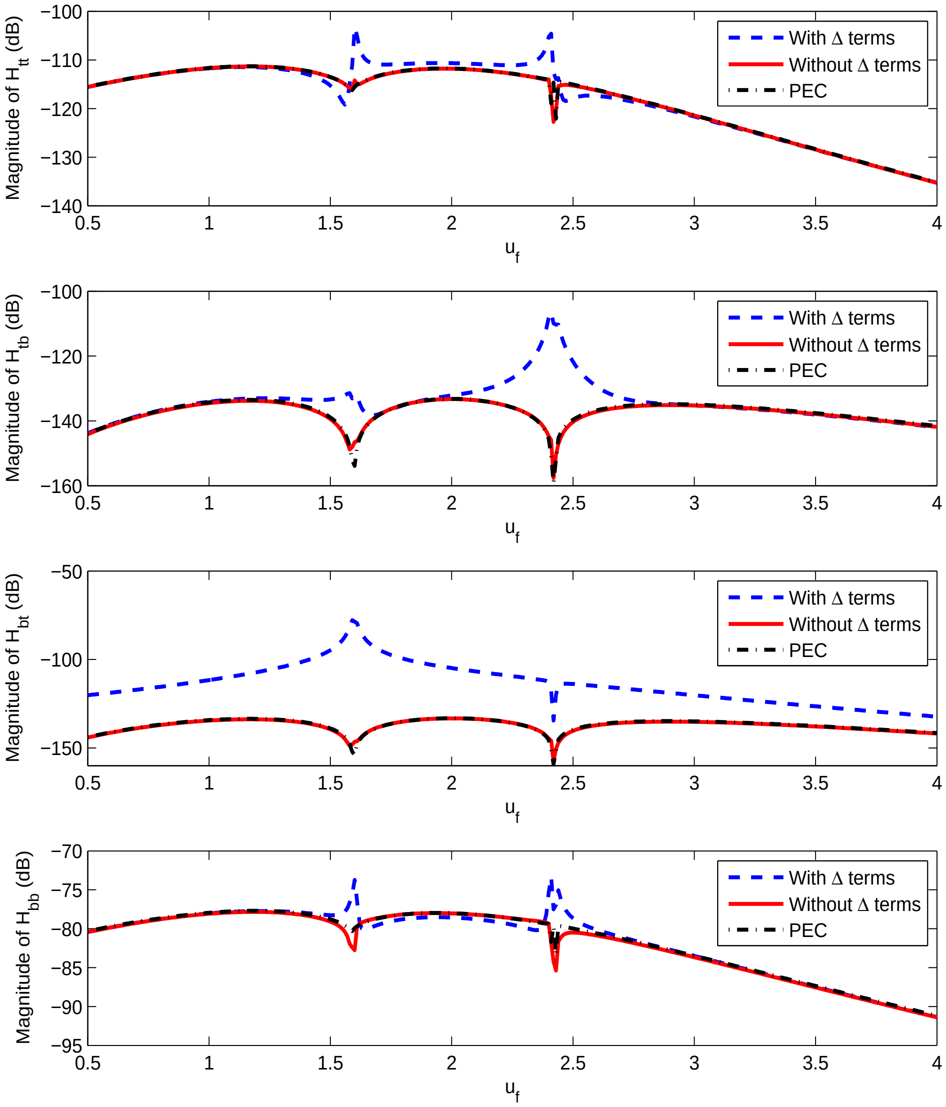

Figure 4.34: Comparison of the magnitudes of the calculated tangential magnetic field components with and without Δ terms for u_f varying from 0.5 to 4 for a GPOR with $a = 5$ having a surface impedance of $Z_s = 1\Omega$ with those of PEC GPOR

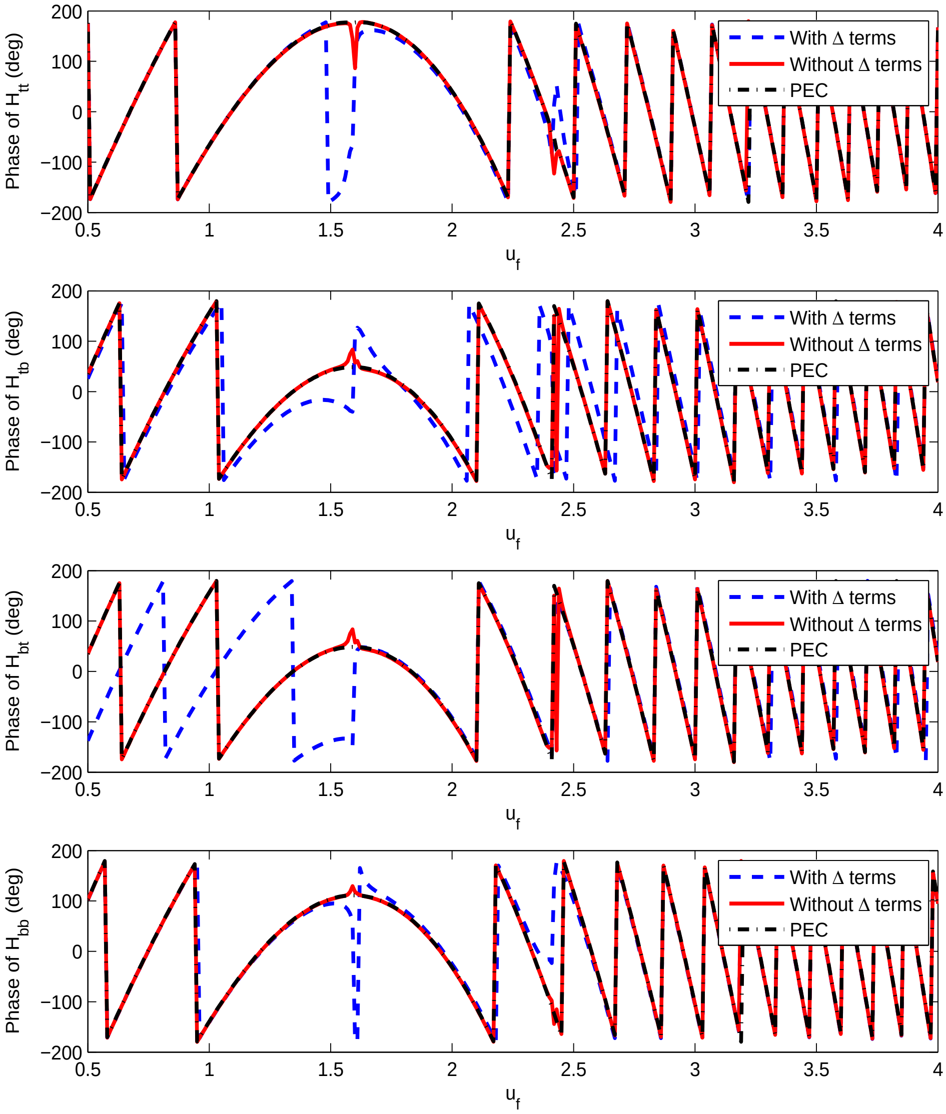

Figure 4.35: Comparison of the phases of the calculated tangential magnetic field components with and without Δ terms for u_f varying from 0.5 to 4 for a GPOR with $a = 5$ having a surface impedance of $Z_s = 1\Omega$ with those of PEC GPOR

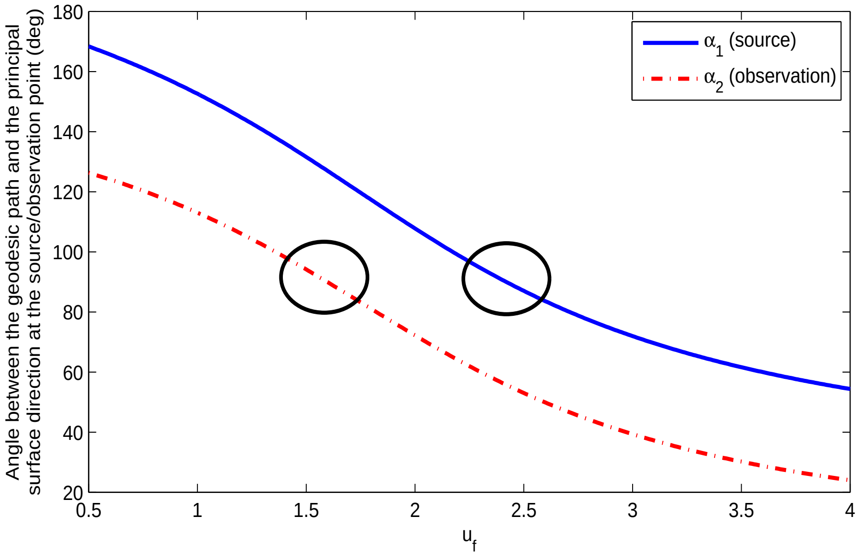

Figure 4.36: Angle between the geodesic path and the principal surface direction at the source/observation point

$\pi/2$.

- Special care is required if Δ terms are desired to be used. However, if the provided UTD solutions are used in a multipurpose code, it may be better not to include these terms.

The final set of numerical results illustrates how the tangential magnetic field components are affected by the change of the surface impedance. Therefore, tangential magnetic field components are computed using (3.49) without Δ terms [presented in (3.50)-(3.53)] for u_f varying from 0.5 to 4 on GPORs with $a = 5$ having different surface impedances. The source is located at $(u, v) = (2, 0)$, and the observation point is $(u, v) = (u_f, \pi/4)$ (see Fig. 4.33). Surface impedances are chosen to be in the form of $Z_s = \alpha$, $Z_s = \alpha + j\beta$ and $Z_s = \alpha - j\beta$ where $\alpha > 0$ and $\beta > 0$. Computed tangential magnetic field components are plotted in Figs. 4.37-4.39. Moreover, the results regarding the computed tangential magnetic field components with Δ terms for the same configuration are plotted in Figs. 4.40-4.42

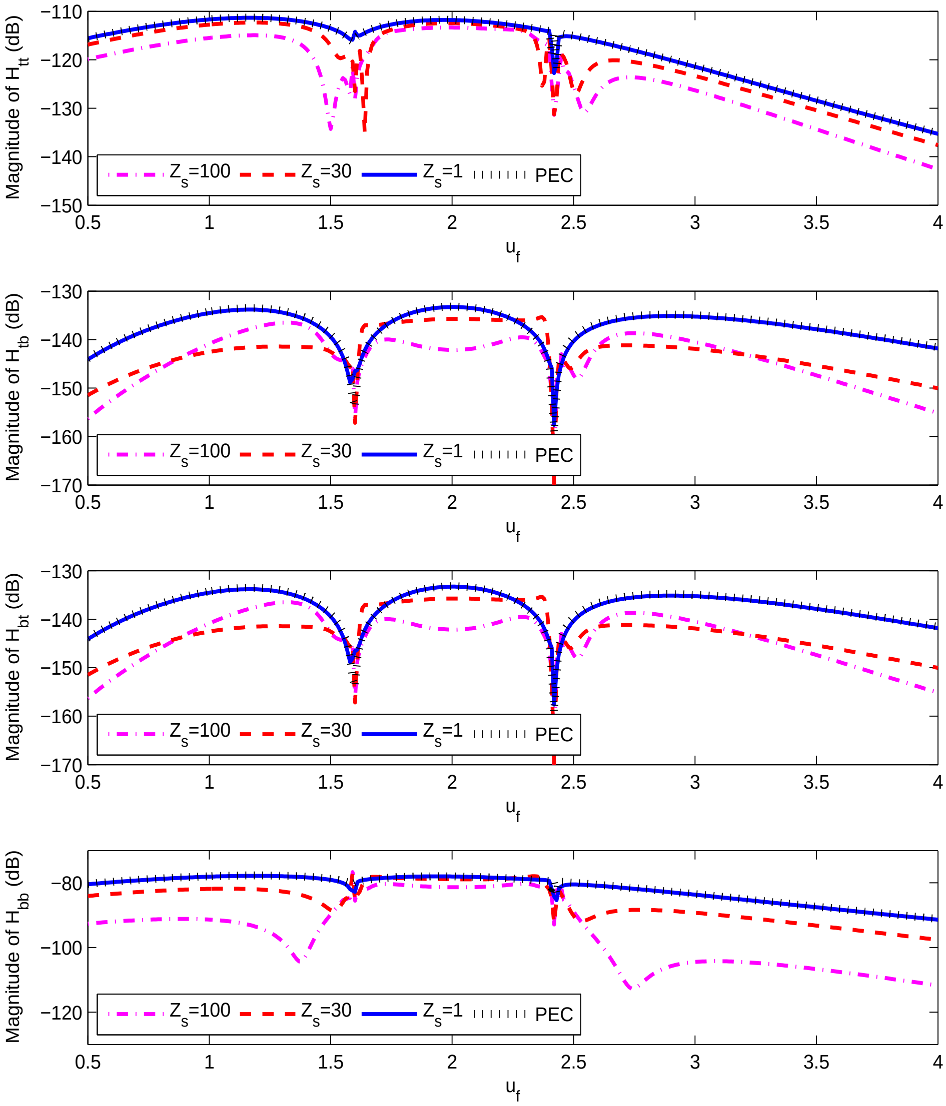

Figure 4.37: Magnitudes of the calculated tangential magnetic field components without Δ terms for u_f varying from 0.5 to 4 on GPORs with $a = 5$ having different surface impedances in the form of $Z_s = \alpha$. PEC result is given for reference.

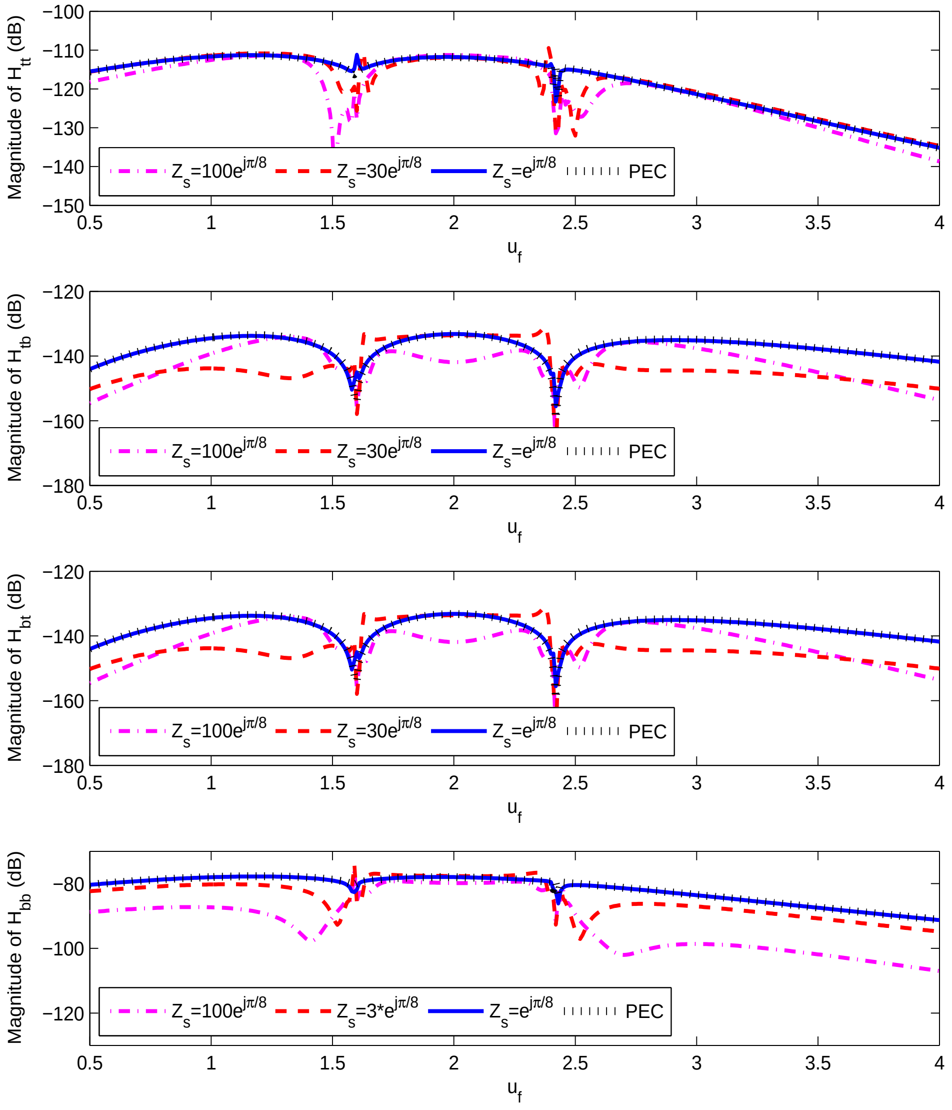

Figure 4.38: Magnitudes of the calculated tangential magnetic field components without Δ terms for u_f varying from 0.5 to 4 on GPORs with $a = 5$ having different surface impedances in the form of $Z_s = \alpha + j\beta$. PEC result is given for reference.

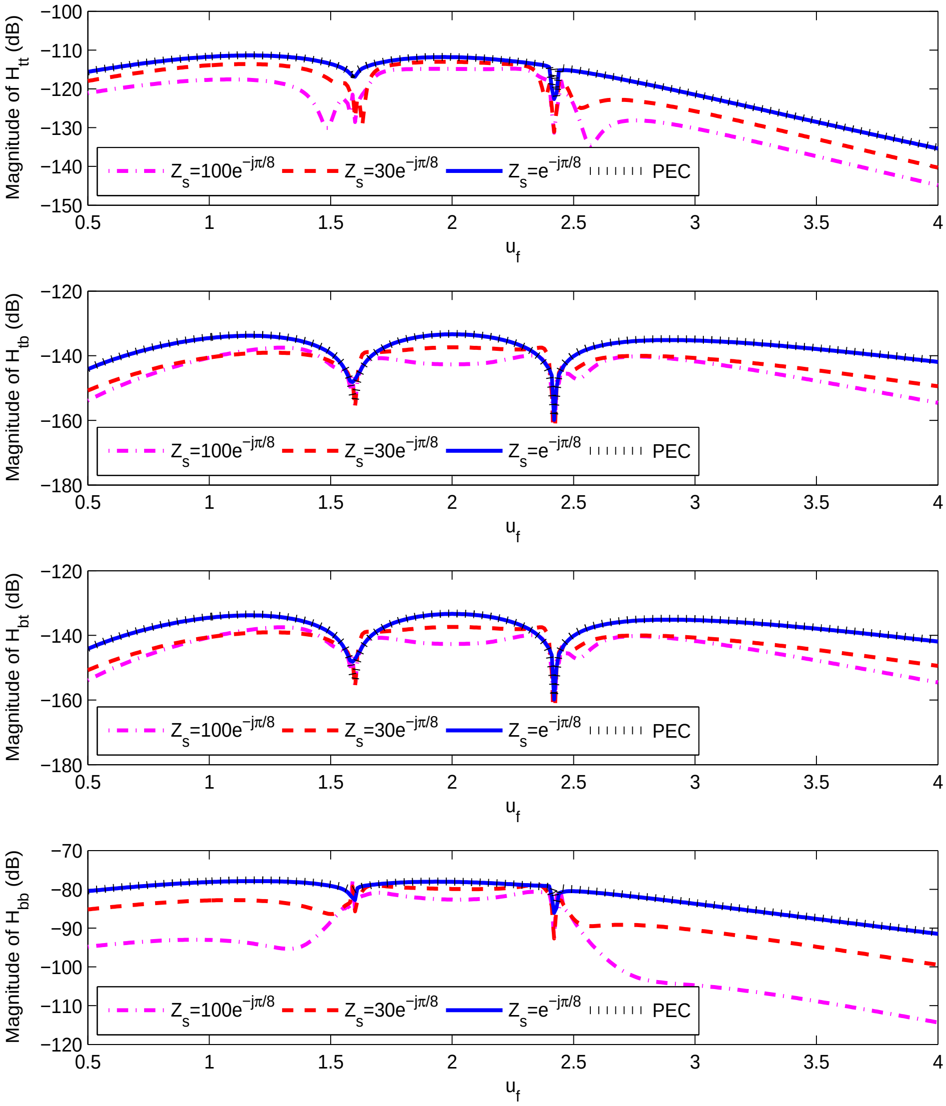

Figure 4.39: Magnitudes of the calculated tangential magnetic field components without Δ terms for u_f varying from 0.5 to 4 on GPORs with $a = 5$ having different surface impedances in the form of $Z_s = \alpha - j\beta$. PEC result is given for reference.

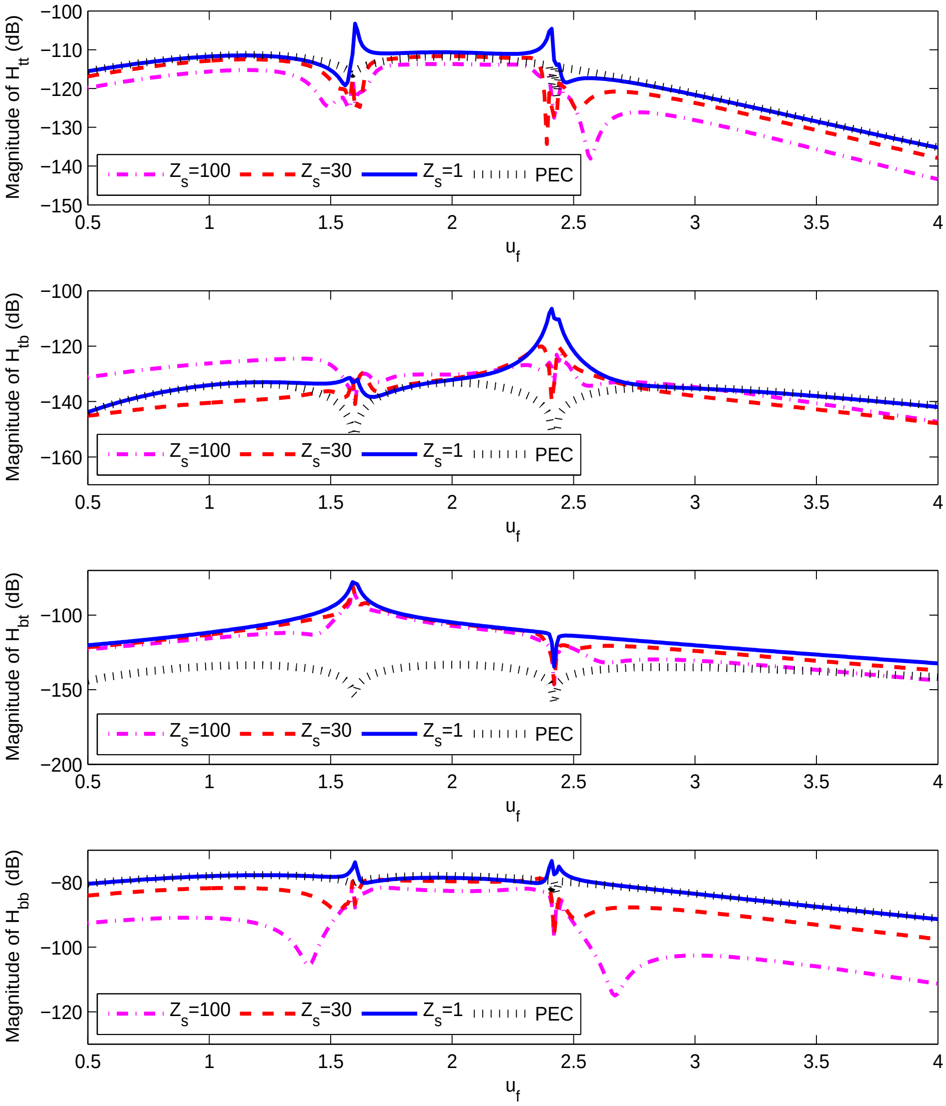

Figure 4.40: Magnitudes of the calculated tangential magnetic field components with Δ terms for u_f varying from 0.5 to 4 on GPORs with $a = 5$ having different surface impedances in the form of $Z_s = \alpha$. PEC result is given for reference.

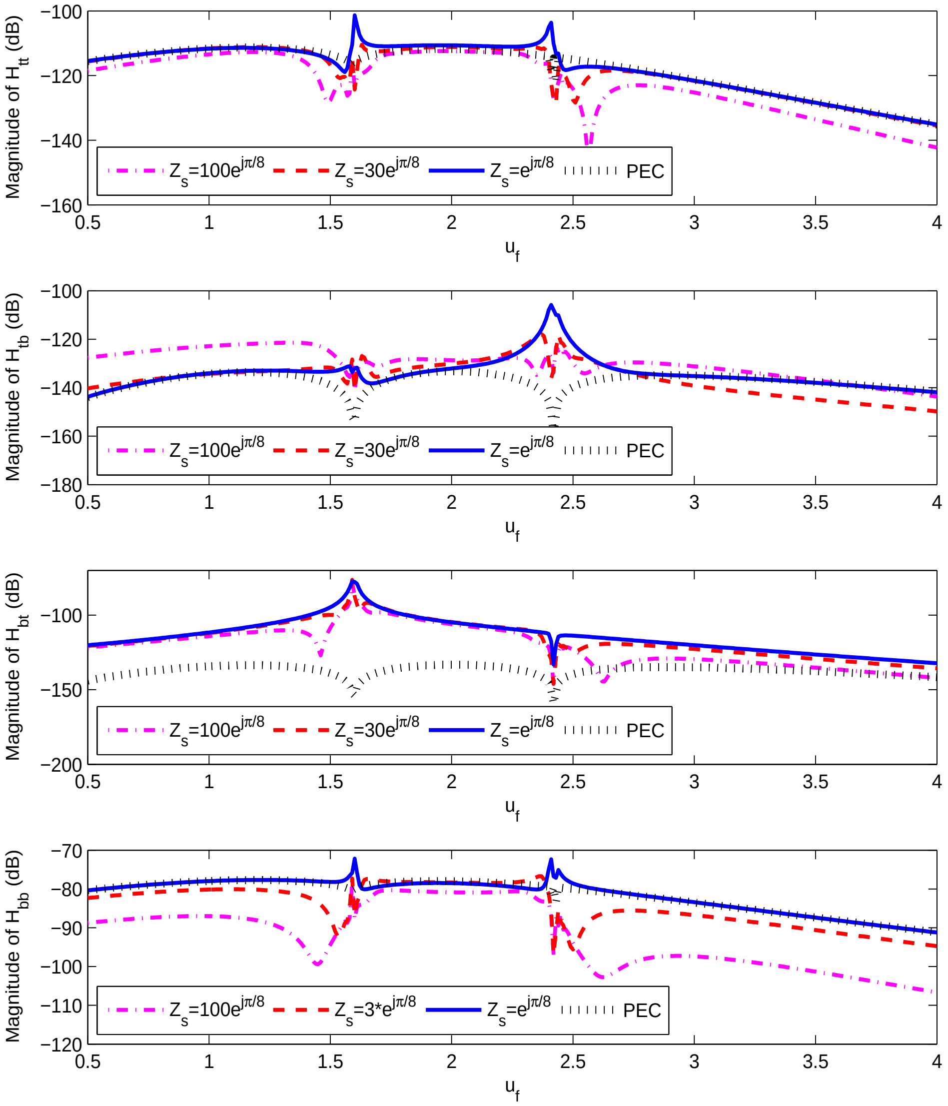

Figure 4.41: Magnitudes of the calculated tangential magnetic field components with Δ terms for u_f varying from 0.5 to 4 on GPORs with $a = 5$ having different surface impedances in the form of $Z_s = \alpha + j\beta$. PEC result is given for reference.

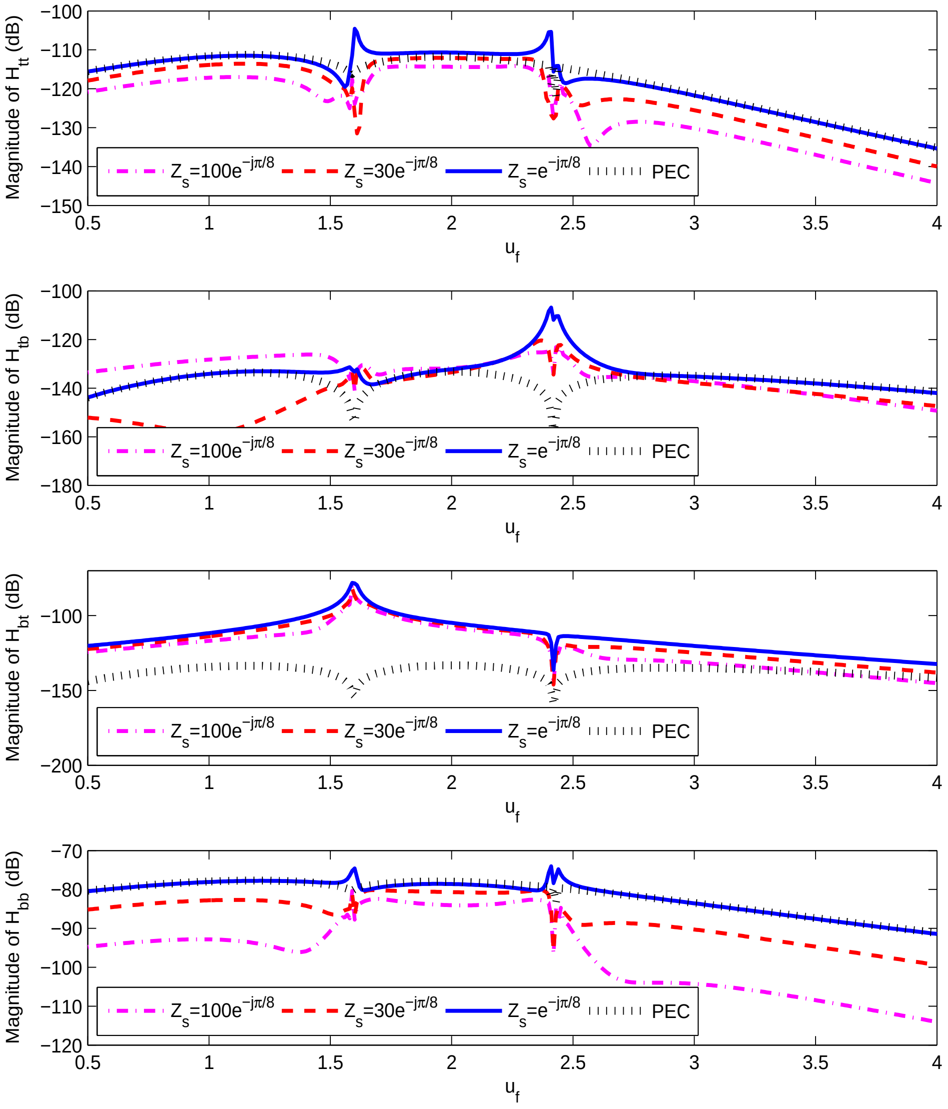

Figure 4.42: Magnitudes of the calculated tangential magnetic field components with Δ terms for u_f varying from 0.5 to 4 on GPORs with $a = 5$ having different surface impedances in the form of $Z_s = \alpha - j\beta$. PEC result is given for reference.

4.3 Results obtained by simulation tools

In this section, simulation tools such as HFSS, FEKO and CST are tried out to verify the validity and the accuracy of our proposed solution.

HFSS

Firstly, the mutual admittance results between two circumferential slots on PEC GPCYL are verified with HFSS. Mutual admidtance between two slots [Source: $(u, v) = (1.115, 0)$, Observation: $(u, v) = (u_f, 0)$] with slot length $= 0.5\lambda$ and width $= 0.2\lambda$ on a GPCYL, which has a shaping parameter $a = 0.5$, is computed using both UTD and HFSS. Comparison of the magnitude and phase of the mutual admittance as a function of increasing seperation between the two slots along the u axis is plotted in Fig. 4.43. As it is seen from the figure that a reasonable agreement is achieved.

Later, HFSS is tried out to obtain numerical results for impedance surfaces. Several simulations are made with different configurations of two circumferential slots on impedance GPCYLs having different surface impedance and generated mutual coupling results. As an example, magnitude of mutual admittance between two slots [Source: $(u, v) = (1, 0)$, Observation: $(u, v) = (1.2751, 0)$] with slot length $= 0.65\lambda$ and width $= 0.27\lambda$ on a GPCYL, which has a shaping parameter $a = 1.5$, computed using both UTD and HFSS is given in Table 4.1. As it is seen from Table 4.1, the results do not agree with each other. Mutual admittance decreases as the surface impedance increases. Also, the decrement is very sharp beyond 100Ω.

Beside the impedance boundary, simulations are made for a thin material coated PEC surface to understand whether the impedance boundary definition of HFSS is the same with our definition. The simulations are done on planar surfaces for simplicity. Magnetic field for a rectangular slot located on an impedance planar surface ($Z_s = 130\Omega - j100\Omega$) and thin material coated PEC surface having the same surface impedance is compared (At $f = 10GHz$, a PEC surface coated

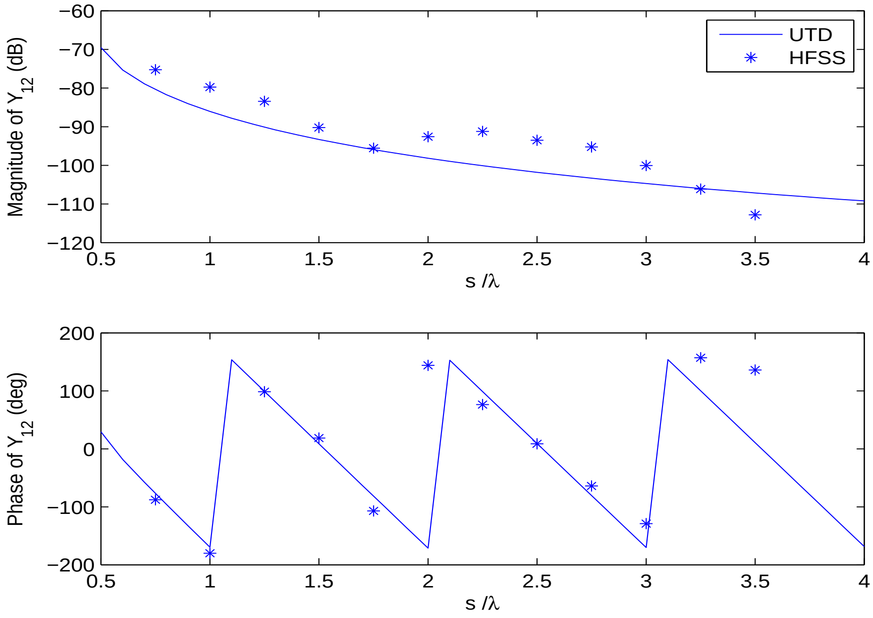

Figure 4.43: Comparison of the magnitude and phase of the mutual admittance between two slots [Source: $(u, v) = (1.115, 0)$, Observation: $(u, v) = (u_f, 0)$] with slot length $= 0.5\lambda$ and width $= 0.2\lambda$ on a GPCYL, which has a shaping parameter $a = 0.5$, computed using both UTD and HFSS as a function of increasing seperation between the two slots along the u axis

Surface impedance (Ω)	UTD	HFSS
0 (PEC)	-76.69	-77.43
20	-77.07	-74.18
100	-79.06	-73.39
1000	-94.06	-74.51

Table 4.1: Magnitude (dB) of mutual admittance between two slots [Source: $(u, v) = (1, 0)$, Observation: $(u, v) = (1.2751, 0)$] with slot length $= 0.65\lambda$ and width $= 0.27\lambda$ on a GPCYL, which has a shaping parameter $a = 1.5$, computed using both UTD and HFSS

with a $2.286mm$ thick material with $\epsilon_r = 11.8$ and $\mu_r = 1.4 + j1.4$ has a surface impedance of $130\Omega - j100\Omega$ [1]). The impedance boundary results and thin material coated PEC surface results are close each other. However, magnitude of magnetic field on these surfaces is greater when compared with the PEC surface result. This unreasonable situation indicates that HFSS do not give accurate results for the impedance boundary condition.

FEKO

FEKO is another simulation tool preferred to use. Since it has magnetic point source definition, surface magentic field comparison can be made instead of mutual admittance comparison. Fistly, the tangential magnetic fields due to a magnetic point source on PEC parabolic cylinders are calculated using FEKO. A good agreement for PEC parabolic cylinder is achieved. However, FEKO results for impedance parabolic cylinder were quite different from the results obtained by our proposed UTD solution. Several tests are made by changing the surface impedance of the geometry. The summary of the tests and the results are as follows:

- For a $z-$directed magnetic point source located on the vertex of the impedance parabolic cylinder, $z-$component of the surface magnetic field is calculated.
- Z_s is chosen 1Ω. The UTD result is very close to the PEC result as expected. Magnitude of the FEKO result is $8-10dB$ higher than the PEC result. The phase obtained from FEKO is not close to the phase of the PEC result.
- As Z_s is increased, magnitudes of both the UTD result and the FEKO result decrease as expected. However, the magnitude of the FEKO result is still higher than the PEC result.
- As Z_s is further increased ($Z_s > 1000\Omega$), FEKO result converges to PEC result, which does not make sense.

Configuration	Mutual admittance (dB)
0 (PEC)	-84.02
Thin material coated PEC	-84.19
$Z_s = 380\Omega - j50\Omega$	-85.66
$Z_s = 1000\Omega$	-90.91

Table 4.2: Comparison of magnitude (dB) of mutual admittance between two slots (slot length = 0.65λ and width = 0.27λ) separated by 1λ on different planar surfaces computed by CST

These findings show that FEKO does not give accurate results for the impedance boundary condition.

CST

CST is the final simulation tool that is used. The magnitude of the mutual admittance between two slots (slot length = 0.65λ and width = 0.27λ) separated by 1λ on an impedance planar surface ($Z_s = 380\Omega - j50\Omega$) and a thin material coated PEC surface having the same surface impedance are compared and tabulated in Table 4.2 (At $f = 5GHz$, a PEC surface coated with a $2.286mm$ thick material with $\epsilon_r = 12$ and $\mu_r = 2.2 + j1.4$ has a surface impedance of $380\Omega - j50\Omega$ [1]). PEC result is given for reference. As seen from Table 4.2, the impedance boundary results and the thin material coated PEC surface results are close to each other. Mutual admittance decreases as the surface impedance increases as expected. However, the decrement is not as fast as expected.

Chapter 5

Conclusions

In this dissertation, a UTD-based high frequency asymptotic formulation for the appropriate Green's function representation pertaining to the surface fields excited by a magnetic current source located on an arbitrary smooth convex surface with a thin material coating (approximated by IBC) is developed for the first time. This formulation can be used in the efficient evaluation of the mutual coupling for conformal slot/aperture antennas on thin material coated/partially coated PEC surfaces. Also, it is useful for the design/analysis of conformal antennas/arrays which can be mounted on aircrafts, missiles, mobile base stations, etc.

Surface field solutions of cannocial geometries, which are circular cylinder and sphere, are used in obtaining the arbitrary smooth convex surface solution. The solution is constructed by blending the cylinder and sphere solutions using blending functions, which are introduced heuristically via the locality of high frequency wave propagation after the generalization of the important parameters included in the surface field expressions such as the divergence factor, the Fock parameter and Fock type integrals.

In obtaining the final UTD-based Green's function representation for impedance surfaces, some approximations are made. Impedance cylinder and sphere solutions contain the derivatives of Fock type integrals different from those of PEC solutions. Because working with these terms is intractable in the generalization process, derivative terms are not included in the cylinder and sphere expressions used for the generalization for convenience. Although the derivation of surface fields for arbitrary convex impedance surface appears to be a simple extension of that of PEC case, it has substantial differences and difficulties. Fock type integrals pertaining to the cylinder and sphere geometries become more complex when the impedance boundary condition exists. The proposed technique in the literature is based on invoking the Cauchy's residue theorem by finding the pole singularities numerically. Since locating the poles requires a difficult and a complex procedure and one can easily miss a pole, and/or pole search algorithms may need to be modified for some geometries and physical parameters, an alternative technique, which is based on deforming the integration contour on which the integrands of Fock type integrals are non oscillatory and fast decaying, is developed and used in obtaining the numerical results in this dissertation.

Numerical results are given for both singly and doubly curved surfaces. Obtained results are compared with those of PEC surfaces in the limiting case where the surface impedance, $Z_s \rightarrow 0$ because of the lack of numerical results for the surface fields for impedance surfaces in the literature and the failure of the popular CAD tools, such as HFSS, CST and FEKO in obtaining accurate results for surfaces with an IBC.

The final UTD-based Green's function representation for impedance surfaces looks very similar to those of PEC surfaces except the Fock type integrals and Δ terms. Although Δ terms improve the accuracy of the solution at small separations for some tangential magnetic field components, the accuracy of the solution decreases too much for the other components. Also, Δ terms deteriorate the surface field results for particular circumstances, such as when the angle between the geodesic path and the principal surface direction at the source/observation point is around $\pi/2$. Because of this problematic nature of these terms, it is more appealing not to use them in a multipurpose code.

In conclusion, the prominent attributes of this solution can be summarized as follows:

- Although it is an approximate solution, it is an accurate solution for the mutual coupling problem.

- It includes more general Fock type integrals. These integrals are valid for all arbitrary smooth convex surfaces. Also, they recover the cylinder and sphere Fock type integrals when the solution is specialized to these geometries.

- An alternative computation approach to the one in the literaure is introduced for the evaluation of the Fock type integrals, which is the major burden in the evaluation of the UTD solution. It has several advantages such as having an easier formulation and less computational time.

- For electrically large geometries, this solution give results in terms of seconds in a standard personal computer whereas computation of surface fields lasts tens of hours with popular simulation tools on professional workstations. Morever, simulation tools do not give accurate results for impedance boundary.

Appendix A

Uniform Geometrical Theory of Diffraction (UTD)

A brief information about UTD is given in Appendix.

Geometrical optics (GO) explains electromagnetic propagation in terms of rays. GO ray field locally behaves like a plane wave in a lossless, homogeneous medium. GO is comprised of incident, reflected and transmitted ray. Since the geometries of interest are impenetrable, transmitted ray fields do not exist in our case. Let us consider a line source excitation near a PEC half plane as shown in Fig. A.1. The GO solution for this problem is as follows:

$$U^t = \begin{cases} U^i + U^r, & \text{in Region I} \\ U^i, & \text{in Region II} \\ 0, & \text{in Region III} \end{cases} \tag{A.1}$$

where U^t, U^i and U^r are total, incident and reflected ray fields, respectively. The GO solution has certain failures. The first one is discontinuity of the field across the shadow boundaries. Another failure is the incorrect prediction of the field in Region III, which is, in fact, nonzero .

Keller examined the exact solution of the plane wave illuminated to PEC half plane (the line source in Fig. A.1 is moved to infinity) and figured out that there must be an additional component, which corresponds to diffracted rays.

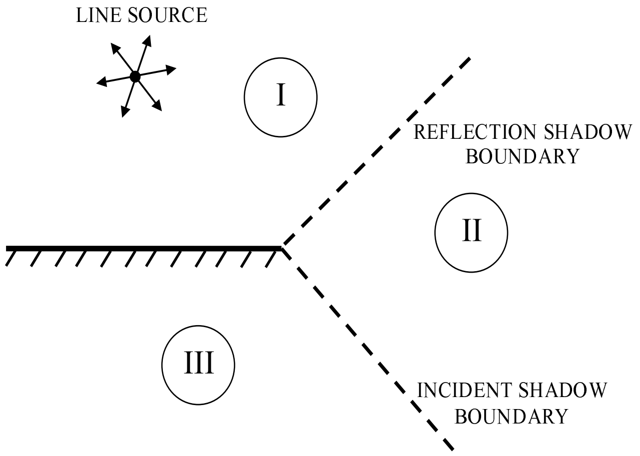

Figure A.1: Line source excitation near a PEC half plane

These diffracted rays emanate from the discontinuties (edge, corner, vertex) and smooth convex parts of the object by the illumination of GO rays to these points. Keller's solution, which is entitled Geometrical Theory of Diffraction (GTD [44]), includes diffracted rays in addition to the incident and reflected rays of the GO solution. GTD solution was a very simple approach to deal with the complex high frequency problems. However, GTD solution is singular around shadow boundaries. This weakness limited the usage of GTD by researchers.

Later, Uniform Geometrical Theory of Diffraction (UTD) is proposed to overcome the deficiencies of GTD in [4]. In UTD solution, transition functions, which go to zero at shadow boundaries where the diffraction coefficients become singular, are introduced. Multiplication of the transtion function with the diffraction coefficients assures that diffractied ray solution remains bounded and total high frequency solution is continuous across the shadow boundaries. Transition functions are obtained from cannonical problems. They are comprised of Fresnel integrals for edge diffraction and Fock type integrals for diffraction from smooth convex surfaces.

Appendix B

Eigenfunction solution pertaining to the canonical problems

B.1 Impedance Circular Cylinder

Eigenfunction solution pertaining to the impedance circular cylinder is given in [19]. A brief summary of this derivation is given in this Appendix for the sake of completeness.

The electric and magnetic fields, $\vec{E}$ and $\vec{H}$, due to a point magnetic current satisfy the following vector wave equations:

$$(\vec{\nabla}^2 + k^2) \begin{bmatrix} \vec{E}(\vec{r}) \\ \vec{H}(\vec{r}) \end{bmatrix} = \frac{j}{Z_0 k} \begin{bmatrix} -jkZ_0\vec{\nabla}\times \\ k^2 + \vec{\nabla}\vec{\nabla}\cdot \end{bmatrix} \vec{M}(\vec{r}). \tag{B.1}$$

In (B.1) k is the free space wave number, Z_0 is the intrinsic impedance of free space, $\vec{r}'$ and $\vec{r}$ are the position vectors for the source and observation points, respectively, and the tangential electric current, $\vec{M}$, on the surface of the cylinder is given by

$$\vec{M}(\vec{r}) = (P_m^z \hat{z} + P_m^\phi \hat{\phi})\delta(\vec{r} - \vec{r}'). \tag{B.2}$$

The $\hat{z}$ components of the electric and magnetic fields correspond to the following equations:

$$(\vec{\nabla}^2 + k^2)\begin{bmatrix} E_z \\ H_z \end{bmatrix} = \frac{j}{Z_0 k}\hat{z} \cdot \begin{bmatrix} -jkZ_0\vec{\nabla}\times \\ k^2 + \vec{\nabla}\vec{\nabla}\cdot \end{bmatrix} \vec{M}(\vec{r}). \tag{B.3}$$

In an unbounded medium, E_z and H_z can be expressed as follows:

$$\begin{bmatrix} E_z \\ H_z \end{bmatrix} = -\frac{j}{Z_0 k}\hat{z} \cdot \begin{bmatrix} -jkZ_0\vec{\nabla}\times \\ k^2 + \vec{\nabla}\vec{\nabla}\cdot \end{bmatrix} (P_m^z \hat{z} + P_m^\phi \hat{\phi}) \frac{e^{-jk|\vec{r}-\vec{r}'|}}{4\pi|\vec{r}-\vec{r}'|}. \tag{B.4}$$

The equations given by (B.4) can be modified to express electric and magnetic fields in terms of source point coordinates such that

$$\begin{bmatrix} E_z \\ H_z \end{bmatrix} = -\frac{j}{Z_0 k}\hat{z} \cdot \begin{bmatrix} jkZ_0\vec{\nabla}'\times \\ k^2 + \vec{\nabla}'\vec{\nabla}'\cdot \end{bmatrix} (P_m^z \hat{z} + P_m^\phi \hat{\phi}) \frac{e^{-jk|\vec{r}-\vec{r}'|}}{4\pi|\vec{r}-\vec{r}'|}. \tag{B.5}$$

We expand the spherical wave as a spectral integral of a product of a cylindrical and plane waves using the Sommerfeld identity given by

$$\frac{e^{-jk|\vec{r}-\vec{r}'|}}{|\vec{r}-\vec{r}'|} = -\frac{j}{2}\int_{-\infty}^{\infty} dk_z e^{-jk_z z_d} H_0^{(2)}(k_\rho|\vec{\rho}-\vec{\rho}'|). \tag{B.6}$$

Using the Addition theorem, the Hankel function, $H_0^{(2)}(k_\rho|\vec{\rho}-\vec{\rho}'|)$, can be expanded as an infinite summation of standing and outgoing waves as

$$H_0^{(2)}(k_\rho|\vec{\rho}-\vec{\rho}'|) = \sum_{n=-\infty}^{\infty} e^{jn\phi_d} J_n(k_\rho \rho_<) H_n^{(2)}(k_\rho \rho_>). \tag{B.7}$$

In (B.6) and (B.7), $z_d = z - z'$, $\phi_d = \phi - \phi'$, k_z and k_ρ are the axial and radial wave numbers, respectively such that

$$k_\rho = \begin{cases} \sqrt{k^2 - k_z^2} & \text{if } k^2 \geq k_z^2 \\ -j\sqrt{k_z^2 - k^2} & \text{if } k^2 < k_z^2. \end{cases} \tag{B.8}$$

Now, $\hat{z}$ components of the electric and magnetic fields can be expressed as

$$\begin{aligned} \begin{bmatrix} E_z \\ H_z \end{bmatrix} &= -\frac{1}{8\pi Z_0 k}\hat{z} \cdot \begin{bmatrix} jkZ_0\vec{\nabla}'\times \\ k^2 + \vec{\nabla}'\vec{\nabla}'\cdot \end{bmatrix} (P_m^z \hat{z} + P_m^\phi \hat{\phi}) \int_{-\infty}^{\infty} dk_z e^{-jk_z z_d} \\ & \sum_{n=-\infty}^{\infty} e^{jn\phi_d} J_n(k_\rho \rho_<) H_n^{(2)}(k_\rho \rho_>). \end{aligned} \tag{B.9}$$

The orders of the derivatives and the integral can be interchanged to yield

$$\begin{bmatrix} E_z \\ H_z \end{bmatrix} = \frac{1}{2\pi}\int_{-\infty}^{\infty} dk_z e^{-jk_z z_d} \sum_{n=-\infty}^{\infty} e^{jn\phi_d} J_n(k_\rho \rho_<) H_n^{(2)}(k_\rho \rho_>) \overleftarrow{S} \tag{B.10}$$

where the operator $\overleftarrow{S}$, which acts on functions to its left and is defined for the $e^{-jk_z z' - jn\phi'}$ dependence [45], is given by

$$\overleftarrow{S} = -\frac{1}{4k\rho'} \begin{bmatrix} jk\rho' P_m^{\phi} \partial/\partial\rho' \\ Z_0^{-1}(k_\rho^2 \rho' P_m^z + nk_z P_m^{\phi}) \end{bmatrix}. \tag{B.11}$$

If we introduce a circular cylinder into the unbounded medium, such that $\rho' > a$ and $\rho > a$, by taking the reflections from the cylinder into account the field components can be written as

$$\begin{bmatrix} E_z \\ H_z \end{bmatrix} = \frac{1}{2\pi}\int_{-\infty}^{\infty} dk_z e^{-jk_z z_d} \sum_{n=-\infty}^{\infty} e^{jn\phi_d} \begin{bmatrix} \tilde{E}_{z_n} \\ \tilde{H}_{z_n} \end{bmatrix} \tag{B.12}$$

where $\tilde{E}_{z_n}$ and $\tilde{H}_{z_n}$ are the n^{th} harmonics of E_z and H_z, respectively, such that

$$\begin{bmatrix} \tilde{E}_{z_n} \\ \tilde{H}_{z_n} \end{bmatrix} = \begin{cases} [J_n(k_\rho \rho)\bar{I} + H_n^{(2)}(k_\rho \rho)\bar{R}] H_n^{(2)}(k_\rho \rho') \overleftarrow{S}, & \rho < \rho' \\ H_n^{(2)}(k_\rho \rho)[J_n(k_\rho \rho')\bar{I} + H_n^{(2)}(k_\rho \rho')\bar{R}] \overleftarrow{S}, & \rho > \rho' \end{cases} \tag{B.13}$$

where $\bar{I}$ and $\bar{R}$ are identity and reflection matrices, respectively.

Using the Maxwell's equations, E_ϕ and H_ϕ can be written in terms of E_z and H_z such that

$$(k^2 + \frac{\partial^2}{\partial z^2}) \begin{bmatrix} H_\phi \\ E_\phi \end{bmatrix} = \frac{1}{\rho} \begin{bmatrix} -jZ_0^{-1} k\rho \partial/\partial\rho & \partial^2/\partial z \partial\phi \\ \partial^2/\partial z \partial\phi & jZ_0 k\rho \partial/\partial\rho \end{bmatrix} \begin{bmatrix} E_z \\ H_z \end{bmatrix} \tag{B.14}$$

in which the n^{th} harmonics of E_ϕ and H_ϕ, $\tilde{E}_{\phi_n}$ and $\tilde{H}_{\phi_n}$ are related to $\tilde{E}_{z_n}$ and $\tilde{H}_{z_n}$ as follows:

$$\begin{bmatrix} \tilde{H}_{\phi_n} \\ \tilde{E}_{\phi_n} \end{bmatrix} = \frac{1}{k_\rho^2 \rho} \begin{bmatrix} -jZ_0^{-1} k\rho \partial/\partial\rho & nk_z \\ nk_z & jZ_0 k\rho \partial/\partial\rho \end{bmatrix} \begin{bmatrix} \tilde{E}_{z_n} \\ \tilde{H}_{z_n} \end{bmatrix}. \tag{B.15}$$

Thus, $\hat{\phi}$ components of the electric and magnetic fields, E_ϕ and H_ϕ, can be expressed as

$$\begin{bmatrix} H_\phi \\ E_\phi \end{bmatrix} = \frac{1}{2\pi}\int_{-\infty}^{\infty} dk_z e^{-jk_z z_d} \sum_{n=-\infty}^{\infty} e^{jn\phi_d} \begin{bmatrix} \tilde{H}_{\phi_n} \\ \tilde{E}_{\phi_n} \end{bmatrix} \tag{B.16}$$

such that

$$\left[\begin{array}{c} \tilde{H}_{\phi_n} \\ \tilde{E}_{\phi_n} \end{array}\right] = \begin{cases} [\bar{J}_n(k_\rho\rho)\bar{I} + \bar{H}_n^{(2)}(k_\rho\rho)\bar{R}]H_n^{(2)}(k_\rho\rho')\overleftarrow{S}, & \rho < \rho' \\ \bar{H}_n^{(2)}(k_\rho\rho)[J_n(k_\rho\rho')\bar{I} + H_n^{(2)}(k_\rho\rho')\bar{R}]\overleftarrow{S}, & \rho > \rho' \end{cases} \tag{B.17}$$

in which

$$\bar{B}_n(k_\rho\rho) = \frac{1}{k_\rho^2\rho}\left[\begin{array}{cc} -jZ_0^{-1}kk_\rho\rho B_n'(k_\rho\rho) & nk_zB_n(k_\rho\rho) \\ nk_zB_n(k_\rho\rho) & jZ_0kk_\rho\rho B_n'(k_\rho\rho) \end{array}\right] \tag{B.18}$$

where B_n is either J_n or $H_n^{(2)}$ depending on whether $\bar{B}_n = \bar{J}_n$ or $\bar{B}_n = \bar{H}_n^{(2)}$ is evaluated, respectively, and $'$ denotes the derivative with respect to the argument.

The tangential components of the fields have to satisfy the following IBC [46]

$$\left[\begin{array}{c} E_z \\ H_z \end{array}\right]\Bigg|_{\rho=a} = \bar{Z}_s\left[\begin{array}{c} H_\phi \\ E_\phi \end{array}\right]\Bigg|_{\rho=a} \tag{B.19}$$

on the surface of the cylinder with

$$\bar{Z}_s = \left[\begin{array}{cc} Z_s & 0 \\ 0 & -Z_s^{-1} \end{array}\right]. \tag{B.20}$$

Since the source is not on the cylinder yet, the expressions for $\rho < \rho'$ in (B.13) and (B.17) are inserted into the IBC for the n^{th} harmonics

$$\left[\begin{array}{c} \tilde{E}_{z_n} \\ \tilde{H}_{z_n} \end{array}\right]\Bigg|_{\rho=a} = \bar{Z}_s\left[\begin{array}{c} \tilde{H}_{\phi_n} \\ \tilde{E}_{\phi_n} \end{array}\right]\Bigg|_{\rho=a} \tag{B.21}$$

to obtain the reflection matrix given by

$$\bar{R} = -[H_n^{(2)}(k_\rho a)\bar{I} - \bar{Z}_s\bar{H}_n^{(2)}(k_\rho a)]^{-1}[J_n(k_\rho a)\bar{I} - \bar{Z}_s\bar{J}_n(k_\rho a)]. \tag{B.22}$$

First, we substitute (B.22) into (B.13) and (B.17). Then, inserting (B.13) and (B.17) into (B.12) and (B.16), respectively, for $\rho > \rho'$, and setting $\rho' = a$ (source is placed on the cylinder), tangential electric and magnetic fields due to the tangential magnetic source given by (B.2) are obtained as

$$\begin{aligned} E_z &= \frac{1}{4\pi^2 a}\int_{-\infty}^{\infty} dk_z e^{-jk_z z_d} \sum_{n=-\infty}^{\infty} e^{jn\phi_d} \frac{N^c_{\phi z} P^z_m + N^c_{\phi\phi} P^\phi_m}{D_c} \\ &\quad \frac{H^{(2)}_n(k_\rho \rho)}{H^{(2)}_n(k_\rho a)} && \text{(B.23)} \\ H_z &= -\frac{1}{4\pi^2 a Z_s}\int_{-\infty}^{\infty} dk_z e^{-jk_z z_d} \sum_{n=-\infty}^{\infty} e^{jn\phi_d} \frac{N^c_{zz} P^z_m + N^c_{z\phi} P^\phi_m}{D_c} \\ &\quad \frac{H^{(2)}_n(k_\rho \rho)}{H^{(2)}_n(k_\rho a)} && \text{(B.24)} \\ H_\phi &= -\frac{1}{4\pi^2 a Z_s}\int_{-\infty}^{\infty} dk_z e^{-jk_z z_d} \sum_{n=-\infty}^{\infty} e^{jn\phi_d} \left[\frac{nk_z}{k_\rho^2 \rho} \frac{N^c_{zz} P^z_m + N^c_{z\phi} P^\phi_m}{D_c}\right. \\ &\quad \left. -\frac{j\Lambda k}{k_\rho} \frac{H^{(2)}_n(k_\rho \rho)}{H^{(2)}_n(k_\rho a)} \frac{N^c_{\phi z} P^z_m + N^c_{\phi\phi} P^\phi_m}{D_c}\right] \frac{H^{(2)}_n(k_\rho \rho)}{H^{(2)}_n(k_\rho a)} && \text{(B.25)} \end{aligned}$$

where

$$\begin{aligned} R_n &= \frac{H^{(2)'}_n(k_\rho a)}{H^{(2)}_n(k_\rho a)} && \text{(B.26)} \\ N^c_{zz} &= 1 + \frac{j\Lambda k}{k_\rho} R_n && \text{(B.27)} \\ N^c_{z\phi} &= N^c_{\phi z} = \frac{nk_z}{k_\rho^2 a} && \text{(B.28)} \\ N^c_{\phi\phi} &= 1 + \frac{j\Lambda^{-1} k}{k_\rho} R_n && \text{(B.29)} \\ D_c &= N^c_{zz} N^c_{\phi\phi} + N^c_{z\phi} N^c_{\phi z} && \text{(B.30)} \end{aligned}$$

in which Λ is the normalized surface impedance and defined as Z_s/Z_0.

B.2 Impedance Sphere

The starting point of the formulation is similar to that of [5], where a vector potential $\bar{F}_0$ due to a source $\bar{M}$ in the absence of the impedance sphere can be represented by an infinite sum of spherical wave functions of the form

$$\bar{F}_0 = \hat{x}\frac{kp_m}{4\pi j}\sum_{n=0}^{\infty}(2n+1)h^{(2)}_n(kr')j_n(kr)P_n(\cos\theta); \qquad |\bar{r}| < |\bar{r}'| \qquad \text{(B.31)}$$

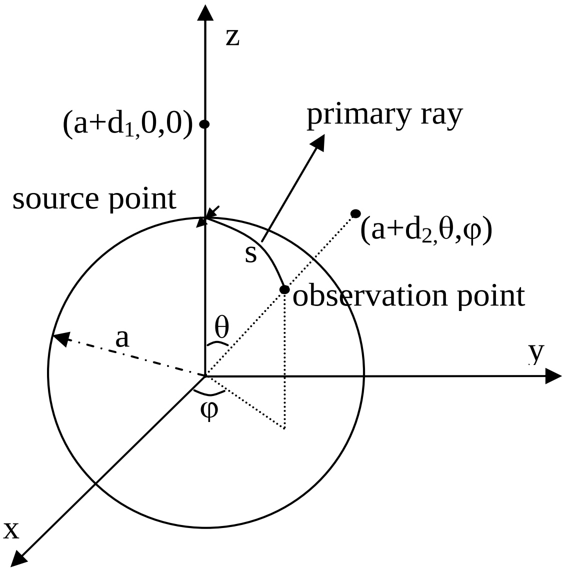

Figure B.1: Problem geometry for an impedance sphere

where j_n, $h_n^{(2)}$ and P_n are the usual spherical Bessel, Hankel and Legendre functions [47], respectively. Defining a set of potentials, $\psi_0^e\hat{r}$ and $\psi_0^m\hat{r}$ associated with $\bar{M}$ in free space that satisfy

$$(\nabla^2 + k^2)\left\{ \begin{array}{c} \psi_0^e/r \\ \psi_0^m/r \end{array} \right\} = 0; \qquad r \neq 0 \tag{B.32}$$

are related to $\bar{F}_0$ via

$$\sin\phi \frac{\partial F_0}{\partial \theta} = \frac{-1}{jkY_0}\Delta^*(\frac{\psi_0^e}{r}) \tag{B.33}$$

$$\cos\phi\left[\frac{\partial}{\partial\theta}\left(\frac{\partial F_0}{\partial b} + \frac{F_0}{b}\right)\right] = \Delta^*(\frac{\psi_0^m}{r}) \tag{B.34}$$

where the operator Δ^* is defined by [5] as

$$\Delta^* = \frac{1}{\sin\theta}\frac{\partial}{\partial\theta}(\sin\theta\frac{\partial}{\partial\theta}) + \frac{1}{\sin^2\theta}\frac{\partial^2}{\partial\phi^2}, \tag{B.35}$$

and the source is initially assumed to be at $\bar{r}' = (a + d_1)\hat{z} = b\hat{z}$ as illustrated in Fig.B.1. In (B.33), $Y_0 = 1/Z_0$ is the free-space admittance. Substituting (B.31) into (B.33) and (B.34), and using the properties given by [48]

$$\hat{J}_n(kr) = krj_n(kr) \tag{B.36}$$

$$\hat{H}_n^{(2)}(kr) = krh_n^{(2)}(kr) \tag{B.37}$$

$$\frac{\partial}{\partial\theta}P_n(\cos\theta) = P_n^1(\cos\theta) \tag{B.38}$$

ψ_0^e and ψ_0^m can be expressed as

$$\psi_0^e = \left(\frac{kp_m}{4\pi j}\right)\left(\frac{jY_0\sin\phi}{kb}\right)\sum_{n=1}^{\infty}\frac{2n+1}{n(n+1)}\hat{H}_n^{(2)}(kb)\hat{J}_n(kr)P_n^1(\cos\theta) \quad \text{(B.39)}$$

$$\psi_0^m = \left(\frac{kp_m}{4\pi j}\right)\left(\frac{-\cos\phi}{kb}\right)\sum_{n=1}^{\infty}\frac{2n+1}{n(n+1)}\hat{H}_n^{(2)\prime}(kb)\hat{J}_n(kr)P_n^1(\cos\theta) \quad \text{(B.40)}$$

where $'$ denotes the derivative with respect to the argument. The scattered fields due to the presence of the impedance sphere are in similar form to those of incident fields (i.e., in the form of an infinite sum of spherical wave functions) except some complex coefficients to be found from the appropriate boundary conditions. Thus, defining another set of potentials to account for the scattering from the impedance sphere, and superposing them with the free-space potentials defined in (B.39)-(B.40), the total potentials are given by

$$\begin{aligned}\psi^e = {} & \left(\frac{kp_m}{4\pi j}\right)\left(\frac{jY_0\sin\phi}{kb}\right)\sum_{n=1}^{\infty}\frac{2n+1}{n(n+1)}\hat{H}_n^{(2)}(kb) \\ & \left(\hat{J}_n(kr)+C_{1n}\hat{H}_n^{(2)}(kr)\right)P_n^1(\cos\theta) \qquad \text{(B.41)}\\ \psi^m = {} & \left(\frac{kp_m}{4\pi j}\right)\left(\frac{-\cos\phi}{kb}\right)\sum_{n=1}^{\infty}\frac{2n+1}{n(n+1)}\hat{H}_n^{(2)\prime}(kb) \\ & \left(\hat{J}_n(kr)+C_{2n}\hat{H}_n^{(2)}(kr)\right)P_n^1(\cos\theta). \qquad \text{(B.42)}\end{aligned}$$

In (B.41) and (B.42), C_{1n} and C_{2n} are the complex coefficients to be found by applying the impedance boundary conditions at $r = a$ given by

$$\begin{bmatrix} E_\phi \\ H_\phi \end{bmatrix} = \begin{bmatrix} Z_s & 0 \\ 0 & -Z_s^{-1} \end{bmatrix}\begin{bmatrix} H_\theta \\ E_\theta \end{bmatrix}. \qquad \text{(B.43)}$$

Therefore, calculating E_ϕ and H_θ from ψ^e and ψ^m using [49]

$$E_\phi = \frac{1}{r}\frac{\partial\psi^m}{\partial\theta} + \frac{1}{jkY_0 r\sin\theta}\frac{\partial^2\psi^e}{\partial r\partial\phi} \qquad \text{(B.44)}$$

$$H_\theta = \frac{1}{r\sin\theta}\frac{\partial\psi^e}{\partial\phi} + \frac{1}{jkZ_0 r}\frac{\partial^2\psi^m}{\partial r\partial\theta}, \qquad \text{(B.45)}$$

and substituting the results into (B.43), the complex coefficients C_{1n} and C_{2n} are obtained as

$$C_{1n} = -\frac{\hat{J}_n(ka)+j\Lambda^{-1}\hat{J}_n'(ka)}{\hat{H}_n^{(2)}(ka)+j\Lambda^{-1}\hat{H}_n^{(2)\prime}(ka)} \qquad \text{(B.46)}$$

$$C_{2n} = -\frac{\hat{J}_n(ka) + j\Lambda \hat{J}_n'(ka)}{\hat{H}_n^{(2)}(ka) + j\Lambda \hat{H}_n^{(2)'}(ka)} \tag{B.47}$$

where Λ is the normalized surface impedance and defined as Z_s/Z_0.

Finally, substituting (B.46) and (B.47) into (B.41) and (B.42), respectively, the exact expressions for ψ^e and ψ^m can be found as

$$\psi^e = \left(\frac{kp_m}{4\pi j}\right)\left(\frac{jY_0 \sin\phi}{kb}\right)\sum_{n=1}^{\infty}\frac{2n+1}{n(n+1)}\hat{H}_n^{(2)}(kb)\tilde{A}_n(kr)P_n^1(\cos\theta) \tag{B.48}$$

$$\psi^m = \left(\frac{kp_m}{4\pi j}\right)\left(\frac{-\cos\phi}{kb}\right)\sum_{n=1}^{\infty}\frac{2n+1}{n(n+1)}\hat{H}_n^{(2)'}(kb)\tilde{B}_n(kr)P_n^1(\cos\theta) \tag{B.49}$$

where

$$\tilde{A}_n(kr) = \hat{J}_n(kr) - \frac{\hat{J}_n(ka) + j\Lambda^{-1}\hat{J}_n'(ka)}{\hat{H}_n^{(2)}(ka) + j\Lambda^{-1}\hat{H}_n^{(2)'}(ka)}\hat{H}_n^{(2)}(kr) \tag{B.50}$$

$$\tilde{B}_n(kr) = \hat{J}_n(kr) - \frac{\hat{J}_n(ka) + j\Lambda \hat{J}_n'(ka)}{\hat{H}_n^{(2)}(ka) + j\Lambda \hat{H}_n^{(2)'}(ka)}\hat{H}_n^{(2)}(kr). \tag{B.51}$$

The tangential magnetic field components are found by inserting these potentials into (B.45) and

$$H_\phi = -\frac{1}{r}\frac{\partial\psi_e}{\partial\theta} + \frac{1}{jkZ_0 r sin\theta}\frac{\partial^2\psi_m}{\partial r\partial\phi} \tag{B.52}$$

Therefore, substituting (B.48) and (B.49) into (B.45) and (B.52), and using the following identities

$$\hat{J}_n'(kr) = (n+1)\hat{J}_n(kr) - kr\hat{J}_n n + 1(kr) \tag{B.53}$$

$$\hat{H}_n^{(2)'}(kr) = (n+1)\hat{H}_n^{(2)}(kr) - kr\hat{H}_{n+1}^{(2)}(kr) \tag{B.54}$$

one obtains

$$\begin{aligned}
H_\phi \;=\; & -\frac{1}{r}\left(\frac{kp_m}{4\pi j}\right)\left(\frac{jY_0\sin\phi}{kb}\right)\sum_{n=1}^{\infty}\frac{2n+1}{n(n+1)}kb\hat{H}_n^{(2)}(kb)\Bigg\{kr\hat{J}_n(kr) \\
& -\frac{ka\hat{J}_n(ka)+j\Lambda^{-1}[(n+1)\hat{J}_n(ka)-kr\hat{J}_{n+1}(ka)]}{ka\hat{H}_n^{(2)}(ka)+j\Lambda^{-1}[(n+1)\hat{H}_n^{(2)}(ka)-kr\hat{H}_{n+1}^{(2)}(ka)]}kr\hat{H}_n^{(2)}(kr)\Bigg\} \\
& \frac{\partial P_n^1(\cos\theta)}{\partial\theta}+\frac{1}{jkZ_0rsin\theta}\left(\frac{kp_m}{4\pi j}\right)\left(\frac{\sin\phi}{kb}\right)\sum_{n=1}^{\infty}\frac{2n+1}{n(n+1)} \\
& [(n+1)\hat{H}_n^{(2)}(kb)-kb\hat{H}_{n+1}^{(2)}(kb)]k\Bigg\{[(n+1)\hat{J}_n(kr)-kr\hat{J}_{n+1}(kr)] \\
& -\frac{ka\hat{J}_n(ka)+j\Lambda[(n+1)\hat{J}_n(ka)-kr\hat{J}_{n+1}(ka)]}{ka\hat{H}_n^{(2)}(ka)+j\Lambda[(n+1)\hat{H}_n^{(2)}(ka)-kr\hat{H}_{n+1}^{(2)}(ka)]}kr\hat{H}_n^{(2)}(kr) \\
& [(n+1)\hat{H}_n^{(2)}(kr)-kr\hat{H}_{n+1}^{(2)}(kr)]\Bigg\}P_n^1(\cos\theta) \qquad \text{(B.55)}
\end{aligned}$$

$$\begin{aligned}
H_\theta \;=\; & -\frac{1}{a}\left(\frac{kp_m}{4\pi j}\right)jY_0\sin\phi\sum_{n=1}^{\infty}\frac{2n+1}{n(n+1)}\hat{H}_n^{(2)}(ka) \\
& \left\{\frac{\Lambda^{-1}}{ka\hat{H}_n^{(2)}(ka)+j\Lambda^{-1}[(n+1)\hat{H}_n^{(2)}(ka)-ka\hat{H}_{n+1}^{(2)}(ka)]}\right\} \\
& \frac{\partial P_n^1(\cos\theta)}{\partial\theta}+\frac{1}{jkZ_0asin\theta}\left(\frac{kp_m}{4\pi j}\right)\left(\frac{\sin\phi}{ka}\right)\sum_{n=1}^{\infty}\frac{2n+1}{n(n+1)} \\
& [(n+1)\hat{H}_n^{(2)}(ka)-ka\hat{H}_{n+1}^{(2)}(ka)] \\
& \left\{\frac{jk}{ka\hat{H}_n^{(2)}(ka)+j\Lambda[(n+1)\hat{H}_n^{(2)}(ka)-ka\hat{H}_{n+1}^{(2)}(ka)]}\right\} \\
& P_n^1(\cos\theta). \qquad \text{(B.56)}
\end{aligned}$$

Finally, the expressions $r' = b = a$ and $r = a$ (source and observation points are on the sphere) are introduced. After doing some algebra and using the identity

$$\hat{H}_n^{(2)}(ka)\hat{J}_{n+1}(ka)-\hat{H}_{n+1}^{(2)}(ka)\hat{J}_n(ka)=-j/(ka)^2, \qquad \text{(B.57)}$$

the tangential magnetic field components are written as follows:

$$\begin{aligned}
H_\phi &= \sin\phi \frac{k^2 Y_0 p_m}{4\pi} \sum_{n=1}^{\infty} \frac{2n+1}{n(n+1)} \frac{j}{(ka)^2} \\
&\left\{ \left[-j\Lambda + \frac{(n+1)}{ka} - \frac{\hat{H}_{n+1}^{(2)}(ka)}{\hat{H}_n^{(2)}(ka)} \right]^{-1} \frac{\partial P_n^1(\cos\theta)}{\partial\theta} \right. \\
&\left. - \frac{1}{\sin\theta} \left[\frac{\frac{(n+1)}{ka} - \frac{\hat{H}_{n+1}^{(2)}(ka)}{\hat{H}_n^{(2)}(ka)}}{1 + j\Lambda\left(\frac{(n+1)}{ka} - \frac{\hat{H}_{n+1}^{(2)}(ka)}{\hat{H}_n^{(2)}(ka)} \right)} \right] P_n^1(\cos\theta) \right\}
\end{aligned} \tag{B.58}$$

$$\begin{aligned}
H_\theta &= -\cos\phi \frac{k^2 Y_0 p_m}{4\pi} \sum_{n=1}^{\infty} \frac{2n+1}{n(n+1)} \frac{j}{(ka)^2} \\
&\left\{ \frac{1}{\sin\theta} \left[-j\Lambda + \frac{(n+1)}{ka} - \frac{\hat{H}_{n+1}^{(2)}(ka)}{\hat{H}_n^{(2)}(ka)} \right]^{-1} P_n^1(\cos\theta) \right. \\
&\left. - \left[\frac{\frac{(n+1)}{ka} - \frac{\hat{H}_{n+1}^{(2)}(ka)}{\hat{H}_n^{(2)}(ka)}}{1 + j\Lambda\left(\frac{(n+1)}{ka} - \frac{\hat{H}_{n+1}^{(2)}(ka)}{\hat{H}_n^{(2)}(ka)} \right)} \right] \frac{\partial P_n^1(\cos\theta)}{\partial\theta} \right\}.
\end{aligned} \tag{B.59}$$

Appendix C

Derivation of asymptotic solution pertaining to the circular cylinder

C.1 PEC Circular Cylinder

For a PEC cylinder, $\hat{z}$ components of the electric and magnetic fields due to a tangential magnetic source

$$\vec{P}_m = P_m^z \hat{z} + P_m^\phi \hat{\phi} \tag{C.1}$$

located on the surface $\rho = a$ (see Fig. 2.1) is expressed in [10] as

$$\begin{aligned} E_z &= -\frac{1}{4\pi^2 a} \int_{-\infty}^{\infty} dk_z e^{-jk_z z_d} \sum_{n=-\infty}^{\infty} e^{jn\phi_d} \frac{P_m^\phi}{k_\rho^2 a} \frac{H_n^{(2)}(k_\rho \rho)}{H_n^{(2)}(k_\rho a)} && \text{(C.2)} \\ H_z &= \frac{1}{4\pi^2 ajkZ_0} \int_{-\infty}^{\infty} dk_z e^{-jk_z z_d} \sum_{n=-\infty}^{\infty} e^{jn\phi_d} [\frac{-P_m^z}{k\rho} + \frac{nk_z}{k_\rho^3 a} P_m^\phi] \\ & \quad \frac{H_n^{(2)}(k_\rho \rho)}{H_n^{(2)'}(k_\rho a)} && \text{(C.3)} \end{aligned}$$

where $z_d = z - z'$, $\phi_d = \phi - \phi'$, k_z and k_ρ are the axial and radial wave numbers, respectively, such that

$$k_\rho = \begin{cases} \sqrt{k^2 - k_z^2} & \text{if } k^2 \geq k_z^2 \\ -j\sqrt{k_z^2 - k^2} & \text{if } k^2 < k_z^2. \end{cases} \tag{C.4}$$

Once the $\hat{z}$ components of the fields (E_z, H_z) are obtained, the vector potentials (A_z, F_z) due to these components can easily be found using the methods described in [49]. Then, the procedure explained in [19] is followed. Briefly, first the Watson transform [50] is applied to the potentials to obtain

$$A_z = \sum_{\ell=0}^{\infty}(A_{z_\ell}^{+} + A_{z_\ell}^{-}) \tag{C.5}$$

$$F_z = \sum_{\ell=0}^{\infty}(F_{z_\ell}^{+} + F_{z_\ell}^{-}) \tag{C.6}$$

where $A_{z_\ell}^{+}$ and $F_{z_\ell}^{+}$ pertain the surface waves propagating around the cylinder in the positive $\hat{\phi}$ direction, whereas $A_{z_\ell}^{-}$ and $F_{z_\ell}^{-}$ correspond to those propagating in the negative $\hat{\phi}$ direction.

Thereby the potentials are expressed as double integrals over the axial (k_z) and the azimuthal (ν) wavenumbers such that

$$A_{z_\ell}^{\pm} = -\frac{jk}{4\pi^2 a Z_0}\int_{-\infty}^{\infty} dk_z e^{-jk_z z_d}\int_{-\infty}^{\infty} d\nu e^{-j\nu\phi_\ell^{\pm}} \frac{P_m^{\phi}}{k_\rho^2 a}\frac{H_\nu^{(2)}(k_\rho\rho)}{H_\nu^{(2)}(k_\rho a)} \tag{C.7}$$

$$F_{z_\ell}^{\pm} = \frac{1}{4\pi^2 a}\int_{-\infty}^{\infty} dk_z e^{-jk_z z_d}\int_{-\infty}^{\infty} d\nu e^{-j\nu\phi_\ell^{\pm}}[\frac{-P_m^{z}}{k_\rho} + \frac{\nu k_z}{k_\rho^3 a}P_m^{\phi}]\frac{H_\nu^{(2)}(k_\rho\rho)}{H_\nu^{(2)'}(k_\rho a)} \tag{C.8}$$

where

$$\phi_\ell^{\pm} = \pm(\phi - \phi' - \pi) + (2\ell + 1)\pi. \tag{C.9}$$

Employing a Fock-substitution $(\nu = k_\rho a + m_t\tau)$, integration in the ν-plane is replaced by an integration in the τ-plane as follows:

$$A_{z_\ell}^{\pm} = \frac{jk}{4\pi^2 a Z_0}\int_{-\infty}^{\infty} dk_z e^{-j(k_z z_d + k_\rho a\phi_\ell^{\pm})}\int_{-\infty}^{\infty} d\tau e^{-j\xi\tau} m_t \frac{P_m^{\phi}}{k_\rho^2 a}\frac{H_\nu^{(2)}(k_\rho\rho)}{H_\nu^{(2)}(k_\rho a)} \tag{C.10}$$

$$F_{z_\ell}^{\pm} = \frac{1}{4\pi^2 a}\int_{-\infty}^{\infty} dk_z e^{-j(k_z z_d + k_\rho a\phi_\ell^{\pm})}\int_{-\infty}^{\infty} d\tau e^{-j\xi\tau} m_t$$

$$[\frac{-P_m^{z}}{k_\rho} + (k_\rho a + \frac{\tau}{2m_t^2 k_\rho^2})P_m^{\phi}]\frac{H_\nu^{(2)}(k_\rho\rho)}{H_\nu^{(2)'}(k_\rho a)}. \tag{C.11}$$

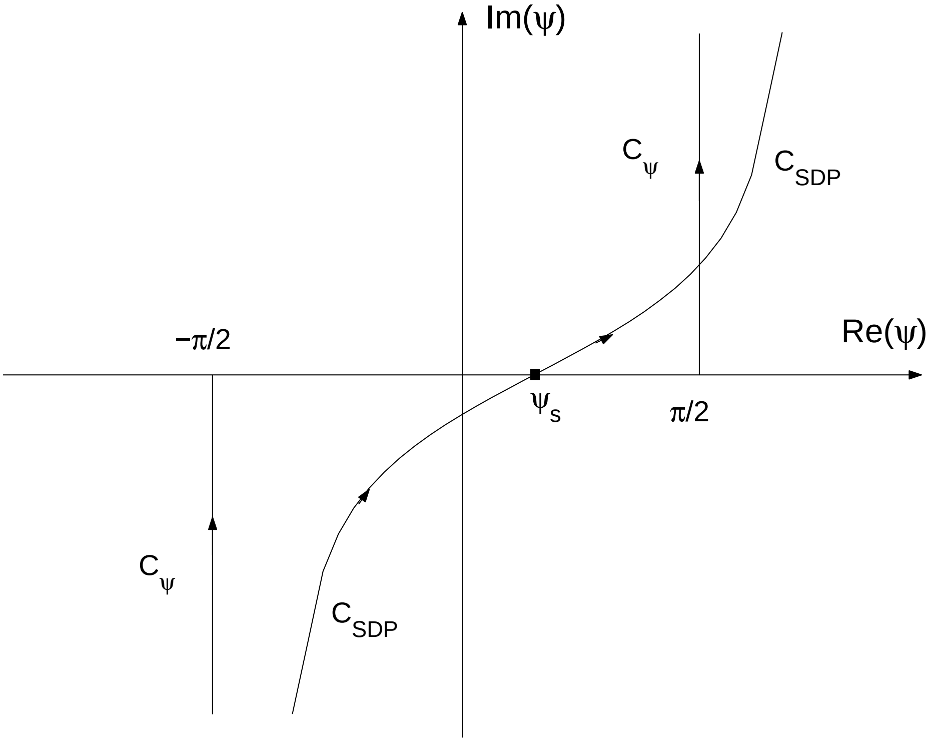

Figure C.1: Integration paths, C_ψ and C_{SDP} , on the complex ψ plane

Then, introducing the standard polar transformations

$$k_\rho = k\cos\psi \;, \quad k_z = k\sin\psi, \tag{C.12}$$

along with the geometrical relations (see Fig. 2.1)

$$a\phi_\ell^\pm = s\cos\alpha \;, \quad z_d = s\sin\alpha, \tag{C.13}$$

integration over k_z is converted to a complex contour integral C_ψ as shown in Fig. C.1. The relevant vector potential expressions to find the surface magnetic field are given as

$$\left.\frac{\partial A^\pm_{z_\ell}}{\partial\rho}\right|_{\rho=a} = -\frac{jkP^\phi_m}{4\pi^2 aZ_0}\int_{C_\psi} d\psi e^{-jks\cos(\psi-\alpha)}\int_{-\infty}^{\infty} d\tau e^{-j\xi\tau}\frac{W_2'(\tau)}{W_2(\tau)} \tag{C.14}$$

$$\left.F^\pm_{z_\ell}\right|_{\rho=a} = \frac{1}{4\pi^2 a}\int_{C_\psi} d\psi e^{-jks\cos(\psi-\alpha)}\int_{-\infty}^{\infty} d\tau e^{-j\xi\tau} [\frac{-P^z_m}{k_\rho} + k_\rho aP^\phi_m]\frac{W_2(\tau)}{W_2'(\tau)} \tag{C.15}$$

which are evaluated on the surface of the cylinder ($\rho = a$). In Eqs.(C.14) and (C.15), higher order terms are neglected and Hankel functions are approximated by the Fock type Airy functions as follows:

$$\begin{aligned} H_\nu^{(2)}(k_\rho a) &\sim \frac{j}{\sqrt{\pi}} m_t^{-1} W_2(\tau) \qquad (C.16)\\ H_\nu^{(2)'}(k_\rho a) &\sim \frac{-j}{\sqrt{\pi}} m_t^{-2} W_2'(\tau). \qquad (C.17)\end{aligned}$$

Complex contour integral is evaluated applying the method of steepest descent (see Fig. C.1) assuming that the separation s between the source and field points is the large parameter (with respect to wavelength), resulting

$$\begin{aligned} \left.\frac{\partial A_{z_\ell}^\pm}{\partial \rho}\right|_{\rho=a} &\sim -P_m^\phi \frac{j}{ks} \frac{U}{\cos^2\alpha} G_0 \qquad (C.18)\\ \left. F_{z_\ell}^\pm \right|_{\rho=a} &\sim \frac{jZ_0}{k}(P_m^z - \cot\alpha P_m^\phi) V G_0 \qquad (C.19)\end{aligned}$$

where

$$G_0 = -\frac{jk^2 e^{-jks}}{2\pi Z_0 ks} \qquad (C.20)$$

$$U = j\xi\sqrt{\frac{j\xi}{\pi}} \int_{-\infty}^{\infty} d\tau e^{-j\xi\tau} \frac{W_2'(\tau)}{W_2(\tau)} \qquad (C.21)$$

$$V = \sqrt{\frac{j\xi}{4\pi}} \int_{-\infty}^{\infty} d\tau e^{-j\xi\tau} \frac{W_2(\tau)}{W_2'(\tau)}. \qquad (C.22)$$

The field expressions are then obtained by performing the derivatives to the resultant potential expressions analytically using the following tangential surface magnetic field expression:

$$\vec{H}_{t_\ell}^\pm = -\frac{j}{kZ_0}\left.[\hat{z}(\frac{\partial^2}{\partial z_d^2} + k^2) F_{z_\ell}^\pm + \hat{\phi}(\pm\frac{a}{\rho}\frac{\partial^2 F_{z_\ell}^\pm}{\partial y_\ell \partial z_d} - jZ_0 k \frac{\partial A_{z_\ell}^\pm}{\partial \rho})]\right|_{\rho=a}. \qquad (C.23)$$

Finally, from (C.23), the UTD-based asymptotic Green's function representations that give the tangential surface magnetic field components for a tangential magnetic source on a PEC cylinder can be written as

$$G_{zz}^{\ell\pm} \sim G_0\left\{\cos^2\alpha V + \frac{j}{ks}\left(1-\frac{j}{ks}\right)\left(2-3\cos^2\alpha\right)V\right\} \tag{C.24}$$

$$G_{z\phi}^{\ell\pm} \sim \mp G_0\left\{\cos\alpha\sin\alpha\left[1-\frac{j3}{ks}\left(1-\frac{j}{ks}\right)\right]V\right\} \tag{C.25}$$

$$G_{\phi z}^{\ell\pm} \sim \mp G_0\left\{\cos\alpha\sin\alpha\left[1-\frac{j3}{ks}\left(1-\frac{j}{ks}\right)V\right]\right\} \tag{C.26}$$

$$\begin{aligned} G_{\phi\phi}^{\ell\pm} \sim G_0\Bigg\{&\sin^2\alpha V + \frac{j}{ks}\left(1-\frac{j}{ks}\right)\left(2-3\sin^2\alpha\right)V \\ &+\frac{j}{ks}\frac{1}{\cos^2\alpha}\left(U-V\right)\Bigg\}. \end{aligned} \tag{C.27}$$

C.2 Impedance Circular Cylinder

For an impedance cylinder, $\hat{z}$ components of the electric and magnetic fields due to a tangential magnetic source

$$\vec{P}_m = P_m^z\hat{z} + P_m^\phi\hat{\phi} \tag{C.28}$$

located on the surface $\rho = a$ (see Fig. 2.1) is expressed in [19] as

$$\begin{aligned} E_z = &\frac{1}{4\pi^2 a}\int_{-\infty}^{\infty} dk_z e^{-jk_z z_d}\sum_{n=-\infty}^{\infty}\frac{e^{jn\phi_d}}{D_c}\left[\frac{nk_z}{k_\rho^2 a}P_m^z + \left(1+\frac{j\Lambda^{-1}k}{k_\rho}R_n\right)P_m^\phi\right] \\ &\frac{H_n^{(2)}(k_\rho\rho)}{H_n^{(2)}(k_\rho a)} \end{aligned} \tag{C.29}$$

$$\begin{aligned} H_z = &-\frac{1}{4\pi^2 a Z_s}\int_{-\infty}^{\infty} dk_z e^{-jk_z z_d}\sum_{n=-\infty}^{\infty}\frac{e^{jn\phi_d}}{D_c}\left[\left(1+\frac{j\Lambda k}{k_\rho}R_n\right)P_m^z + \frac{nk_z}{k_\rho^2 a}P_m^\phi\right] \\ &\frac{H_n^{(2)}(k_\rho\rho)}{H_n^{(2)}(k_\rho a)} \end{aligned} \tag{C.30}$$

where

$$R_n = \frac{H_n^{(2)'}(k_\rho a)}{H_n^{(2)}(k_\rho a)} \tag{C.31}$$

$$D_c = \left(1+\frac{j\Lambda k}{k_\rho}R_n\right)\left(1+\frac{j\Lambda^{-1}k}{k_\rho}R_n\right) - \left(\frac{nk_z}{k_\rho^2 a}\right)^2 \tag{C.32}$$

and where $z_d = z - z'$, $\phi_d = \phi - \phi'$, k_z and k_ρ are the axial and radial wave numbers, respectively, such that

$$k_\rho = \begin{cases} \sqrt{k^2 - k_z^2} & \text{if } k^2 \geq k_z^2 \\ -j\sqrt{k_z^2 - k^2} & \text{if } k^2 < k_z^2. \end{cases} \tag{C.33}$$

Using the $\hat{z}$ components of the fields (E_z, H_z), the vector potentials (A_z, F_z) due to these components are found via the methods described in [49]. Then, the procedure for the development of high frequency solutions, which is explained in [19], is followed. In this procedure, Watson transform [50] is applied to the potentials and thereby the potentials are expressed as double integrals over the axial (k_z) and azimuthal (ν) wavenumbers such that

$$\begin{aligned} A_{z_\ell}^{\pm} &= -\frac{j}{4\pi^2 a Z_0 k} \int_{-\infty}^{\infty} dk_z e^{-jk_z z_d} \int_{-\infty}^{\infty} d\nu e^{-j\nu\phi_\ell^{\pm}} \frac{1}{D_\nu} \\ & \quad (\pm \frac{\nu k_z}{k_\rho^2 a} P_m^z + (1 + \frac{j\Lambda^{-1} k}{k_\rho} R_\nu) P_m^\phi] \frac{H_\nu^{(2)}(k_\rho \rho)}{H_\nu^{(2)}(k_\rho a)} &\text{(C.34)} \\ F_{z_\ell}^{\pm} &= \frac{j}{4\pi^2 a \Lambda k} \int_{-\infty}^{\infty} dk_z e^{-jk_z z_d} \int_{-\infty}^{\infty} d\nu e^{-j\nu\phi_\ell^{\pm}} \frac{1}{D_\nu} \\ & \quad [(1 + \frac{j\Lambda k}{k_\rho} R_\nu) P_m^z \mp \frac{\nu k_z}{k_\rho^2 a} P_m^\phi] \frac{H_\nu^{(2)}(k_\rho \rho)}{H_\nu^{(2)}(k_\rho a)} &\text{(C.35)} \end{aligned}$$

where

$$D_\nu = (R_\nu - \frac{j\Lambda k_\rho}{k})(R_\nu - \frac{j\Lambda^{-1} k_\rho}{k}) - (\frac{\nu k_z}{k k_\rho a})^2 \tag{C.36}$$

$$R_\nu = \frac{H_\nu^{(2)'}(k_\rho a)}{H_\nu^{(2)}(k_\rho a)}. \tag{C.37}$$

After employing a Fock-substitution ($\nu = k_\rho a + m_t \tau$), integration in the ν-plane is replaced by an integration in the τ-plane, and the new expressions for the potentials are given by

$$\begin{aligned}
A_{z_\ell}^{\pm} &= -\frac{j}{4\pi^2 a Z_0 k}\int_{-\infty}^{\infty} dk_z e^{-j(k_z z_d + k_\rho a\phi_\ell^{\pm})}\int_{-\infty}^{\infty} d\tau e^{-j\xi\tau}\frac{m_t}{D_\nu} \\
&\quad (\pm\frac{k_z}{k_\rho}(1+\frac{\tau}{2m_t^2})P_m^z + (1+\frac{j\Lambda^{-1}k}{k_\rho}R_\nu)P_m^\phi]\frac{H_\nu^{(2)}(k_\rho\rho)}{H_\nu^{(2)}(k_\rho a)} \qquad \text{(C.38)} \\
F_{z_\ell}^{\pm} &= \frac{j}{4\pi^2 a\Lambda k}\int_{-\infty}^{\infty} dk_z e^{-j(k_z z_d + k_\rho a\phi_\ell^{\pm})}\int_{-\infty}^{\infty} d\tau e^{-j\xi\tau}\frac{m_t}{D_\nu} \\
&\quad [(1+\frac{j\Lambda k}{k_\rho}R_\nu)P_m^z \mp \frac{k_z}{k_\rho}(1+\frac{\tau}{2m_t^2})P_m^\phi]\frac{H_\nu^{(2)}(k_\rho\rho)}{H_\nu^{(2)}(k_\rho a)}. \qquad \text{(C.39)}
\end{aligned}$$

Then, introducing standard polar transformations

$$k_\rho = k\cos\psi\ , \quad k_z = k\sin\psi, \qquad \text{(C.40)}$$

along with the geometrical relations (see Fig. 2.1)

$$a\phi_\ell^{\pm} = s\cos\alpha\ , \quad z_d = s\sin\alpha, \qquad \text{(C.41)}$$

integration over k_z is converted to a complex contour integral C_ψ, as shown in Fig. C.1. The relevant vector potential expressions to find the surface magnetic field are given by

$$\begin{aligned}
\left.\frac{\partial A_{z_\ell}^{\pm}}{\partial\rho}\right|_{\rho=a} &= -\frac{jk}{4\pi^2 a Z_0}\int_{C_\psi} d\psi e^{-jks\cos(\psi-\alpha)}\int_{-\infty}^{\infty} d\tau e^{-j\xi\tau}\frac{m_t}{D_\nu} \\
&\quad \cos\psi[\pm\sin\psi(1+\frac{\tau}{2m_t^2})P_m^z + (\cos\psi + j\Lambda^{-1}R_\nu)P_m^\phi]R_\nu \qquad \text{(C.42)} \\
\left.F_{z_\ell}^{\pm}\right|_{\rho=a} &= \frac{j}{4\pi^2 a\Lambda}\int_{C_\psi} d\psi e^{-jks\cos(\psi-\alpha)}\int_{-\infty}^{\infty} d\tau e^{-j\xi\tau}\frac{m_t}{D_\nu} \\
&\quad [(\cos\psi + j\Lambda R_\nu)P_m^z \mp \sin\psi(1+\frac{\tau}{2m_t^2})P_m^\phi] \qquad \text{(C.43)}
\end{aligned}$$

which are evaluated on the surface of cylinder ($\rho = a$).

Complex contour integral is evaluated by applying the method of steepest descent path (see Fig. C.1) assuming that the separation s between the source and field points is the large parameter, resulting

$$\begin{aligned}
\left.\frac{\partial A^{\pm}_{z_\ell}}{\partial \rho}\right|_{\rho=a} &\sim -\frac{jk}{2\pi Z_0}\frac{e^{-jks}}{s}\cos\alpha\sqrt{\frac{j\xi}{4\pi}}\int_{-\infty}^{\infty} d\tau e^{-j\xi\tau}\frac{1}{m_t D_\nu} \\
&\quad [\pm\sin\alpha(1+\frac{\tau}{2m_t^2})P^z_m + (\cos\alpha + j\Lambda^{-1}R_\nu)P^\phi_m]R_\nu \qquad \text{(C.44)} \\
\left. F^{\pm}_{z_\ell}\right|_{\rho=a} &\sim \frac{j}{2\pi\Lambda}\frac{e^{-jks}}{s}\sqrt{\frac{j\xi}{4\pi}}\int_{-\infty}^{\infty} d\tau e^{-j\xi\tau}\frac{1}{m_t D_\nu} \\
&\quad [(\cos\alpha + j\Lambda R_\nu)P^z_m \mp \sin\alpha(1+\frac{\tau}{2m_t^2})P^\phi_m]. \qquad \text{(C.45)}
\end{aligned}$$

Similar to the PEC cylinder case, the field expressions are obtained by performing the derivatives to the resultant potential expressions analytically using (C.23). Finally, the UTD-based asymptotic Green's function representations that give the tangential surface magnetic field components for a tangential magnetic source on an impedance cylinder can be written as

$$\begin{aligned}
G^{\ell\pm}_{zz} &\sim G_0\Bigg\{\cos^2\alpha V_0 + \frac{j}{ks}\left(1-\frac{j}{ks}\right)(2-3\cos^2\alpha)V_0 \\
&\quad -\frac{j2}{k}\left(1-\frac{j}{ks}\right)\sin\alpha\frac{\partial V_0}{\partial z_d} + \frac{1}{k^2}\frac{\partial^2 V_0}{\partial z_d^2}\Bigg\} \qquad \text{(C.46)} \\
G^{\ell\pm}_{z\phi} &\sim \mp G_0\Bigg\{\cos\alpha\sin\alpha\left[1-\frac{j3}{ks}\left(1-\frac{j}{ks}\right)\right]Y_0 \\
&\quad -\frac{j2}{k}\left(\tan^2\alpha + \frac{j}{ks}\right)\cos\alpha\frac{\partial Y_0}{\partial z_d} + \frac{\tan\alpha}{k^2}\frac{\partial^2 Y_0}{\partial z_d^2}\Bigg\} \qquad \text{(C.47)} \\
G^{\ell\pm}_{\phi z} &\sim \mp G_0\Bigg\{\cos\alpha\sin\alpha\left[X_0 + V_0 - \frac{j3}{ks}(1-\frac{j}{ks})V_0\right] \\
&\quad +\frac{j}{k}\left(1-\frac{j}{ks}\right)\left(\cos\alpha\frac{\partial V_0}{\partial z_d} + \sin\alpha\frac{\partial V_0}{\partial y_\ell}\right) - \frac{1}{k^2}\frac{\partial^2 V_0}{\partial y_\ell \partial z_d}\Bigg\} \qquad \text{(C.48)} \\
G^{\pm}_{\phi\phi} &\sim G_0\Bigg\{\sin^2\alpha Y_0 + \frac{j}{ks}\left(1-\frac{j}{ks}\right)(2-3\sin^2\alpha)Y_0 + \frac{j}{ks}\frac{1}{\cos^2\alpha}(U_0 - Y_0) \\
&\quad +\frac{j}{k}\left(1-\frac{j}{ks}\right)\left(\sin\alpha\frac{\partial Y_0}{\partial z_d} - \cos\alpha\frac{\partial Y_0}{\partial y_\ell}\right) \\
&\quad +\frac{j}{k\cos\alpha}\left(\frac{\partial Y_0}{\partial y_\ell} - \frac{j}{ks}\tan\alpha\frac{\partial Y_0}{\partial z_d}\right) - \frac{\tan\alpha}{k^2}\frac{\partial^2 Y_0}{\partial y_\ell \partial z_d}\Bigg\}. \qquad \text{(C.49)}
\end{aligned}$$

In (C.46)-(C.49), the U_0, X_0, V_0 and Y_0 terms are expressed in [19] in terms of simpler Fock type integrals in the form of

$$\Upsilon_r = \int_{-\infty}^{\infty} d\tau e^{-j\xi\tau} \frac{(R_w)^r}{D_w} \quad ; \qquad r = 0, 1, 2 \tag{C.50}$$

where

$$D_w = (R_w - q_e)(R_w - q_m) + q_c^2 \tag{C.51}$$

$$q_e = -jm_t \Lambda \cos\alpha \tag{C.52}$$

$$q_m = -jm_t \Lambda^{-1} \cos\alpha \tag{C.53}$$

$$q_c = -jm_t (1 + \frac{\tau}{2m_t^2}) \sin\alpha \tag{C.54}$$

$$R_w = W_2'(\tau)/W_2(\tau) \tag{C.55}$$

in which $W_2(\tau)$ is a Fock-type Airy function, $W_2'(\tau)$ is its derivative with respect to τ. Besides, $\Lambda = Z_s/Z_0$ is the normalized surface impedance, and the Fock parameter is

$$\xi = m_t \phi_\ell^{\pm} \tag{C.56}$$

with

$$m_t = (\frac{k_\rho a}{2})^{1/3}. \tag{C.57}$$

The simplified equations are, in turn, given in [19] as follows:

$$U_0 = -j\xi q_m \sqrt{\frac{j\xi}{\pi}} (\Upsilon_2 - q_e \Upsilon_1) \tag{C.58}$$

$$X_0 = -\frac{1}{2} \sqrt{\frac{j\xi}{\pi}} (\Upsilon_1 + \frac{j}{2m_t^2} \frac{\partial \Upsilon_1}{\partial \xi}) \tag{C.59}$$

$$V_0 = \frac{1}{2} \sqrt{\frac{j\xi}{\pi}} (\Upsilon_1 - q_m \Upsilon_0) \tag{C.60}$$

$$Y_0 = -\frac{q_m}{2} \sqrt{\frac{j\xi}{\pi}} (\Upsilon_0 + \frac{j}{2m_t^2} \frac{\partial \Upsilon_0}{\partial \xi}) \tag{C.61}$$

The derivatives of Fock type integrals in (C.46)-(C.49) are written in [19] as (the terms including higher powers of m_t^{-2} are neglected))

$$\frac{\partial V_0}{\partial z_d} \sim -\frac{\sin\alpha}{6s} V_1 \tag{C.62}$$

$$\frac{\partial Y_0}{\partial z_d} \sim -\frac{\sin\alpha}{6s} Y_1 \tag{C.63}$$

$$\frac{\partial V_0}{\partial y_\ell} \sim -\frac{1}{6s}\left(\cos\alpha - \frac{4}{\cos\alpha}\right) V_1 \tag{C.64}$$

$$\frac{\partial Y_0}{\partial y_\ell} \sim -\frac{1}{6s}\left(\cos\alpha - \frac{4}{\cos\alpha}\right) Y_1 \tag{C.65}$$

$$\frac{\partial^2 V_0}{\partial z_d^2} \sim \frac{\sin^2\alpha}{36s^2} V_2 - \frac{\cos 2\alpha}{6s^2} V_1 \tag{C.66}$$

$$\frac{\partial^2 Y_0}{\partial z_d^2} \sim \frac{\sin^2\alpha}{36s^2} Y_2 - \frac{\cos 2\alpha}{6s^2} Y_1 \tag{C.67}$$

$$\frac{\partial^2 V_0}{\partial y_\ell \partial z_d} \sim \frac{\sin\alpha}{36s^2}\left(\cos\alpha - \frac{4}{\cos\alpha}\right) V_2 + \frac{\sin 2\alpha}{6s^2} V_1 \tag{C.68}$$

$$\frac{\partial^2 Y_0}{\partial y_\ell \partial z_d} \sim \frac{\sin\alpha}{36s^2}\left(\cos\alpha - \frac{4}{\cos\alpha}\right) Y_2 + \frac{\sin 2\alpha}{6s^2} Y_1 \tag{C.69}$$

where

$$V_1 = \frac{1}{2}\sqrt{\frac{j\xi}{\pi}}[\Upsilon_1 - q_m\Upsilon_0 + 2\xi(\frac{\partial\Upsilon_1}{\partial\xi} - q_m\frac{\partial\Upsilon_0}{\partial\xi})] \tag{C.70}$$

$$Y_1 = -\frac{q_m}{2}\sqrt{\frac{j\xi}{\pi}}[\Upsilon_0 + (\frac{j}{2m_t^2} + 2\xi)\frac{\partial\Upsilon_0}{\partial\xi}] \tag{C.71}$$

$$V_2 = \frac{1}{2}\sqrt{\frac{j\xi}{\pi}}[3(\Upsilon_1 - q_m\Upsilon_0) + 8\xi(\frac{\partial\Upsilon_1}{\partial\xi} - q_m\frac{\partial\Upsilon_0}{\partial\xi})] \tag{C.72}$$

$$Y_2 = -\frac{q_m}{2}\sqrt{\frac{j\xi}{\pi}}[3\Upsilon_0 + (\frac{j3}{2m_t^2} + 8\xi)\frac{\partial\Upsilon_0}{\partial\xi}]. \tag{C.73}$$

Appendix D

Derivation of asymptotic solution pertaining to the sphere

D.1 PEC Sphere

The free-space potentials (in the absence of the sphere) are given in (B.39)-(B.40) in Appendix B.2. The scattered fields due to the presence of the PEC sphere are in similar form to those of incident fields (i.e., in the form of an infinite sum of spherical wave functions) except some complex coefficients to be found from the appropriate boundary conditions as also explained in Appendix B. Thus, defining another set of potentials to account for the scattering from the PEC sphere, and superposing them with the free-space potentials defined in (B.39)-(B.40), the total potentials are given by

$$\begin{aligned}\psi^e &= \left(\frac{kp_m}{4\pi j}\right)\left(\frac{jY_0\sin\phi}{kb}\right)\sum_{n=1}^{\infty}\frac{2n+1}{n(n+1)}\hat{H}_n^{(2)}(kb) \\ &\quad \left(\hat{J}_n(kr)+C_{1n}\hat{H}_n^{(2)}(kr)\right)P_n^1(\cos\theta) \qquad \text{(D.1)}\\ \psi^m &= \left(\frac{kp_m}{4\pi j}\right)\left(\frac{-\cos\phi}{kb}\right)\sum_{n=1}^{\infty}\frac{2n+1}{n(n+1)}\hat{H}_n^{(2)\prime}(kb) \\ &\quad \left(\hat{J}_n(kr)+C_{2n}\hat{H}_n^{(2)}(kr)\right)P_n^1(\cos\theta). \qquad \text{(D.2)}\end{aligned}$$

Complex coefficients, C_{1n} and C_{2n}, in (D.1) and (D.2) are found by applying the boundary conditions at $r = a$ (tangential electric fields are zero). Then, the exact expressions for ψ^e and ψ^m can be found as

$$\begin{aligned} \psi^e &= \left(\frac{kp_m}{4\pi j}\right)\left(\frac{jY_0 \sin\phi}{kb}\right)\sum_{n=1}^{\infty}\frac{2n+1}{n(n+1)}\hat{H}_n^{(2)}(kb)\tilde{A}_n(kr)P_n^1(\cos\theta) && \text{(D.3)} \\ \psi^m &= \left(\frac{kp_m}{4\pi j}\right)\left(\frac{-\cos\phi}{kb}\right)\sum_{n=1}^{\infty}\frac{2n+1}{n(n+1)}\hat{H}_n^{(2)\prime}(kb)\tilde{B}_n(kr)P_n^1(\cos\theta) && \text{(D.4)} \end{aligned}$$

where

$$\begin{aligned} \tilde{A}_n(kr) &= \hat{J}_n(kr) - \frac{\hat{J}_n(ka)}{\hat{H}_n^{(2)}(ka)}\hat{H}_n^{(2)}(kr) && \text{(D.5)} \\ \tilde{B}_n(kr) &= \hat{J}_n(kr) - \frac{\hat{J}_n'(ka)}{\hat{H}_n^{(2)\prime}(ka)}\hat{H}_n^{(2)}(kr). && \text{(D.6)} \end{aligned}$$

The first step of the high frequency development of the surface fields on a PEC sphere is to apply Watson's transformation [50] to convert the very slowly convergent infinite summations in (D.3)-(D.4) to a contour integral $C_\nu^\pm$, as shown in Fig.D.1. Thus, the new expression for the potentials are given by

$$\begin{aligned} \left\{\begin{array}{c} \psi^e \\ \psi^m \end{array}\right\} &= \frac{kp_m}{4\pi j}\frac{1}{kb}\left\{\begin{array}{c} jY_0 \sin\phi \\ -\cos\phi \end{array}\right\}\frac{1}{2\pi j}\oint_{C_\nu^+ + C_\nu^-} d\nu \frac{2\nu+1}{\nu(\nu+1)}\frac{\pi(-1)^\nu}{\sin(\nu\pi)} \\ & \quad \hat{H}_\nu^{(2)}(kb)\left\{\begin{array}{c} \tilde{A}_\nu(kr) \\ \tilde{B}_\nu(kr) \end{array}\right\}P_\nu^1(\cos\theta). && \text{(D.7)} \end{aligned}$$

Then, as suggested in [10], using the relation ([47])

$$(-1)^\nu P_\nu^1(\cos\theta) = \nu(\nu+1)P_\nu^{-1}(-\cos\theta) \tag{D.8}$$

and then replacing ν by $-\nu - 1$ in the integration over C_ν^+, the potentials are obtained as

$$\begin{aligned} \left\{\begin{array}{c} \psi^e \\ \psi^m \end{array}\right\} &= \frac{kp_m}{4\pi j}\frac{1}{kb}\left\{\begin{array}{c} jY_0 \sin\phi \\ -\cos\phi \end{array}\right\}\frac{1}{2\pi j}\int_{-\infty-j\xi}^{\infty-j\xi} d\nu \frac{\pi}{\sin(\nu\pi)}(2\nu+1) \\ & \quad \hat{H}_\nu^{(2)}(kb)\left\{\begin{array}{c} \tilde{A}_\nu(kr) \\ \tilde{B}_\nu(kr) \end{array}\right\}P_\nu^{-1}(-\cos\theta) && \text{(D.9)} \end{aligned}$$

in which the integration is over the new contour $\tilde{C}_\nu = \tilde{C}_\nu^+ + C_\nu^-$.

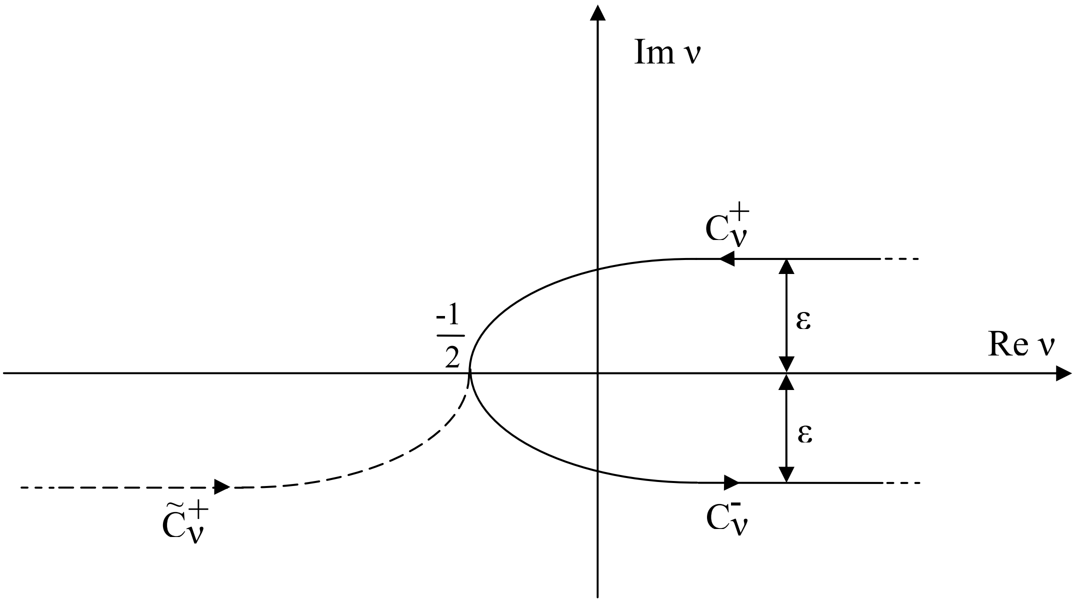

Figure D.1: Contour of integration in the complex ν plane. $C_\nu = C_\nu^+ + C_\nu^-$ is the original contour and $\tilde{C}_\nu = \tilde{C}_\nu^+ + C_\nu^-$ is the new contour.

As the next step, the potentials ψ^e and ψ^m are evaluated at $r = r' = a$, and the integration variable is changed from ν to μ via $\mu = \nu + 1/2$. Then, the substitution originally suggested by [24]

$$\mu = ka + m\tau \qquad ; \qquad m = \left(\frac{ka}{2}\right)^{1/3} \tag{D.10}$$

is made, and the series expansion of $\frac{1}{sin[(\mu-1/2)\pi]}$ given by

$$\frac{1}{sin[(\mu - 1/2)\pi]} = 2je^{-j(\mu-1/2)\pi} \sum_{\ell=0}^{\infty} e^{-j(\mu-1/2)(2\pi\ell)} \tag{D.11}$$

is employed where only the $\ell = 0$ term is retained since $\ell \neq 0$ terms correspond to multiple encirclements around the sphere and are negligible for large ka. Finally, replacing the cylindrical Hankel and Bessel functions [i.e., $\hat{J}_{\mu-1/2}(ka)$, $\hat{H}^{(2)}_{\mu-1/2}(ka)$] along with their derivatives by Fock type Airy functions and their derivatives, and approximating the Legendre polynomial $P^{-1}_{\mu-1/2}(-\cos\theta)$ by [47]

$$P^{-1}_{\mu-1/2}(-\cos\theta) \sim -\frac{\mu^{-3/2}}{2j}\sqrt{\frac{2}{\pi\sin\theta}}e^{-j\pi/4}e^{j\mu\pi}\left[e^{-j\mu\theta} - je^{-j\mu(2\pi-\theta)}\right] \tag{D.12}$$

ψ^e can be obtained as

$$\begin{aligned}\psi^e \quad \sim \quad & \left(\frac{kp_m}{4\pi j}\right)\left(\frac{-jY_0 \sin\phi}{ka}\right)\sqrt{\frac{2}{\pi \sin\theta}}e^{-j\pi/4}jm\int_{-\infty}^{\infty} d\mu\mu^{-1/2} \\ & \left[\frac{1}{R_w(\tau)}\right]\left[e^{-j\mu\theta} - je^{-j\mu(2\pi-\theta)}\right] \end{aligned} \tag{D.13}$$

where

$$R_w(\tau) = \frac{W_2'(\tau)}{W_2(\tau)}. \tag{D.14}$$

Then, using the definitions made by [10]:

$$\xi^{\pm} = m\theta^{\pm} = m\left\{\begin{array}{c}\theta \\ 2\pi - \theta\end{array}\right\} \tag{D.15}$$

$$s^{\pm} = a\left\{\begin{array}{c}\theta \\ 2\pi - \theta\end{array}\right\} \tag{D.16}$$

and making use of the following approximation for large ka

$$\int d\mu\mu^{-1/2} \sim \frac{m}{\sqrt{ka}}\int d\tau, \tag{D.17}$$

the final form of ψ^e is written in the form of $\psi^e_{\pm}$ as

$$\psi^e_{\pm} \sim \pm\frac{jp_m}{k}V(\xi^{\pm})\sin\phi D^{\pm}G_0 \tag{D.18}$$

where

$$G_0 = \frac{k^2 Y_0}{2\pi j}\frac{e^{-jks^{\pm}}}{ks^{\pm}} \tag{D.19}$$

$$D^{\pm} = \sqrt{\frac{\theta^{\pm}}{\sin\theta^{\pm}}} \tag{D.20}$$

$$V(\xi^{\pm}) = \sqrt{\frac{j\xi^{\pm}}{4\pi}}\int_{-\infty}^{\infty}\frac{1}{R_w}e^{-j\xi^{\pm}\tau}d\tau. \tag{D.21}$$

Because the tangential magnetic field components H_θ and H_ϕ contain the derivative of ψ^m with respect to r, as seen in (B.45) and (B.52), the Fock substitution is employed as (see Fig. B.1)

$$\mu = ka + m\tau = k(r - d_2) + m\tau = kr + m(\tau - m^{-1}kd_2) = kr + m(\tau - y_2) \tag{D.22}$$

where $y_2 = m^{-1}kd_2$, and the evaluation at $r = a$ $(i.e., d_2 = 0)$ is performed after performing the derivatives with respect to r. Thus, performing the same definitions and approximation as done for ψ^e case, ψ^m is written as

$$\begin{aligned}
\psi^m_\pm \quad \sim \quad & \pm\frac{-p_m e^{-j\pi/4}}{4kmY_0}\cos\phi D^\pm G_0\sqrt{\frac{\xi^\pm}{\pi}}\int_{-\infty}^{\infty} d\tau e^{-j\xi^\pm\tau} \\
& \frac{W_2'(\tau)}{-mW_2(\tau)+j\Lambda W_2'(\tau)}\Big\{W_1(\tau-y_2)[-mW_2(\tau)+j\Lambda W_2'(\tau)] \\
& +W_2(\tau-y_2)[mW_1(\tau)-j\Lambda W_1'(\tau)]\Big\}
\end{aligned} \tag{D.23}$$

before the derivatives are performed.

The final expressions for tangential magnetic field components, H_θ and H_ϕ, are found as ($\pm$ is dropped from s and ξ for convenience)

$$H_\theta^\pm \quad = \quad \pm p_m\cos\phi\left[\frac{j}{ks}(1-\frac{2j}{ks})U + D^2\frac{j}{ks}V\right]DG_0 \tag{D.24}$$

$$H_\phi^\pm \quad = \quad \mp p_m\sin\phi\left[(1-\frac{j}{ks})V - D^2\frac{U}{(ks)^2}\right]DG_0 \tag{D.25}$$

where

$$U = j\xi\sqrt{\frac{j\xi}{\pi}}\int_{-\infty}^{\infty} d\tau e^{-j\xi\tau}\frac{W_2'(\tau)}{W_2(\tau)}. \tag{D.26}$$

D.2 Impedance Sphere

The exact expressions for ψ^e and ψ^m are found in Appedix B.2 as

$$\psi^e \quad = \quad \left(\frac{kp_m}{4\pi j}\right)\left(\frac{jY_0\sin\phi}{kb}\right)\sum_{n=1}^{\infty}\frac{2n+1}{n(n+1)}\hat{H}_n^{(2)}(kb)\tilde{A}_n(kr)P_n^1(\cos\theta) \tag{D.27}$$

$$\psi^m \quad = \quad \left(\frac{kp_m}{4\pi j}\right)\left(\frac{-\cos\phi}{kb}\right)\sum_{n=1}^{\infty}\frac{2n+1}{n(n+1)}\hat{H}_n^{(2)'}(kb)\tilde{B}_n(kr)P_n^1(\cos\theta) \tag{D.28}$$

where

$$\tilde{A}_n(kr) \quad = \quad \hat{J}_n(kr) - \frac{\hat{J}_n(ka)+j\Lambda^{-1}\hat{J}_n'(ka)}{\hat{H}_n^{(2)}(ka)+j\Lambda^{-1}\hat{H}_n^{(2)'}(ka)}\hat{H}_n^{(2)}(kr) \tag{D.29}$$

$$\tilde{B}_n(kr) \quad = \quad \hat{J}_n(kr) - \frac{\hat{J}_n(ka)+j\Lambda\hat{J}_n'(ka)}{\hat{H}_n^{(2)}(ka)+j\Lambda\hat{H}_n^{(2)'}(ka)}\hat{H}_n^{(2)}(kr). \tag{D.30}$$

At this stage, one can find the exact expression for the field components from the potentials ψ^e and ψ^m that involve infinite summations, and then find the high frequency based asymptotic expressions for these field components. However, we prefer to use the same procedure developed in [10] for PEC cylinder and sphere as explained in Appendix D.1. Briefly, it is a two-step procedure where the leading term $[O(1/ks)]$ of the high frequency based expressions for the potentials (ψ^e and ψ^m in this study) are first developed, and the fields are then obtained by taking the necessary derivatives. However, unlike [10] some higher order terms and derivatives of Fock type integrals are retained as they may be important for some Z_s values for some separations between the source and observation points. A similar procedure has been presented in [20] to find the UTD based solution for the surface fields on an impedance cylinder.

Similar to the PEC sphere case, the first step of the high frequency development of the surface fields on an impedance sphere is to apply Watson's transformation [50] to convert the very slowly convergent infinite summations in (D.27)-(D.28) to a contour integral $C_\nu^\pm$, as shown in Fig.D.1. Thus, the new expression for the potentials are given by

$$\begin{aligned}\left\{\begin{array}{c}\psi^e\\ \psi^m\end{array}\right\} &= \frac{kp_m}{4\pi j}\frac{1}{kb}\left\{\begin{array}{c}jY_0\sin\phi\\ -\cos\phi\end{array}\right\}\frac{1}{2\pi j}\oint_{C_\nu^+ + C_\nu^-} d\nu\frac{2\nu+1}{\nu(\nu+1)}\frac{\pi(-1)^\nu}{\sin(\nu\pi)}\\ &\quad \hat{H}_\nu^{(2)}(kb)\left\{\begin{array}{c}\tilde{A}_\nu(kr)\\ \tilde{B}_\nu(kr)\end{array}\right\}P_\nu^1(\cos\theta). \qquad (D.31)\end{aligned}$$

Then, as suggested by [10], using the relation ([47])

$$(-1)^\nu P_\nu^1(\cos\theta) = \nu(\nu+1)P_\nu^{-1}(-\cos\theta) \qquad (D.32)$$

and then replacing ν by $-\nu-1$ in the integration over C_ν^+, the potentials are obtained as

$$\begin{aligned}\left\{\begin{array}{c}\psi^e\\ \psi^m\end{array}\right\} &= \frac{kp_m}{4\pi j}\frac{1}{kb}\left\{\begin{array}{c}jY_0\sin\phi\\ -\cos\phi\end{array}\right\}\frac{1}{2\pi j}\int_{-\infty-j\xi}^{\infty-j\xi} d\nu\frac{\pi}{\sin(\nu\pi)}(2\nu+1)\\ &\quad \hat{H}_\nu^{(2)}(kb)\left\{\begin{array}{c}\tilde{A}_\nu(kr)\\ \tilde{B}_\nu(kr)\end{array}\right\}P_\nu^{-1}(-\cos\theta). \qquad (D.33)\end{aligned}$$

Similar to the PEC case, the integration in (D.33) is to be evaluated on the new contour $\tilde{C}_\nu = \tilde{C}_\nu^+ + C_\nu^-$. As the next step, the potentials ψ^e and ψ^m are evaluated at $r = r' = a$, and the integration variable is changed from ν to μ via $\mu = \nu + 1/2$. Then, the substitution originally suggested by [24]

$$\mu = ka + m\tau \qquad ; \qquad m = \left(\frac{ka}{2}\right)^{1/3} \tag{D.34}$$

is made, and the series expansion of $\frac{1}{sin[(\mu-1/2)\pi]}$ given by

$$\frac{1}{sin[(\mu - 1/2)\pi]} = 2je^{-j(\mu-1/2)\pi}\sum_{\ell=0}^{\infty} e^{-j(\mu-1/2)(2\pi\ell)} \tag{D.35}$$

is employed where only the $\ell = 0$ term is retained since $\ell \neq 0$ terms correspond to multiple encirclements around the sphere and are negligible for large ka. Finally, replacing the cylindrical Hankel and Bessel functions [i.e., $\hat{J}_{\mu-1/2}(ka)$, $\hat{H}^{(2)}_{\mu-1/2}(ka)$] along with their derivatives by Fock type Airy functions and their derivatives, and approximating the Legendre polynomial $P^{-1}_{\mu-1/2}(-\cos\theta)$ by [47]

$$P^{-1}_{\mu-1/2}(-\cos\theta) \sim -\frac{\mu^{-3/2}}{2j}\sqrt{\frac{2}{\pi\sin\theta}}e^{-j\pi/4}e^{j\mu\pi}\left[e^{-j\mu\theta} - je^{-j\mu(2\pi-\theta)}\right] \tag{D.36}$$

ψ^e can be obtained as

$$\begin{aligned}\psi^e \sim & \left(\frac{kp_m}{4\pi j}\right)\left(\frac{-jY_0\sin\phi}{ka}\right)\sqrt{\frac{2}{\pi\sin\theta}}e^{-j\pi/4}jm\int_{-\infty}^{\infty} d\mu\mu^{-1/2} \\ & \left[\frac{1}{R_w(\tau) + jm\Lambda}\right]\left[e^{-j\mu\theta} - je^{-j\mu(2\pi-\theta)}\right]\end{aligned} \tag{D.37}$$

where

$$R_w(\tau) = \frac{W_2'(\tau)}{W_2(\tau)}. \tag{D.38}$$

Note that ψ^e can be written as ψ^e_+ and ψ^e_- where ψ^e_+ is associated with $e^{-j\mu\theta}$ term; and ψ^e_- is associated with $e^{-j\mu(2\pi-\theta)}$ term [10]. Then, using the definitions made by [10]:

$$\xi^{\pm} = m\theta^{\pm} = m\left\{\begin{array}{c}\theta \\ 2\pi-\theta\end{array}\right\} \tag{D.39}$$

$$s^{\pm} = a\left\{\begin{array}{c}\theta \\ 2\pi-\theta\end{array}\right\} \tag{D.40}$$

and making use of the following approximation for large ka

$$\int d\mu\mu^{-1/2} \sim \frac{m}{\sqrt{ka}}\int d\tau, \tag{D.41}$$

the final form of ψ^e is written in the form of $\psi^e_\pm$ as

$$\psi^e_\pm \sim \pm\frac{jp_m}{k}V_z(\xi^\pm)\sin\phi D^\pm G_0 \tag{D.42}$$

where

$$G_0 = \frac{k^2Y_0}{2\pi j}\frac{e^{-jks^\pm}}{ks^\pm} \tag{D.43}$$

$$D^\pm = \sqrt{\frac{\theta^\pm}{\sin\theta^\pm}} \tag{D.44}$$

$$V_z(\xi^\pm) = \sqrt{\frac{j\xi^\pm}{4\pi}}\int_{-\infty}^{\infty}\frac{1}{R_w - q_e}e^{-j\xi^\pm\tau}d\tau \tag{D.45}$$

with $q_e = -jm\Lambda$. Notice that (D.42)-(D.45) are exactly in the same form as that of the PEC case [(D.18)-(D.21)] except the integrand of (D.45). Also note that in (D.42)-(D.45), (+) corresponds to the field propagation along the geodesic ray path corresponding to $s^+ = a\theta^+$ whereas (-) corresponds to the field propagation along the same geodesic ray path but in a direction opposite to s^+ corresponding to $s^- = a\theta^- = a(2\pi - \theta^+)$.

Because the tangential magnetic field components H_θ and H_ϕ contain the derivative of ψ^m with respect to r, as seen in (B.45) and (B.52), the Fock substitution is employed as

$$\mu = ka + m\tau = k(r - d_2) + m\tau = kr + m(\tau - m^{-1}kd_2) = kr + m(\tau - y_2) \tag{D.46}$$

where $y_2 = m^{-1}kd_2$ and the evaluation at $r = a$ $(i.e., d_2 = 0)$ is performed after performing the derivatives with respect to r. Thus, performing the same definitions and approximation as done for ψ^e case, ψ^m is written as

$$\begin{aligned}\psi^m_\pm \sim\ & \pm\frac{-p_m e^{-j\pi/4}}{4kmY_0}\cos\phi D^\pm G_0\sqrt{\frac{\xi^\pm}{\pi}}\int_{-\infty}^{\infty}d\tau e^{-j\xi^\pm\tau} \\ & \frac{W_2'(\tau)}{-mW_2(\tau) + j\Lambda W_2'(\tau)}\Big\{W_1(\tau - y_2)[-mW_2(\tau) + j\Lambda W_2'(\tau)] \\ & +W_2(\tau - y_2)[mW_1(\tau) - j\Lambda W_1'(\tau)]\Big\},\end{aligned} \tag{D.47}$$

before the derivatives are performed. Then, the derivative of ψ^m with respect to

r is evaluated as follows ($\pm$ is dropped for convenience):

$$\begin{aligned}
\left.\frac{\partial}{\partial r}\psi^m\right|_{r=a} &= \frac{-p_m e^{-j\pi/4}}{4kmY_0}\cos\phi D G_0\sqrt{\frac{\xi}{\pi}}\left(\frac{-k}{m}\right)\int_{-\infty}^{\infty} d\tau e^{-j\xi\tau} \\
&\quad \frac{W_2'(\tau)}{-mW_2(\tau)+j\Lambda W_2'(\tau)}\Big\{W_1'(\tau)[-mW_2(\tau)+j\Lambda W_2'(\tau)] \\
&\quad +W_2'(\tau)[mW_1(\tau)-j\Lambda W_1'(\tau)]\Big\} \\
&= \frac{-p_m e^{-j\pi/4}}{2m^2Y_0}\cos\phi D G_0\sqrt{\frac{\xi}{\pi}}\int_{-\infty}^{\infty} d\tau e^{-j\xi\tau}\frac{jmW_2'(\tau)}{-mW_2(\tau)+j\Lambda W_2'(\tau)} \\
&= \frac{-jp_m}{2\xi m^2Y_0}\cos\phi D G_0 e^{j3\pi/4}\frac{\xi^{3/2}}{\sqrt{\pi}}\int_{-\infty}^{\infty} d\tau e^{-j\xi\tau}\frac{-R_w(\tau)q_m}{R_w(\tau)-q_m} \\
&= \frac{-jp_m}{2\xi m^2Y_0}U_z\xi\cos\phi D G_0 \qquad \text{(D.48)}
\end{aligned}$$

where

$$U_z(\xi) = e^{j3\pi/4}\xi^{3/2}\frac{1}{\sqrt{\pi}}\int_{-\infty}^{\infty} d\tau e^{-j\xi\tau}\frac{-R_w q_m}{(R_w-q_m)} \qquad \text{(D.49)}$$

in which $q_m = -jm\Lambda^{-1}$. On the other hand, the derivative of $G(ks)$ with respect to θ is given by

$$\begin{aligned}
\frac{\partial}{\partial\theta}G_0 &= \frac{k^2Y_0}{2\pi j}\frac{\partial}{\partial\theta}\frac{e^{-jks}}{ks} = \frac{k^2Y_0}{2\pi j}a\frac{\partial}{\partial s}\frac{e^{-jks}}{ks} = ka(-j-\frac{1}{ks})\frac{k^2Y_0}{2\pi j}\frac{e^{-jks}}{ks} \\
&= 2m^3(-j-\frac{1}{ks})G_0 \qquad \text{(D.50)}
\end{aligned}$$

and using (B.45) and (B.52), the final expressions for the tangential magnetic field components, H_θ and H_ϕ, are found as

$$\begin{aligned}
H_\theta &= \frac{1}{a\sin\theta}\frac{\partial}{\partial\phi}\left(\frac{jp_m}{k}V_z(\xi)\sin\phi DG_0\right) \\
&\quad +\frac{1}{jkZ_0a}\frac{\partial}{\partial\theta}\left(\frac{-jp_m}{2\xi m^2Y_0}U_z(\xi)\cos\phi DG_0\right) \\
&= \frac{jp_m}{ka\sin\theta}V_z(\xi)\cos\phi DG_0-\frac{p_m\cos\phi}{2kam^2}\left(\frac{1}{\xi}DU_z(\xi)\frac{\partial G_0}{\partial\theta}\right. \\
&\quad \left.+DU_z(\xi)G_0\frac{\partial}{\partial\theta}\left(\frac{1}{\xi}\right)+G_0\frac{1}{\xi}\frac{\partial}{\partial\theta}\left[DU_z(\xi)\right]\right) \\
&= p_m\cos\phi\frac{j}{ks}V_z(\xi)D^3G_0-\frac{p_m\cos\phi}{2kam^2}\left(DG_0U_z(\xi)\frac{2m^3}{\xi}\left(-j-\frac{1}{ks}\right)\right. \\
&\quad \left.+DG_0U_z(\xi)\frac{-1}{\xi\theta}+G_0\frac{1}{\xi}\frac{\partial}{\partial\theta}\left[DU_z(\xi)\right]\right) \\
&= p_m\cos\phi\left\{\left[\frac{j}{ks}V_z(\xi)D^2+U_z(\xi)\frac{j}{ks}\left(1-\frac{2j}{ks}\right)\right]DG_0\right. \\
&\quad \left.-G_0\frac{1}{4m^5\xi}\frac{\partial}{\partial\theta}\left[DU_z(\xi)\right]\right\} \qquad \text{(D.51)}
\end{aligned}$$

$$\begin{aligned}
H_\phi &= -\frac{1}{a}\frac{\partial}{\partial\theta}\left(\frac{jp_m}{k}V_z(\xi)\sin\phi DG_0\right)+\frac{1}{jkZ_0a\sin\theta} \\
&\quad \frac{\partial}{\partial\phi}\left(\frac{-jp_m}{2\xi m^2Y_0}U_z(\xi)\cos\phi DG_0\right) \\
&= -\frac{jp_m}{ka}\sin\phi\left(V_z(\xi)D\frac{\partial G_0}{\partial\theta}+G_0\frac{\partial}{\partial\theta}\left[DV_z(\xi)\right]\right) \\
&\quad +\frac{p_m\sin\phi}{2ka\sin\theta\xi m^2}G_0\frac{1}{\xi}DU_z \\
&= -p_m\sin\phi\left\{\left[\left(1-\frac{j}{ks}\right)V_z(\xi)+j^2D^2\frac{U_z(\xi)}{(ks)^2}\right]DG_0\right. \\
&\quad \left.+G_0\frac{j}{2m^3}\frac{\partial}{\partial\theta}\left[DV_z(\xi)\right]\right\}. \qquad \text{(D.52)}
\end{aligned}$$

Making the use of (D.51) together with the following expressions

$$\frac{\partial}{\partial\theta}D = \frac{m^3}{ks}D(1 - D^2\cos\theta), \tag{D.53}$$

$$\frac{\partial}{\partial\theta}U_z(\xi) = \frac{3m}{2\xi}U_z(\xi) + e^{j3\pi/4}\xi^{3/2}\frac{1}{\sqrt{\pi}}\int_{-\infty}^{\infty} d\tau(-jm\tau)e^{-j\xi\tau}\frac{-R_w q_m}{(R_w - q_m)}, \tag{D.54}$$

$$\tilde{U}_z(\xi) = e^{j3\pi/4}\xi^{3/2}\frac{1}{\sqrt{\pi}}\int_{-\infty}^{\infty} d\tau e^{-j\xi\tau}\frac{-R_w q_m}{(R_w - q_m)}\left(1 + \frac{\tau}{2m^2}\right), \tag{D.55}$$

H_θ can be written as

$$\begin{aligned}
H_\theta &= p_m\cos\phi\Bigg\{\left[\frac{j}{ks}V_z(\xi)D^2 + U_z(\xi)\frac{j}{ks}\left(1 - \frac{2j}{ks}\right)\right]DG_0 \\
&\quad -G_0 D U_z(\xi)\left[\frac{(1 - D^2\cos\theta)}{4m^2 ks\xi} + \frac{3}{8m^4\xi^2}\right] \\
&\quad -\frac{G_0 D}{4m^5\xi}e^{j3\pi/4}\xi^{3/2}\frac{1}{\sqrt{\pi}}\int_{-\infty}^{\infty} d\tau(-jm\tau)e^{-j\xi\tau}\frac{-R_w q_m}{(R_w - q_m)}\Bigg\} \\
&= p_m\cos\phi\Bigg[\frac{j}{ks}V_z(\xi)D^2 + U_z(\xi)\frac{j}{ks}\left(1 - \frac{2j}{ks}\right) + U_z(\xi)\Bigg(\frac{D^2\cos\theta}{2(ks)^2} \\
&\quad -\frac{2}{(ks)^2}\Bigg) + \frac{j}{ks}e^{j3\pi/4}\xi^{3/2}\frac{1}{\sqrt{\pi}}\int_{-\infty}^{\infty} d\tau\frac{\tau}{2m^2}e^{-j\xi\tau}\frac{-R_w q_m}{(R_w - q_m)}\Bigg]DG_0 \\
&= p_m\cos\phi\left[(\frac{j}{ks})\tilde{U}_z(\xi) - \frac{D^2}{2}(\frac{j}{ks})^2\cos\theta U_z(\xi) + D^2\frac{j}{ks^{\pm}}V_z(\xi)\right] \\
&\quad DG_0.
\end{aligned} \tag{D.56}$$

Similarly, using (D.52), (D.53) together with the following expressions

$$\frac{\partial}{\partial\theta}V_z(\xi) = \frac{m^3}{ks}V_z(\xi) + \sqrt{\frac{j\xi}{4\pi}}\int_{-\infty}^{\infty}\frac{1}{R_w - q_e}e^{-j\xi\tau}(-jm\tau)d\tau \tag{D.57}$$

$$\tilde{V}_z(\xi) = \sqrt{\frac{j\xi}{4\pi}}\int_{-\infty}^{\infty} d\tau e^{-j\xi\tau}\frac{1}{(R_w - q_e)}\left(1 + \frac{\tau}{2m^2}\right) \tag{D.58}$$

H_ϕ can be written as

$$
\begin{aligned}
H_\phi &= -p_m \sin\phi \Bigg\{ \Bigg[\Big(1 - \frac{j}{ks}\Big) V_z(\xi) + j^2 D^2 \frac{U_z(\xi)}{(ks)^2} \Bigg] D G_0 \\
&\quad + G_0 D V_z(\xi) \frac{j}{2m^3} \Bigg[\frac{m^3}{ks}(1 - D^2 \cos\theta) + \frac{m^3}{ks} \Bigg] \\
&\quad + \frac{j G_0 D}{2m^3} \sqrt{\frac{j\xi}{4\pi}} \int_{-\infty}^{\infty} d\tau e^{-j\xi\tau} \frac{1}{(R_w - q_e)} \Big(1 + \frac{\tau}{2m^2}\Big) \Bigg\} \\
&= -p_m \sin\phi \Bigg[\Big(1 - \frac{j}{ks}\Big) V_z(\xi) + j^2 D^2 \frac{U_z(\xi)}{(ks)^2} + V_z(\xi) \Big(\frac{j}{2ks} (1 \\
&\quad - D^2 \cos\theta) + \frac{j}{2ks} \Big) + \sqrt{\frac{j\xi}{4\pi}} \int_{-\infty}^{\infty} \frac{1}{R_w - q_e} e^{-j\xi\tau} \frac{\tau}{2m^2} d\tau \Bigg] D G_0 \\
&= p_m \sin\phi \Bigg[\tilde{V}_z(\xi) - \frac{D^2}{2} \frac{j}{ks} \cos\theta V_z(\xi) + D^2 (\frac{j}{ks})^2 U_z(\xi) \Bigg] D G_0. \qquad \text{(D.59)}
\end{aligned}
$$

In (D.56) and (D.59), V_z and U_z are the Fock type integrals given by

$$
\begin{aligned}
V_z &= \sqrt{\frac{j\xi}{4\pi}} \int_{-\infty}^{\infty} \frac{1}{R_w - q_e} e^{-j\xi\tau} d\tau \qquad \text{(D.60)} \\
U_z &= e^{j3\pi/4} \xi^{3/2} \frac{1}{\sqrt{\pi}} \int_{-\infty}^{\infty} d\tau e^{-j\xi\tau} \frac{-R_w q_m}{(R_w - q_m)}, \qquad \text{(D.61)}
\end{aligned}
$$

$\tilde{V}_z$ and $\tilde{U}_z$ include the derivatives of V_z and U_z, and are given by

$$
\begin{aligned}
\tilde{V}_z &= \sqrt{\frac{j\xi}{4\pi}} \int_{-\infty}^{\infty} d\tau e^{-j\xi\tau} \frac{1}{(R_w - q_e)} \Big(1 + \frac{\tau}{2m^2}\Big) \qquad \text{(D.62)} \\
\tilde{U}_z &= e^{j3\pi/4} \xi^{3/2} \frac{1}{\sqrt{\pi}} \int_{-\infty}^{\infty} d\tau e^{-j\xi\tau} \frac{-R_w q_m}{(R_w - q_m)} \Big(1 + \frac{\tau}{2m^2}\Big) \qquad \text{(D.63)}
\end{aligned}
$$

in which $q_m = -jm\Lambda^{-1}$, and $q_e = -jm\Lambda$ (as given before).

Appendix E

Calculation of geometrical and electrical parameters for UTD solution

An elementary differential geometry information, which is required for the calculation of geometrical and electrical parameters of the surfaces necessary for the UTD solution, is given in this Appendix.

A surface may be represented by a parametric equation

$$\vec{r}(u,v) = (x(u,v), y(u,v), z(u,v)) \tag{E.1}$$

where (u,v) is called the curvilinear coordinates. When $v = v_0$ (v is held constant), $\vec{r}(u,v_0)$ defines a curve on the surface, which is called $u-$parameter curve. When $u = u_0$ (u is held constant), $\vec{r}(u_0,v)$ defines a curve on the surface, which is called $v-$parameter curve.

Partial derivatives of $\vec{r}$ with respect to u, $\vec{r}_u = \frac{\partial \vec{r}}{\partial u}$, and with respect to v, $\vec{r}_v = \frac{\partial \vec{r}}{\partial v}$, give the tangent vectors along the $u-$ and $v-$parameter curves, respectively. The cross product of $\vec{r}_u$ and $\vec{r}_v$ is normal to the surface everywhere so the unit normal of the surface can be defined as

$$\hat{N} = \frac{\vec{r}_u \times \vec{r}_v}{|\vec{r}_u \times \vec{r}_v|}. \tag{E.2}$$

Curvature of a surface in $\hat{t}$ direction can be written as

$$k(\hat{t}) = \frac{II}{I} \tag{E.3}$$

where I and II are the first and second fundamental forms, respectively. I is the square of the differential arc length, $d\vec{r}$, along a curve on the surface such that

$$I = d\vec{r} \cdot d\vec{r} = (\vec{r}_u du + \vec{r}_v dv) \cdot (\vec{r}_u du + \vec{r}_v dv). \tag{E.4}$$

Alternatively, I can be written as

$$I = E(du)^2 + 2F du dv + G(dv)^2 \tag{E.5}$$

where

$$E = \vec{r}_u \cdot \vec{r}_u \ , \quad F = \vec{r}_u \cdot \vec{r}_v \ , \quad G = \vec{r}_v \cdot \vec{r}_v, \tag{E.6}$$

which are called the parameters of the first fundamental form. II is given as

$$II = d\vec{r} \cdot d\hat{N} = (\vec{r}_u du + \vec{r}_v dv) \cdot (\hat{N}_u du + \hat{N}_v dv). \tag{E.7}$$

Alternatively, II can be written as

$$II = e(du)^2 + 2f du dv + g(dv)^2 \tag{E.8}$$

where

$$e = -\vec{r}_u \cdot \hat{N}_u \ , \quad f = -(\vec{r}_u \cdot \hat{N}_v + \vec{r}_v \cdot \hat{N}_u) \ , \quad g = -\vec{r}_v \cdot \hat{N}_v, \tag{E.9}$$

which are called the parameters of the second fundamental form. More convenient formulas for e, f and g can be obtained by the differentiation of the identities $\vec{r}_u \cdot \hat{N} = 0$ and $\vec{r}_v \cdot \hat{N} = 0$ such that

$$\vec{r}_{uu} \cdot \hat{N} = -\vec{r}_u \cdot \hat{N}_u \tag{E.10}$$

$$\vec{r}_{uv} \cdot \hat{N} = -\vec{r}_u \cdot \hat{N}_v \tag{E.11}$$

$$\vec{r}_{vu} \cdot \hat{N} = -\vec{r}_v \cdot \hat{N}_u \tag{E.12}$$

$$\vec{r}_{vv} \cdot \hat{N} = -\vec{r}_v \cdot \hat{N}_v \tag{E.13}$$

where

$$\vec{r}_{uu} = \frac{\partial}{\partial u}\left(\frac{\partial \vec{r}}{\partial u}\right) \ , \quad \vec{r}_{uv} = \frac{\partial}{\partial u}\left(\frac{\partial \vec{r}}{\partial v}\right) \ , \quad \vec{r}_{vv} = \frac{\partial}{\partial v}\left(\frac{\partial \vec{r}}{\partial v}\right). \tag{E.14}$$

The directions where $k(\hat{t})$ is maximum and minimum are called the principal directions. Except the case where the curvature, which measures rate of turning [51], is constant in all directions, a curve on the surface is called line of curvature if it is tangent to a principal direction at all points. When $F = 0$ and $f = 0$, $u-$ and $v-$ parameter curves are themselves lines of curvature [51]. Thus, the principal curvatures along the u and v directions can be written as

$$\begin{aligned} k_u &= \frac{e}{E} && \text{(E.15)} \\ k_v &= \frac{g}{G}. && \text{(E.16)} \end{aligned}$$

The equation of the geodesic on a convex surface may be written as

$$\frac{dv}{du} = \frac{\pm h\sqrt{E}}{\sqrt{G}\sqrt{G - h^2}} \tag{E.17}$$

where h is a constant of integration, and is known as the first geodesic constant [14]. Integration of (E.17) results in

$$v = \int \frac{\pm h\sqrt{E}}{\sqrt{G}\sqrt{G - h^2}} du = f(u, h) + h' \tag{E.18}$$

where h' is called the second geodesic constant. h and h' are unique for the geodesic path between the source point, (u_s, v_s), and the observation point, (u_f, v_f). The first and the second geodesic constants are obtained by solving

$$\begin{aligned} v_s &= f(u_s, h) + h' && \text{(E.19)} \\ v_f &= f(u_f, h) + h'. && \text{(E.20)} \end{aligned}$$

Since finding $\delta(u)$, which is defined as the angle between the geodesic and the $u-$ parameter line, is trivial for singly curved surfaces, it is better to use

$$\cos\delta(u) = \frac{\sqrt{G - h^2}}{\sqrt{G}} \tag{E.21}$$

for the calculation of the first geodesic constant, h.

Surface ray torsion, which measures rate of twisting [51], is calculated using

$$\tau = (k_u - k_v)\cos\delta(u)\sin\delta(u) \tag{E.22}$$

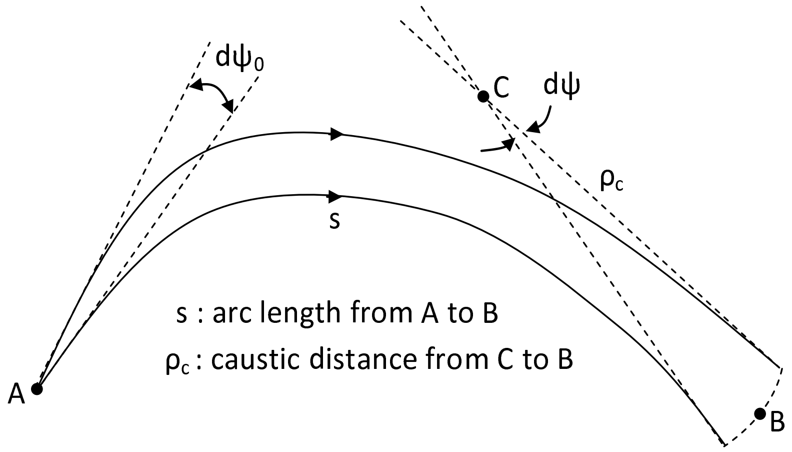

Figure E.1: Caustic distance associated with the spreading of the surface ray field (used to calculate the divergence factor D)

where $\delta(u)$ is the angle between the geodesic and the $u-$ parameter line, k_u and k_v are the principal curvatures along the u and v directions, respectively.

Finally, the divergence factor can be written as

$$D = \sqrt{\frac{s d\psi_0}{\rho_c d\psi}} \tag{E.23}$$

where s, $d\psi_0$, $d\psi$ and ρ_c are shown in Fig. E.1.

E.1 Circular cone geometry

A circular cone, shown in Fig. E.2, may be represented by the following parametric equation

$$\vec{r}(u,v) = (u\sin\theta\cos v, u\sin\theta\sin v, u\cos\theta). \tag{E.24}$$

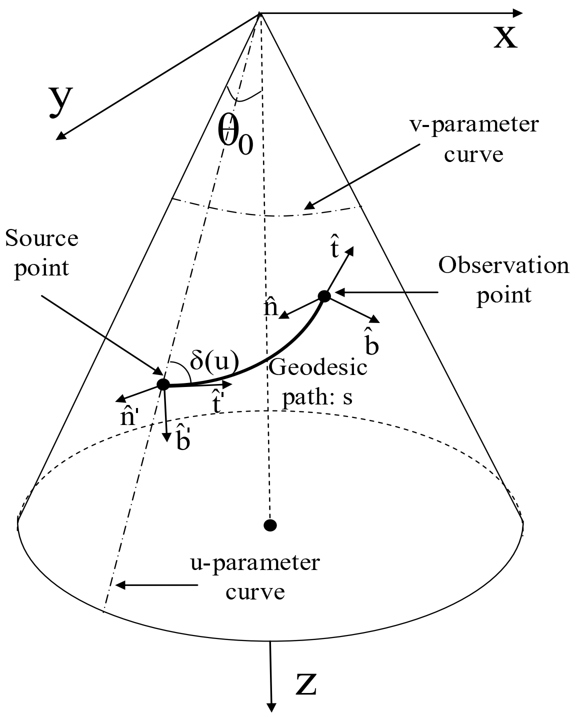

Figure E.2: Circular cone geometry

Differentiation of $\vec{r}$ gives

$$\vec{r}_u = (\sin\theta\cos v, \sin\theta\sin v, \cos\theta) \tag{E.25}$$

$$\vec{r}_v = (-u\sin\theta\sin v, u\sin\theta\cos v, 0) \tag{E.26}$$

$$\vec{r}_{uu} = (0, 0, 0) \tag{E.27}$$

$$\vec{r}_{uv} = (-\sin\theta\sin v, \sin\theta\cos v, 0) \tag{E.28}$$

$$\vec{r}_{vv} = (-u\sin\theta\cos v, -u\sin\theta\sin v, 0). \tag{E.29}$$

The parameters of the first fundamental form are found as

$$E = \vec{r}_u.\vec{r}_u = 1 \tag{E.30}$$

$$F = \vec{r}_u.\vec{r}_v = 0 \tag{E.31}$$

$$G = \vec{r}_v.\vec{r}_v = u^2\sin^2\theta. \tag{E.32}$$

In order to calculate the parameters of the second fundamental form, unit normal of the surface has to be found. Using the definition

$$\hat{N} = \frac{\vec{r}_u \times \vec{r}_v}{|\vec{r}_u \times \vec{r}_v|}, \tag{E.33}$$

the unit normal of the cone is found as

$$\hat{N} = (-\cos\theta\cos v, -\cos\theta\sin v, \sin\theta). \tag{E.34}$$

The parameters of the second fundamental form are found as

$$\begin{aligned} e &= \vec{r}_{uu}.\hat{N} = 0 && \text{(E.35)} \\ f &= \vec{r}_{uv}.\hat{N} = 0 && \text{(E.36)} \\ g &= \vec{r}_{vv}.\hat{N} = u\sin\theta\cos\theta. && \text{(E.37)} \end{aligned}$$

Since $F = 0$ and $f = 0$, $u-$ and $v-$ parameter curves are themselves lines of curvature [51]. Thus, the principal curavatures along the u and v directions can be written as

$$\begin{aligned} k_u &= \frac{e}{E} = 0 && \text{(E.38)} \\ k_v &= \frac{g}{G} = u\tan\theta. && \text{(E.39)} \end{aligned}$$

The equation of the geodesic on a convex surface may be written as

$$\frac{dv}{du} = \frac{\pm h\sqrt{E}}{\sqrt{G}\sqrt{G-h^2}} \tag{E.40}$$

where h is a constant of integration, and is known as the first geodesic constant [14]. The metric of the arc length is obtained as

$$\frac{ds}{du} = \left[E + G\left(\frac{dv}{du}\right)^2\right]^{1/2} = \frac{\sqrt{EG}}{\sqrt{G-h^2}} = \frac{u\sin\theta}{\sqrt{u^2\sin^2\theta - h^2}}. \tag{E.41}$$

$\delta(u)$ is defined as the angle between the geodesic and the $u-$ parameter line. $\cos\delta(u)$ and $\sin\delta(u)$ are found to be

$$\begin{aligned} \cos\delta(u) &= \frac{\sqrt{E}}{(ds/du)} = \sqrt{1 - \left(\frac{h}{u\sin\theta}\right)^2} && \text{(E.42)} \\ \sin\delta(u) &= \frac{|\vec{r}_u \times \vec{r}_v|}{E(ds/du)} = \sqrt{u^2\sin^2\theta - h^2}. && \text{(E.43)} \end{aligned}$$

The surface ray geometric parameters can be found as

$$\rho_g = (k_u\cos^2\delta(u) + k_v\sin^2\delta(u))^{-1} = \frac{1}{u\tan\theta\left(u^2\sin^2\theta - h^2\right)} \tag{E.44}$$

$$\tau = (k_u - k_v)\cos\delta(u)\sin\delta(u) = -\frac{u^2\sin^2\theta - h^2}{\cos\theta} \tag{E.45}$$

where ρ_g and τ are the radius of curvature and the surface ray torsion, respectively. The generalized fock parameter is defined as [11]

$$\begin{aligned} \xi &= \int_{u_s}^{u_f} \frac{\pi^{1/3}}{[\rho_g(s)]^{2/3}} ds \\ &= \pi^{1/3}(\tan\theta)^{2/3}\sin\theta \int_{u_s}^{u_f} u^{5/3}\left(u^2\sin^2\theta - h^2\right)^{1/6} du \end{aligned} \tag{E.46}$$

where u_s and u_f are the values of the u-parameter at the source and observation points, respectively. Since cone is a singly curved surface, blending functions and divergence factor are found to be $\Lambda_s = 0$, $\Lambda_c = 1$, and $D = 1$.

E.2 General parabolic cylinder (GPCYL) geometry

A GPCYL, shown in Fig. E.3, may be represented by the following parametric equation

$$\vec{r}(u,v) = (au, u^2, v) \tag{E.47}$$

where a is shaping parameter and determines the sharpness of the GPCYL. Differentiation of $\vec{r}$ gives

$$\vec{r}_u = (a, 2u, 0) \tag{E.48}$$

$$\vec{r}_v = (0, 0, 1) \tag{E.49}$$

$$\vec{r}_{uu} = (0, 2, 0) \tag{E.50}$$

$$\vec{r}_{uv} = (0, 0, 0) \tag{E.51}$$

$$\vec{r}_{vv} = (0, 0, 0). \tag{E.52}$$

The parameters of the first fundamental form are found as

$$E = \vec{r}_u.\vec{r}_u = a^2 + 4u^2 \tag{E.53}$$

$$F = \vec{r}_u.\vec{r}_v = 0 \tag{E.54}$$

$$G = \vec{r}_v.\vec{r}_v = 1. \tag{E.55}$$

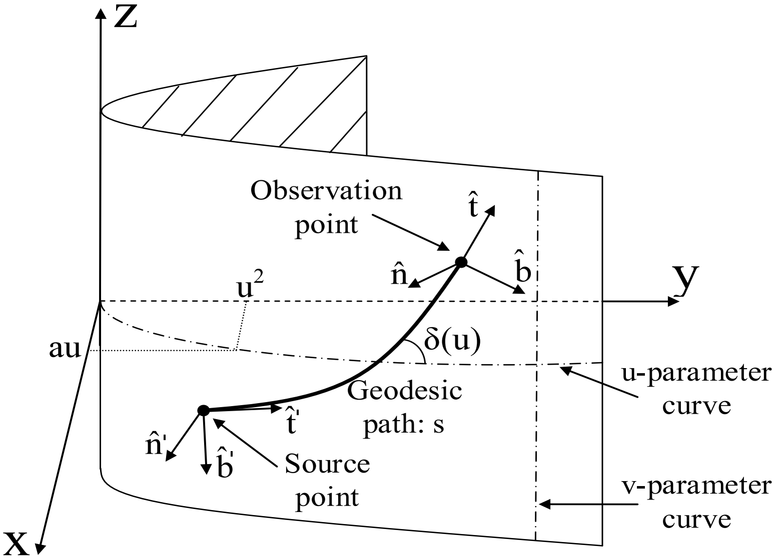

Figure E.3: General parabolic cylinder geometry

In order to calculate the parameters of the second fundamental form, unit normal of the surface has to be found. Using the definition

$$\hat{N} = \frac{\vec{r}_u \times \vec{r}_v}{|\vec{r}_u \times \vec{r}_v|}, \tag{E.56}$$

the unit normal of the GPCYL is found as

$$\hat{N} = (\frac{2u}{\sqrt{a^2 + 4u^2}}, \frac{-a}{\sqrt{a^2 + 4u^2}}, 0). \tag{E.57}$$

The parameters of the second fundamental form are found as

$$\begin{aligned} e &= \vec{r}_{uu}.\hat{N} = \frac{-2a}{\sqrt{a^2 + 4u^2}} && \text{(E.58)} \\ f &= \vec{r}_{uv}.\hat{N} = 0 && \text{(E.59)} \\ g &= \vec{r}_{vv}.\hat{N} = 0. && \text{(E.60)} \end{aligned}$$

Since $F = 0$ and $f = 0$, $u-$ and $v-$ parameter curves are themselves lines of curvature [51]. Thus, the principal curavatures along the u and v directions can be written as

$$\begin{aligned} k_u &= \frac{e}{E} = \frac{-2a}{(a^2 + 4u^2)^{3/2}} && \text{(E.61)} \\ k_v &= \frac{g}{G} = 0. && \text{(E.62)} \end{aligned}$$

The equation of the geodesic on a convex surface may be written as

$$\frac{dv}{du} = \frac{\pm h\sqrt{E}}{\sqrt{G}\sqrt{G-h^2}} \tag{E.63}$$

where h is a constant of integration, and is known as the first geodesic constant [14]. The metric of the arc length is obtained as

$$\frac{ds}{du} = \left[E + G\left(\frac{dv}{du}\right)^2\right]^{1/2} = \frac{\sqrt{EG}}{\sqrt{G-h^2}} = \frac{\sqrt{a^2+4u^2}}{\sqrt{1-h^2}}. \tag{E.64}$$

$\delta(u)$ is defined as the angle between the geodesic and the $u-$ parameter line. $\cos\delta(u)$ and $\sin\delta(u)$ are found to be

$$\cos\delta(u) = \frac{\sqrt{E}}{(ds/du)} = \sqrt{1-h^2} \tag{E.65}$$

$$\sin\delta(u) = \frac{|\vec{r}_u \times \vec{r}_v|}{E(ds/du)} = \frac{\sqrt{1-h^2}}{a^2+4u^2}. \tag{E.66}$$

The surface ray geometric parameters can be found as

$$\rho_g = (k_u\cos^2\delta(u) + k_v\sin^2\delta(u))^{-1} = \frac{-(a^2+4u^2)^{3/2}}{2a(1-h^2)} \tag{E.67}$$

$$\tau = (k_u - k_v)\cos\delta(u)\sin\delta(u) = \frac{2a(1-h^2)}{-(a^2+4u^2)^2} \tag{E.68}$$

where ρ_g and τ are the radius of curvature and the surface ray torsion, respectively. The generalized fock parameter is defined as [11]

$$\xi = \int_{u_s}^{u_f} \frac{\pi^{1/3}}{[\rho_g(s)]^{2/3}} ds \tag{E.69}$$

where u_s and u_f are the values of the u-parameter at the source and observation points, respectively. Evaluation of the above integral results in

$$\xi = (0.5\pi a^2)^{1/3}(1-h^2)^{1/6}\ln|2u + \sqrt{a^2+4u^2}|\Bigg|_{u_s}^{u_f}. \tag{E.70}$$

Since GPCYL is a singly curved surface, blending functions and divergence factor are found to be $\Lambda_s = 0$, $\Lambda_c = 1$, and $D = 1$.

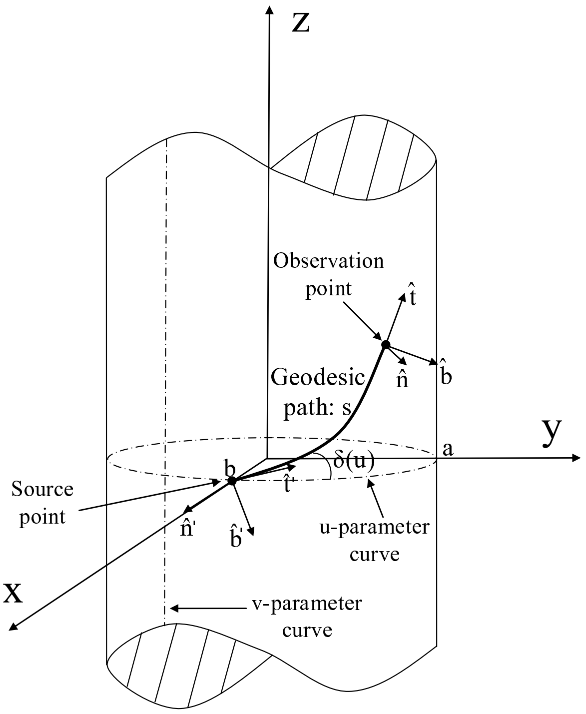

Figure E.4: Elliptic cylinder geometry

E.3 Elliptic cylinder geometry

An elliptic cylinder, shown in Fig. E.4, may be represented by the following parametric equation

$$\vec{r}(u,v) = (b\cos u, a\sin u, v) \tag{E.71}$$

where a is the major axis and b is the minor axis. a/b determines the ellipticity. Differentiation of $\vec{r}$ gives

$$\begin{aligned}
\vec{r}_u &= (-b\sin u, a\cos u, 0) && \text{(E.72)}\\
\vec{r}_v &= (0,0,1) && \text{(E.73)}\\
\vec{r}_{uu} &= (-b\cos u, -a\sin u, 0) && \text{(E.74)}\\
\vec{r}_{uv} &= (0,0,0) && \text{(E.75)}\\
\vec{r}_{vv} &= (0,0,0). && \text{(E.76)}
\end{aligned}$$

The parameters of the first fundamental form are found as

$$E = \vec{r}_u.\vec{r}_u = a^2 \cos^2 u + b^2 \sin^2 u \tag{E.77}$$

$$F = \vec{r}_u.\vec{r}_v = 0 \tag{E.78}$$

$$G = \vec{r}_v.\vec{r}_v = 1. \tag{E.79}$$

In order to calculate the parameters of the second fundamental form, unit normal of the surface has to be found. Using the definition

$$\hat{N} = \frac{\vec{r}_u \times \vec{r}_v}{|\vec{r}_u \times \vec{r}_v|}, \tag{E.80}$$

the unit normal of the elliptic cylinder is found as

$$\hat{N} = (\frac{a \cos u}{\sqrt{a^2 \cos^2 u + b^2 \sin^2 u}}, \frac{b \sin u}{\sqrt{a^2 \cos^2 u + b^2 \sin^2 u}}, 0). \tag{E.81}$$

The parameters of the second fundamental form are found as

$$e = \vec{r}_{uu}.\hat{N} = \frac{-ab}{\sqrt{a^2 \cos^2 u + b^2 \sin^2 u}} \tag{E.82}$$

$$f = \vec{r}_{uv}.\hat{N} = 0 \tag{E.83}$$

$$g = \vec{r}_{vv}.\hat{N} = 0. \tag{E.84}$$

Since $F = 0$ and $f = 0$, $u-$ and $v-$ parameter curves are themselves lines of curvature [51]. Thus, the principal curavatures along the u and v directions can be written as

$$k_u = \frac{e}{E} = \frac{-ab}{(a^2 \cos^2 u + b^2 \sin^2 u)^{3/2}} \tag{E.85}$$

$$k_v = \frac{g}{G} = 0. \tag{E.86}$$

The equation of the geodesic on a convex surface may be written as

$$\frac{dv}{du} = \frac{\pm h\sqrt{E}}{\sqrt{G}\sqrt{G-h^2}} \tag{E.87}$$

where h is a constant of integration, and is known as the first geodesic constant [14]. The metric of the arc length is obtained as

$$\frac{ds}{du} = \left[E + G\left(\frac{dv}{du}\right)^2\right]^{1/2} = \frac{\sqrt{EG}}{\sqrt{G-h^2}} = \frac{\sqrt{a^2 \cos^2 u + b^2 \sin^2 u}}{\sqrt{1-h^2}}. \tag{E.88}$$

$\delta(u)$ is defined as the angle between the geodesic and the $u-$ parameter line. $\cos\delta(u)$ and $\sin\delta(u)$ are found to be

$$\begin{aligned} \cos\delta(u) &= \frac{\sqrt{E}}{(ds/du)} = \sqrt{1-h^2} && \text{(E.89)} \\ \sin\delta(u) &= \frac{|\vec{r}_u \times \vec{r}_v|}{E(ds/du)} = \frac{\sqrt{1-h^2}}{a^2\cos^2 u + b^2\sin^2 u}. && \text{(E.90)} \end{aligned}$$

The surface ray geometric parameters can be found as

$$\rho_g = (k_u \cos^2\delta(u) + k_v \sin^2\delta(u))^{-1} = \frac{-(a^2\cos^2 u + b^2\sin^2 u)^{3/2}}{ab(1-h^2)} \tag{E.91}$$

$$\tau = (k_u - k_v)\cos\delta(u)\sin\delta(u) = \frac{-ab(1-h^2)}{(a^2\cos^2 u + b^2\sin^2 u)^{5/2}} \tag{E.92}$$

where ρ_g and τ are the radius of curvature and the surface ray torsion, respectively. The generalized fock parameter is defined as [11]

$$\begin{aligned} \xi &= \int_{u_s}^{u_f} \frac{\pi^{1/3}}{[\rho_g(s)]^{2/3}} ds \\ &= (\pi a^2 b^2)^{1/3}(1-h^2)^{1/6} \int_{u_s}^{u_f} \frac{du}{(a^2\cos^2 u + b^2\sin^2 u)^{1/2}} && \text{(E.93)} \end{aligned}$$

where u_s and u_f are the values of the u-parameter at the source and observation points, respectively. Since elliptic cylinder is a singly curved surface, blending functions and divergence factor are found to be $\Lambda_s = 0$, $\Lambda_c = 1$, and $D = 1$.

E.4 General paraboloid of revolution (GPOR) geometry

A GPOR, shown in Fig. E.5, may be represented by the following parametric equation

$$\vec{r}(u,v) = (au\cos v, au\sin v, -u^2) \tag{E.94}$$

where a is shaping parameter and determines the sharpness of the GPOR. Differentiation of $\vec{r}$ gives

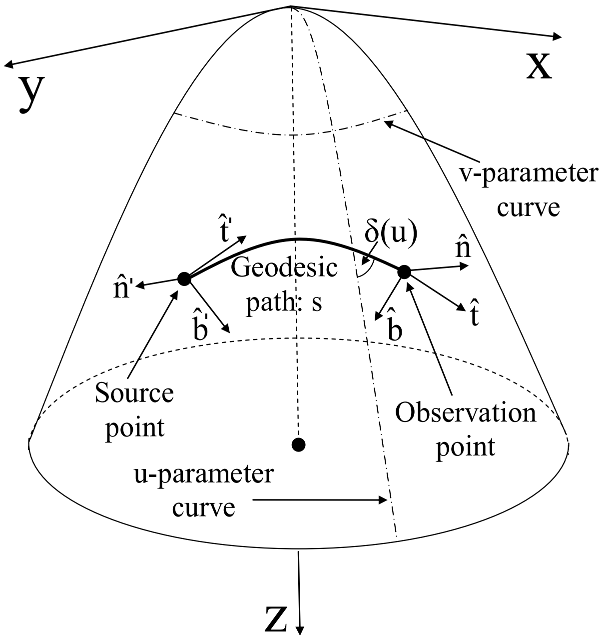

Figure E.5: General paraboloid of revolution geometry

$$\vec{r}_u = (a\cos v, a\sin v, -2u) \tag{E.95}$$

$$\vec{r}_v = (-au\sin v, au\cos v, 0) \tag{E.96}$$

$$\vec{r}_{uu} = (0, 0, -2) \tag{E.97}$$

$$\vec{r}_{uv} = (-a\sin v, a\cos v, 0) \tag{E.98}$$

$$\vec{r}_{vv} = (-au\cos v, -au\sin v, 0). \tag{E.99}$$

The parameters of the first fundamental form are found as

$$E = \vec{r}_u.\vec{r}_u = a^2 + 4u^2 \tag{E.100}$$

$$F = \vec{r}_u.\vec{r}_v = 0 \tag{E.101}$$

$$G = \vec{r}_v.\vec{r}_v = a^2u^2. \tag{E.102}$$

In order to calculate the parameters of the second fundamental form, unit normal of the surface has to be found. Using the definition

$$\hat{N} = \frac{\vec{r}_u \times \vec{r}_v}{|\vec{r}_u \times \vec{r}_v|}, \tag{E.103}$$

the unit normal of the GPOR is found as

$$\hat{N} = (\frac{2u\cos v}{\sqrt{a^2+4u^2}}, \frac{2u\sin v}{\sqrt{a^2+4u^2}}, \frac{a}{\sqrt{a^2+4u^2}}). \tag{E.104}$$

The parameters of the second fundamental form are found as

$$\begin{aligned} e &= \vec{r}_{uu}.\hat{N} = \frac{-2a}{\sqrt{a^2+4u^2}} && \text{(E.105)} \\ f &= \vec{r}_{uv}.\hat{N} = 0 && \text{(E.106)} \\ g &= \vec{r}_{vv}.\hat{N} = \frac{-2au^2}{\sqrt{a^2+4u^2}}. && \text{(E.107)} \end{aligned}$$

Since $F = 0$ and $f = 0$, $u-$ and $v-$ parameter curves are themselves lines of curvature [51]. Thus, the principal curavatures along the u and v directions can be written as

$$\begin{aligned} k_u &= \frac{e}{E} = \frac{-2a}{(a^2+4u^2)^{3/2}} && \text{(E.108)} \\ k_v &= \frac{g}{G} = \frac{-2}{2(a^2+4u^2)^{1/2}}. && \text{(E.109)} \end{aligned}$$

The equation of the geodesic on a convex surface may be written as

$$\frac{dv}{du} = \frac{\pm h\sqrt{E}}{\sqrt{G}\sqrt{G-h^2}} \tag{E.110}$$

where h is a constant of integration, and is known as the first geodesic constant [14]. (E.110) is integrated, and the result is given in closed form as follows [14]

$$\begin{aligned} v &= \frac{h}{a^2}\ln\frac{a[4u^2+a^2]^{1/2}+2[a^2u^2-h^2]^{1/2}}{a[4u^2+a^2]^{1/2}-2[a^2u^2-h^2]^{1/2}} \\ &\quad + \sin^{-1}\left[\frac{a[a^2u^2-h^2]^{1/2}}{u[4u^2+a^2]^{1/2}}\right] + h' && \text{(E.111)} \end{aligned}$$

where h' is the second geodesic constant. The metric of the arc length is obtained as

$$\frac{ds}{du} = \left[E + G\left(\frac{dv}{du}\right)^2\right]^{1/2} = \frac{\sqrt{EG}}{\sqrt{G-h^2}} = \frac{\sqrt{a^2+4u^2}}{\sqrt{1-h^2}}. \tag{E.112}$$

The arc length corresponding to the geodesic between the source (u_s, v_s) and the observation (u_f, v_f) points is obtained by integrating (E.112) as [14]

$$\begin{aligned} s &= \frac{[(4u^2+a^2)(a^2u^2-h^2)]^{1/2}}{2a} \\ &\quad + \frac{a^4+h^2}{8a^2}\ln\frac{a[4u^2+a^2]^{1/2}+2[a^2u^2-h^2]^{1/2}}{a[4u^2+a^2]^{1/2}-2[a^2u^2-h^2]^{1/2}}\Bigg|_{u_s}^{u_f}. && \text{(E.113)} \end{aligned}$$

$\delta(u)$ is defined as the angle between the geodesic and the $u-$ parameter line. $\cos\delta(u)$ and $\sin\delta(u)$ are found to be

$$\cos\delta(u) = \frac{\sqrt{E}}{(ds/du)} = \frac{\sqrt{a^2u^2-h^2}}{au} \tag{E.114}$$

$$\sin\delta(u) = \frac{|\vec{r}_u \times \vec{r}_v|}{E(ds/du)} = \frac{h}{au}. \tag{E.115}$$

The surface ray geometric parameters can be found as

$$\rho_g = (k_u\cos^2\delta(u) + k_v\sin^2\delta(u))^{-1} = \frac{-a^3(a^2+4u^2)^{3/2}}{2a(a^4+4h^2)} \tag{E.116}$$

$$\tau = (k_u - k_v)\cos\delta(u)\sin\delta(u) = \frac{-8h(a^2u^2-h^2)^{1/2}}{a^3(a^2+4u^2)^{3/2}} \tag{E.117}$$

where ρ_g and τ are the radius of curvature and the surface ray torsion, respectively. The generalized fock parameter is defined as [11]

$$\xi(u) = \int_{u_s}^{u_f} \frac{\pi^{1/3}}{[\rho_g(s)]^{2/3}}ds \tag{E.118}$$

here u_s and u_f are the values of the $u-$parameter at the source and observation points, respectively. Evaluation of (E.118) results in

$$\xi = \frac{(4\pi)^{1/3}(a^4+4h^2)^{2/3}}{4a^2}\ln\left.\frac{a[4u^2+a^2]^{1/2}+2[a^2u^2-h^2]^{1/2}}{a[4u^2+a^2]^{1/2}-2[a^2u^2-h^2]^{1/2}}\right|_{u_s}^{u_f}. \tag{E.119}$$

Also, blending functions are found to be

$$\Lambda_s = \left|\sqrt{\left(\frac{a^2}{a^2+4u_s^2}\right)\left(\frac{a^2}{a^2+4u_f^2}\right)}\right| \tag{E.120}$$

$$\Lambda_c = 1 - \Lambda_s. \tag{E.121}$$

Finally, the divergence factor can be written as

$$D = \sqrt{\frac{sd\psi_0}{\rho_c d\psi}} \tag{E.122}$$

where s, $d\psi_0$, $d\psi$ and ρ_c are shown in Fig. E.1. Since there are not any closed form expressions for the parameters $d\psi_0$, $d\psi$ and ρ_c, they are obtained numerically with the aid of Fig. E.1.

Bibliography

[1] C. W. Penney, R. J. Luebbers, and J. W. Schuster, “Scattering from coated targets using frequency-dependent, surface impedance boundary condition in FDTD,” *IEEE Trans. Antennas Propagat.*, vol. AP-44, pp. 434–443, 1996.

[2] R. G. Rojas and Z. Al-hekail, “Generalized impedance/resistive boundary conditions for electromagnetic scattering problems,” *Radio Sci.*, vol. 24, pp. 1–12, Jan.-Feb. 1989.

[3] T. B. A. Senior and J. L. Volakis, *Approximate Boundary Conditions in Electromagnetics.* London: IEEE Press, 1995.

[4] R. G. Kouyoumjian and P. H. Pathak, “A uniform geometrical theory of diffraction for an edge in a perfectly conducting surface,” *Proc. IEEE*, vol. 62, pp. 1448–1461, 1974.

[5] V. A. Fock, *Electromagnetic Diffraction and Propagation Problems.* New York: Pergamon, 1965.

[6] G. Hasserjian and A. Ishimaru, “Excitation of a conducting cylindrical surface of large radius of curvature,” *IRE Trans. Antennas Propagat.*, vol. AP-10, pp. 264–273, May 1962.

[7] Z. W. Chang, L. B. Felsen, and A. Hessel, “Surface ray methods for mutual coupling in conformal arrays on cylinder and conical surfaces,” Tech. Rep. Final Rep., prepared under Contract N00123-76-C-0236, Polytechnic Institute of New York, 1976.

[8] S. W. Lee and S. Safavi-Naini, "Approximate asymptotic solution of surface field due to a magnetic dipole on a cylinder," *IEEE Trans. Antennas Propagat.*, vol. AP-26, pp. 593–598, July 1978.

[9] J. Boersma and S. W. Lee, "Surface field due to a magnetic dipole on a cylinder: Asymptotic expansion of exact-solution," Tech. Rep. Rep. EM78-17, prepared under Contract N00019-78-C-0064 for Naval Air Systems Command, Dept. of Elec. Eng., Univ. of Illinois, Dec. 1978.

[10] P. H. Pathak and N. Wang, "An analysis of mutual coupling between antennas on a smooth convex surface," Tech. Rep. Rep. 784583-7, prepared under Contract N62269-76-C-0554 for Naval Air Development Center, ElectroScience Lab., Dept. of Elec. Eng., The Ohio State Univ., Oct. 1978.

[11] P. H. Pathak and N. Wang, "Ray analysis of mutual coupling between antennas on a convex surface," *IEEE Trans. Antennas Propagat.*, vol. AP-29, pp. 911–922, Nov. 1981.

[12] R. M. Jha and W. Wiesback, "Geodesic constant method: A novel approach to analytical surfaceray tracing on convex conducting bodies," *IEEE Antennas and Propagation Magazine*, vol. 37, pp. 28–38, April 1995.

[13] L. Josefsson and P. Persson, *Conformal Array Antenna Theory and Design.* New Jersey: IEEE Press, 2006.

[14] R. M. Jha, S. A. Bokhari, and W. Wiesback, "A novel ray tracing on general paraboloids of revolution for UTD applications," *IEEE Trans. Antennas Propagat.*, vol. 41, pp. 934–939, July 1993.

[15] P. Persson, L. Josefsson, and M. Lanne, "Investigation of the mutual coupling between apertures on doubly curved convex surfaces: Theory and measurements," *IEEE Trans. Antennas Propagat.*, vol. 51, pp. 682–692, April 2003.

[16] R. Paknys and N. Wang, "High -frequency surface field excited by a magnetic line source on an impedance cylinder," *IEEE Trans. Antennas Propagat.*, vol. 35, pp. 293–298, March 1987.

[17] R. J. Pogorzelski, "On the high-frequency asymptotic evaluation of the potentials of elemental sources on an anisotropic impedance cylinder," *Radio Sci.*, vol. 31, pp. 389–399, Mar.-Apr. 1996.

[18] Ç. Tokgöz and R. J. Marhefka, "Surface field excitation by a magnetic point source on an impedance cylinder," *IEEE Antennas and Propagat. Symposium Dig.*, vol. 4, pp. 2834–2837, July 1999.

[19] Ç. Tokgöz, *Asymptotic high frequency analysis of the surface fields of a source excited circular cylinder with an impedance boundary condition.* PhD thesis, The Ohio-State University Dept. of Electrical Engineering, 2002.

[20] Ç. Tokgöz and R. J. Marhefka, "A UTD based asymptotic solution for the surface magnetic field on a source excited circular cylinder with an impedance boundary condition," *IEEE Trans. Antennas Propagat.*, vol. 54, no. 6, pp. 1750–1757, 2006.

[21] V. B. Ertürk, B. Alisan, and A. Altintas, "Efficient computation of surface fields excited on an electrically large circular cylinder with an impedance boundary condition," *28th General Assembly of International Union of Radio Science (URSI)*, vol. URSI, New Delhi, Oct. 23-29 2005.

[22] B. Alisan, V. B. Ertürk, and A. Altintas, "Efficient computation of non-paraxial surface fields excited on an electrically large circular cylinder with an impedance boundary condition," *IEEE Trans. Antennas Propagat.*, vol. 54, pp. 2559–2567, September 2006.

[23] Ç. Tokgöz, P. H. Pathak, and R. J. Marhefka, "An asymptotic solution for the surface magnetic field within the paraxial region of a circular cylinder with an impedance boundary condition," *IEEE Trans. Antennas Propagat.*, vol. 53, pp. 1435–1443, April 2005.

[24] V. A. Fock, "Diffraction of radio waves around the earth's surface," *Journal of Physics (Moscow)*, no. 9, pp. 256–266, 1945.

[25] J. R. Wait, "On the excitation of electromagnetic surface waves on a curved surface," *IRE Trans. Antennas Propagat.*, vol. 8, pp. 445–449, 1960.

[26] J. R. Wait, "The propagation of em waves along the earth's surfaces," *Electromagnetic Waves, University of Wisconsin Press*, pp. 243–290, 1962.

[27] J. R. Wait, "A note on surface waves and ground waves," *IEEE Trans. Antennas Propagat.*, vol. 13, pp. 996–997, 1965.

[28] J. R. Wait, "Illumination of an inhomogeneous spherical earth by an lf plane electromagnetic wave," *Radio Science*, vol. 2, no. 1, pp. 111–118, 1967.

[29] K. Spies and J. R. Wait, "On the calculation of the ground wave attenuation factor at low frequencies," *IEEE Trans. Antennas Propagat.*, vol. 14, pp. 515–517, 1966.

[30] K. P. Spies and J. R. Wait, "On the calculation of antenna patterns for an inhomogeneous spherical earth," *Radio Science*, vol. 2, no. 11, pp. 1361–1378, 1967.

[31] D. A. Hill and J. R. Wait, "Ground wave attenuation function for a spherical earth with arbitrary surface impedance," *Radio Science*, vol. 15, no. 3, pp. 637–643, 1980.

[32] D. A. Hill and J. R. Wait, "Hf ground wave propagation over sea ice for a spherical earth model," *IEEE Trans. Antennas Propagat.*, vol. 29, no. 3, pp. 525–527, 1981.

[33] R. J. King and J. R. Wait, "Electromagnetic ground wave propagation," *Theory and Experiment, in Symposia Mathematica - New York: Academic*, vol. 18, pp. 107–208, 1976.

[34] H. Bremmer, "Applications of operational calculus to ground-wave propagation, particularly for long waves," *IRE Trans. Antennas Propagat.*, vol. 6, pp. 267–272, 1958.

[35] J. R. Wait, "Radiation from a vertical antenna over a curved stratified ground," *Nat. Bur. Stand. J. Res.*, vol. 56, pp. 237–244, 1956.

[36] J. R. Wait, "On the theory of propagation of electromagnetic waves along a curved surface," *Can. J. Phys.*, vol. 36, pp. 9–17, 1958.

[37] J. R. Wait, “The ancient and modern history of EM ground wave propagation,” *IEEE Trans. Antennas Propagat. Magazine*, vol. 40, no. 5, pp. 7–24, 1998.

[38] B. Alisan and V. B. Erturk, “A high-frequency based asymptotic solution for surface fields on a source-excited sphere with an impedance boundary condition,” *Radio Science*, vol. 45, no. RS5008, 2010.

[39] S. W. Lee, R. Mittra, J. Boersma, and E. Jung, “An investigation on characterizing mutual coupling between two antenna slots on a cone,” Tech. Rep. Rep. EM79-2, prepared under Contract N00019-78-C-0064 for Naval Air Systems Command, Dept. of Elec. Eng., Univ. of Illinois, Jan. 1979.

[40] S. W. Lee, “Mutual admittances of slots on a cone: solution by ray technique,” *IEEE Trans. Antennas Propagat.*, vol. AP-26, pp. 768–773, Nov. 1978.

[41] K. E. Golden, G. E. Stewart, and D. C. Pridmore-Brown, “Approximation techniques for the mutual admittance of slot antennas on metallic cones,” *IEEE Trans. Antennas Propagat.*, vol. 22, pp. 43–48, 1974.

[42] N. A. Logan and K. S. Yee, “A simple expression for propagation constants associated with a reactive convex surface,” *IRE Trans. Antennas Propagat.*, vol. 10, p. 103, 1962.

[43] L. B. Felsen and K. Naishadham, “Ray formulation of waves guided by circular cylindrical stratified dielectrics,” *Radio Science*, vol. 26, pp. 203–209, 1991.

[44] J. B. Keller, “Geometrical theory of diffraction,” *J. Opt. Soc. Amer.*, vol. 52, pp. 116–130, 1962.

[45] W. C. Chew, *Wave and Fields in Inhomogneous Media.* Van Nostrand Reinhold, 1990.

[46] R. E. Collin, *Theory of Guided Waves.* New York: McGraw-Hill, 1960.

[47] M. Abramowitz and I. A. Stegun, *Handbook of Mathematical Functions with Formulas, Graphs, and Mathematical Tables.* New York: Dover, 1964.

[48] C. A. Balanis, *Advanced Engineering Electromagnetics.* New York: Wiley, 1989.

[49] R. F. Harrington, *Time-Harmonic Electromagnetic Fields.* New York: IEEE Press, 1961.

[50] G. N. Watson, “The diffraction of electric waves by the earth,” *Proc. Roy. Soc. London*, vol. 95A, pp. 83–99, 1918.

[51] S. W. Lee, “Differential Geometry for GTD Applications,” Tech. Rep. Electromagnetics Lab. Report No. 77-21, University of Illinois at Urbana-Champaign, Oct. 1977.